Università degli Studi di Padova

Dipartimento di Fisica e Astronomia "Galileo Galilei"

Ph.D. course in Material Science and Technology

Doctoral Thesis

Crystallization of amorphous tantala coatings and its implication on GW interferometry

Ph.D. school coordinator:
Prof. Stefano Agnoli
Supervisor:
Prof. Marco Bazzan

Ph.D. student:
Giulio Favaro
1229775

XXXVI cycle

Che fatica la vita. Ma tanto poi finisce.
Viure és un cansament. Però, amb tot, s'acaba.

Abstract

Gravitational astronomy is one of the most meaningful achievements of the new millennium, opening the way to a new window to remote and mysterious cosmic objects such as black holes and neutron stars. Gravitational wave interferometers are among the most sensitive instruments ever developed. The key element of those instruments is constituted by mirror test masses whose surface is coated with special materials to reflect the laser signal of the interferometer. The coating thermal noise (CTN) is one of the main causes limiting the sensitivity of gravitational wave interferometers in their most sensistive frequency band. Presently, the research of new routes to reduce this noise is the object of a large international effort. As a part of this coordinated research, this thesis, performed in the framework of the LIGO-Virgo collaboration, is devoted to study the impact of a controlled partial crystallization on the noise characteristics of those coatings, as a possible strategy to improve their performances. A large set of annealing conditions were explored in order to promote the formation of crystalline grains inside amorphous films of Ta2O5 deposited by Ion Beam Sputtering. This is indeed a reference coating material for gravitational wave interferometry and the one that is most plagued by the thermal noise issue. Several techniques (optical microscopy, Raman, XRD, and AFM measurements) were employed, showing how in our samples the material upon annealing single-crystalline grains with random orientation, whose size is comparable or larger than the film thickness. In-situ XRD experiments have been used to characterize the transition kinetics from amorphous to crystalline states. Using classical crystallization theory, activation energies for the growth process are determined, and the parameters used to describe the characteristic crystallization time in the Avrami model are found. A dedicated in-situ total scattering experiment has been carried out at the ESRF synchrotron radiation facility showing that the grains nucleate with an already considerable size of several tens of nanometers. The crystalline phase has been investigated by combining a Rietveld analysis of the diffraction spectra. Our results point out that a large part of the diffractogram can be explained by a simple hexagonal unit cell, even though some features remain unclear and require further investigation.

The thermal noise characteristics of the treated samples were systemat-

ically studied by an indirect approach consisting in the measurement of the mechanical losses by means of a Gentle Nodal Suspension system. Our results show, to our knowledge for the first time, that mechanical losses depend on the crystallized fraction, showing a minimum for a 5% crytsalline volume. In those conditions our partially crystallized coatings display a reduction of the mechanical losses of about 15% with respect to the standard Ta2O5 coatings prepared according to the standard procedures for GW interferometers. Finally, the impact of the crystallized fraction on the optical properties of the films has been measured. To this purpose, a dedicated optical set-up has been developed to perform both angle-resolved optical scattering and total integrated scattering measurements. Our preliminary results indicate that, at the crystallization levels corresponding to the "sweet spot" for mechanical losses minimization, the optical scattering is increased of a considerable amount, making difficult its applicability in a realistic context. However the possiblity of reducing the losses by engineering the crystallized grain size distribution via a suitable annealing remains an option to be studied.

In summary, this project presents a systematic approach to address thermal Brownian noise in gravitational-wave detectors by introducing a controlled crystalline grains dispersion into amorphous coatings. The research spans fundamental experiments, model construction, facility development, and material characterization. The identified sweet spot for crystallization opens avenues for further optimization of presently used materials, emphasizing the potential for an holistic improvement in the interferometer sensitivity of gravitational wave detectors.

Contents

Chapter 1

Introduction

Since the ages of myth, the Universe has always been to Humankind the most fascinating perhaps of all mysteries. The ancients raising their eyes to the sky discerned fantastic creatures in the vault of heaven and tried to explain with them the nature of the stars. As the centuries have passed, our understanding of the cosmos has greatly changed; yet, until just a few years ago, our way of looking at the sky was not so very different from that of our ancestors. The signal that carried information about celestial bodies was electromagnetic radiation, light in simpler words, which was measured first with the eyes, then with increasingly sophisticated instruments. However, by traversing interstellar space, light can be absorbed, perturbed, and this limits the portion of the Universe we can probe with these kinds of techniques. In addition, not all the incredible objects and phenomena existing in the Universe emit electromagnetic radiation, thus being undetectable by this means.

In 2015, the sophisticated instruments of the international LIGO-Virgo collaboration observed a gravitational wave for the first time in a direct way [10]. This is a pivotal discovery for a variety of reasons. Perhaps the most important is precisely that this type of detection has opened up a completely different way of studying the cosmos. Gravitational waves interact very little with matter and therefore can propagate undisturbed for enormous distances. For the same reason they are incredibly difficult to measure, which explains why it took almost exactly 100 years between Albert Einstein's prediction of their existence, and their experimental detection. In addition, some of the strongest sources of gravitational waves, such as Black Holes and Neutron stars, are celestial objects that are extremely difficult to study with other types of signals. Gravitational astronomy is thus a powerful new tool for the exploration of the cosmos that allows us to expand our knowledge of cosmology, astrophysics and fundamental physics in a previously unthinkable way.

After the first detection, others followed. Italy's Virgo observatory en-

tered observation mode and joined the international detector network, helping to improve the reliability and accuracy of detections. Other instruments such as KAGRA in Japan and LIGO-India will soon do so. But these major successes are only the beginning of a real revolution in astronomical science that still has unimaginable potential. Motivated by the great successes achieved, other increasingly advanced and futuristic techniques are now being studied to expand the number, type and precision of signals collected. This is a technological challenge involving many different disciplines, from quantum optics to materials science, from engineering to electronics. Gravitational wave research is now more than ever an interdisciplinary research topic.

The devices that were developed to detect gravitational waves are large scale laser interferometers. Those sophisticated optical instruments are so sensitive that they are able to sense a variation of length of one part over 10^{21}. This is like measuring the size of an atom against the distance between Earth and Sun. At this incredible level of sensitivity, every external influence may act as an unwanted source of noise. For this reason, the identification and the mitigation of all possible noise sources, including the most feeble ones, is one of the main tasks of experimental gravitational wave scientists. One of the most elusive and yet problematic form of noise get its origin in the very hearth of the interferometers: the mirror test masses which, with their motion, are the responsible for the detection of the gravitational waves. They are massive mirrors made of large glass cylinders whose finely polished surface is covered with some special optical film that work as an almost ideal reflecting surface. Those films are actually multilayers composed of alternate slabs of amorphous materials with different refractive index deposited by Ion Beam Sputtering. The present coating technology relies on a very standard solution: SiO_2 as low index material and Ta_2O_5 doped with TiO_2 as high-index one. This structure works as a nearly - perfect Bragg mirror reflecting almost the totality of the laser light with very small absorption and negligible scattering. At finite temperature T, the atoms composing the optical coatings are fluctuating around several different configurations by jumping across an energy barrier of the order of kT, where k is the Boltzmann's constant. At the extreme sensitivity level of gravitational interferometers, even those atomic motions are enough to cause a perturbation of the signal. In fact, the coating thermal noise (CTN) is the main noise source in the most sensitive frequency band of the interferometers, where a large portion of the gravitational wave signal is contained. In particular, it can be shown that the high-index layers of TiO_2:Ta_2O_5 are the dominating noise source. To tackle this issue, a large international effort is being carried out to research for new strategies to improve this aspect of the coating technology. It is worth mentioning that even a moderate increase of the coating performance would immediately bring larger SNR and therefore a larger portion of accessible universe without doing any other modification to the instrument. In

this sense it is a very sensible way to go.

This thesis is devoted to the exploration of a possible way improve the coating thermal noise by using precisely controlled annealing procedures. Thermal treatments are a standard step in the production of the coating multilayers covering the mirrors of gravitational wave interferometers. However the usual procedure previews a treatment carried out at a relatively low temperature ($500°C$) for 10 hours. This treatment is meant simply to relax the structure of the as-deposited coatings and is known to bring some benefit from the point of view of the thermal noise behaviour. However, a systematic investigation on how much this process can be pushed to reach its ultimate effectiveness is still lacking. In particular amorphous thin films, when heated for sufficiently long times, show a tendency to transform into polycrystalline. While this circumstance is usually regarded as detrimental of the coatings performance, it is also true that the crystalline state, being characterized by a lower free energy with respect to the amorphous one, is also intrinsically more stable and thus less plagued by thermal noise. The details on how the beginning of the crystallization process impact on the coating thermal noise are still poorly unknown. To investigate this aspect it is mandatory to understand how the crystallization process occurs in the coating amorphous films at a microscopic level depending on the treatment time and temperature. Also, it is necessary to assess how the transition from amorphous to crystalline impact on the overall optical characteristic of the film and on on its applicability for gravitational wave detectors.

This task has been tackled in this work by studying Ta_2O_5 layers as a meaningful prototype system of the high-index materials used in gravitational wave detectors. After a review of the state of the art in chapter 2 and a presentation of the techniques used to characterize the physico-chemical properties of the coatings in chapter 3, the amorphous-to-crystalline transition is analyzed experimentally in chapter 4, providing an assessment of the microscopic structure of the crystalline grains and studying the transformation kinetics in the framework of a Johnson-Mehl-Avrami-Kolmogorov model. A more in-depth investigation of the crystalline structure of Ta_2O_5 iss then presented in chapter 5. The results obtained from the crystallization kinetics can be used to realize coatings with tailored crystallized volume fraction, from amorphous to fully crystallized, which are used in chapter 6 to study the impact of the crystallization on the optical performances of the coating. A dedicated setup, developed in our labs for this purpose, is described and some results are presented. As expected, the presence of crystallized grains brings an increase of the scattering losses.
Finally, in chapter 7 the thermal noise properties of this partially crystallized coatings have been studied by means of an indirect approach based on the measurement of mechanical losses. It is shown, to our knowledge for the first time, that a small crystallized fraction is beneficial from the point of view of thermal noise and may be considered as a viable solution to improve

the properties of the coatings beyond the present levels.

In the Conclusions, chapter 8, some perspectives are then given on possible future directions of this research.

Chapter 2

State of the Art

The first detection of a Gravitational Wave in 2015, GW150914 [14], represents a confirmation of General Relativity, exhibit a direct confirmation of the existence of black holes in the 30-60 solar masses range, and proved that Black Holes can form binary systems and can merge within the Universe time. Furthermore it paved the way for the birth of multimessenger Astronomy, further tests of General Relativity, and new measurements of the expansion rate of the Universe. The central figure in this success story is a new kind of Gravitational Waves detector: the Gravitational Waves interferometer able to finally reach the sensitivity needed to detect the feeble signal of a Gravitational Wave.
In this chapter a brief explanation of the Gravitational Waves phenomena is given in section 2.1; after, in section 2.2, the key principles and limitations of the Gravitational Waves Interferometers are presented. As the objective of this thesis is to study how to improve the Detectors' sensitivity through research on mirror's coatings, section 2.2.3 go more in depth on the different kind of noises that affect the Gravitational Waves Interferometers while section 2.3 deeps down onto the coatings currently in use and the strategies adopted to improve them.

2.1 Gravitational Waves

In 1916 Albert Einstein published the theory of General Relativity (GR) that become the most accepted theory of gravity [1]. The theory made several counter intuitive predictions, such as the bending of light in gravitational fields, whose confirmation validated the theory. Among this set of predictions two of them were lacking direct confirmation: Black Holes and Gravitational Waves (GW). The former are regions of space-time that cannot communicate with the rest of the Universe due to the strength of their gravity, while the latter are ripples in space-time itself. The two phenomena are closely tied together since GW are the main signal one could use to study

a black holes. However, the detection of GWs is not an easy task since the physical effects caused by these ripples in space-time are extremely small.

2.1.1 General Relativity summary

The key idea in General Relativity is to abandon the idea of the existence of a gravitational force between masses and replace it with the introduction of the space-time continuum. The specific geometry of space-time is dictated by the masses and the energies present in it and the Gravitational force becomes an emergent effect of said geometry.
From a mathematical point of view, space-time is a four dimensional manifold that can be described by a metric tensor $g_{\mu\nu}$ where the index value 0 usually represent the time coordinate and the index values $1, 2, 3$ the spatial ones. The equation governing General Relativity is the Einstein's Field Equation:

$$R_{\mu\nu} - \frac{1}{2} g_{\mu\nu} R = \frac{8\pi G}{c^4} T_{\mu\nu} \tag{2.1}$$

Where G is Newton's gravitational constant, $T_{\mu\nu}$ is the stress-energy Tensor, and $R_{\mu\nu}$ and R are Ricci's Tensor and Ricci's Scalar respectively. Ricci's Tensor and Ricci's Scalar are defined as:

$$R_{\mu\nu} = R^{\alpha}_{\mu\alpha\nu} \tag{2.2}$$

$$R = g^{\mu\nu} R^{\alpha}_{\mu\alpha\nu} \tag{2.3}$$

Where the Riemann's Tensor $R^{\mu}_{\nu\rho\sigma}$ appears:

$$R^{\mu}_{\nu\rho\sigma} = \partial_\sigma \Gamma^{\mu}_{\nu\rho} + \Gamma^{\mu}_{\alpha\rho} \Gamma^{\alpha}_{\nu\sigma} - \Gamma^{\mu}_{\alpha\sigma} \Gamma^{\alpha}_{\nu\rho} \tag{2.4}$$

And where $\Gamma^{\mu}_{\nu\rho}$ are the Christoffel's Symbols:

$$\Gamma^{\mu}_{\nu\rho} = \frac{1}{2} g^{\mu\sigma} \left(\partial_\nu g_{\sigma\rho} + \partial_\rho g_{\sigma\nu} - \partial_\sigma g_{\nu\rho} \right) \tag{2.5}$$

The meaning of this equation lies in the fact that the left side of the equation describe the geometric structure of the space-time while the right side relates it to the distribution of masses and energies. When no deformation of the space-time is present, i.e. when the space-time is flat, the metric tensor takes the form of Minkowsky tensor $\eta_{\mu\nu}$:

$$g_{\mu\nu} = \eta_{\mu\nu} = \begin{pmatrix} -1 & 0 & 0 & 0 \\ 0 & 1 & 0 & 0 \\ 0 & 0 & 1 & 0 \\ 0 & 0 & 0 & 1 \end{pmatrix} \tag{2.6}$$

In general, when a mass and or energy distribution are present, the Einstein's equation are very difficult to solve analytically. We can consider however

the case of an almost flat space-time that differs from a Minkowsky space for a very small perturbation h:

$$g_{\mu\nu} = \eta_{\mu\nu} + h_{\mu\nu}, \qquad h_{\mu\nu} \ll 1 \tag{2.7}$$

We can take advantage of this new form of $g_{\mu\nu}$ by rewriting Einstein's equation in a linearized form. Substituting equation 2.7 inside these definitions, and keeping only the terms up to the first order in h we obtain a new form of the Einstein's Field Equation:

$$\Box \left(h_{\mu\nu} - \frac{1}{2}\eta_{\mu\nu}h^{\alpha}_{\alpha} \right) = -\frac{16\pi G}{c^4}T_{\mu\nu} \tag{2.8}$$

When in an empty space the stress-energy Tensor $T_{\mu\nu}$ becomes null and equation 2.8 becomes a wave equation hence predicting the existence of gravitational waves. We can rewrite in a simplified form:

$$\Box \bar{h}_{\mu\nu} = 0 \tag{2.9}$$

and the solutions of this equation are a set of plane waves that abide the relation [8]:

$$\bar{h}_{\mu\nu} = \epsilon_{\mu\nu} \exp\left[ik^{\alpha}x_{\alpha}\right] \tag{2.10}$$

with ϵ the polarization tensor and k the wavevector. Choosing to write this equations under the transverse-traceless gauge (TT-gauge) [13] it can be shown that, for a wave propagating through the z axis ($\mu = 3$), the polarization tensor can be written as the linear combination of two simple tensors:

$$e^{+}_{\mu\nu} = \begin{pmatrix} 0 & 0 & 0 & 0 \\ 0 & 1 & 0 & 0 \\ 0 & 0 & -1 & 0 \\ 0 & 0 & 0 & 0 \end{pmatrix} \qquad e^{x}_{\mu\nu} = \begin{pmatrix} 0 & 0 & 0 & 0 \\ 0 & 0 & 1 & 0 \\ 0 & 1 & 0 & 0 \\ 0 & 0 & 0 & 0 \end{pmatrix} \tag{2.11}$$

called respectively "plus" and "cross". The physical meaning of this decomposition is that a wave traveling through z has an effect only in x and y. A visual representation of the effect of the passage of a Gravitational wave on a ring of masses placed in the xy plane can be seen in figure 2.1

2.1.2 Sources of Gravitational Waves

In the previous subsection it has been shown how a small perturbation of the space-time propagates through it as a wave-like phenomenon. To understand however what generates these perturbations we need to solve the full form of equation 2.8. If we consider an energy-mass distribution that changes with time the emission can be expressed, analogously to the typical electromagnetic case, as a series of multipoles terms where the lower

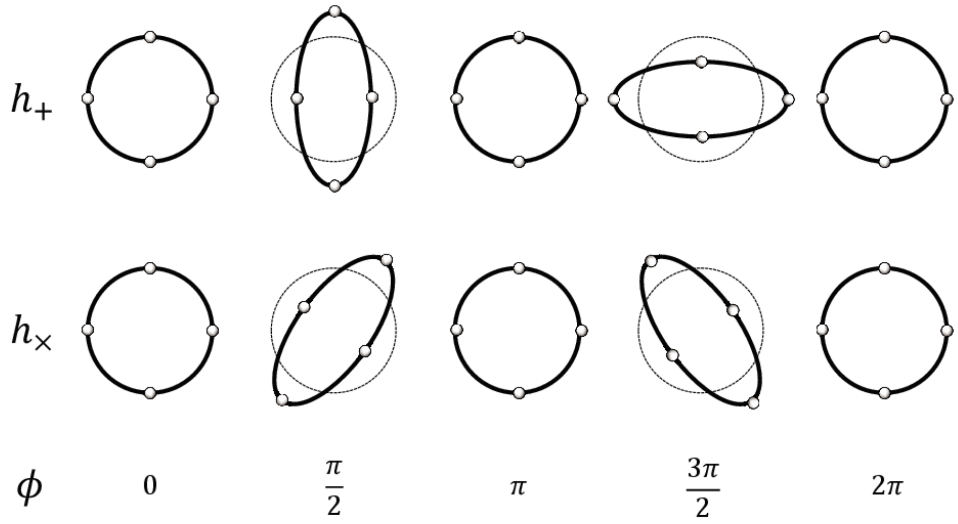

Figure 2.1: Visualization of the effect of the passage of a Gravitational wave on a ring of masses lying in a plane perpendicular to the wave propagation direction. The upper and the lower part of the image refer to the different possible polarization of the wave and show how, except for a different phase of 45°, the two polarizations cause no physical difference [2]

the order of the multipole, the higher the intensity of the associated emission. Mass conservation forbids the existence of a monopole term emission and the absence of a negative charge for the gravitational field forbids the existence of a dipole emission leaving the quadrupole emission to be the dominant term [8].
As Einstein did in 1918 [9] the amplitude of the space-time perturbation $h_{\mu\nu}$ can be expressed as:

$$h_{\mu\nu} \simeq \frac{2G}{rc^4}\ddot{Q}_{\mu\nu} \tag{2.12}$$

where $Q_{\mu\nu}$ is the quadrupole moment and r the the distance travelled by the wave from its source to the observation point. For typical astronomical sources and distances, evaluating equation 2.12 shows that Gravitational waves produce extremely small deformations of the space-time with their magnitude being in the most extreme cases on the order of 10^{-21}.
Up to present times, the only identified sources of gravitational waves have been the coalescences of compact binary systems. These binaries constitute astrophysical systems comprised of two dense objects, only neutron stars and black holes so far, bound together by their gravitational field. As these objects revolve around the center of mass of the system, the emission of gravitational waves leads to energy loss, causing their orbits to contract. Ultimately, the objects inspiral, gradually approaching each other until they merge into a singular, more massive entity. The resulting mass is less than

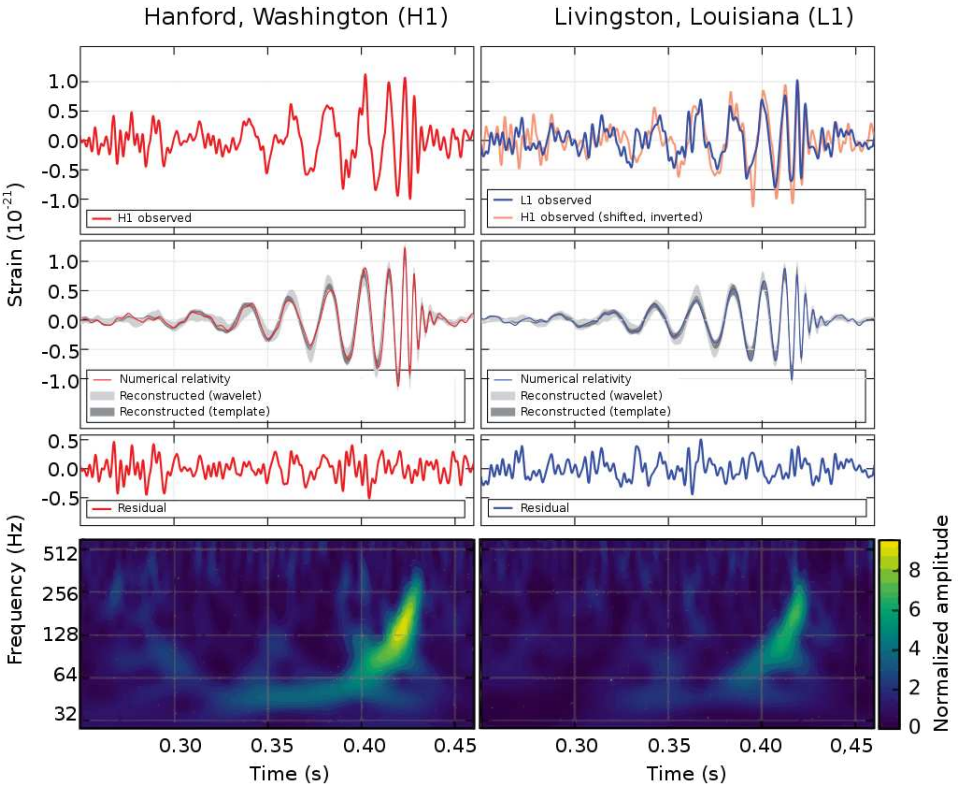

Figure 2.2: The signal measured by the LIGO interferometers of the first gravitational wave ever observed GW150914 [10]. In order from the upper part to the bottom: the experimental data measured for the event, a numerical simulation of the waveform produced by a coalescence compatible with the observed event, residuals between data and simulation, and a time-frequency map of the signal.

the combined mass of the initial objects due to energy dissipation through gravitational wave emission.
The coalescence signal unfolds in three distinctive phases: inspiral, merger, and ringdown. The inspiral phase involves the orbital dance of the two objects, while the merger represents the peak of the signal as the objects unite. The subsequent ringdown phase is a final, damped stage as the newborn entity settles into equilibrium. An example of a GW signal, as recorded from the LIGO interferometers, is shown in figure 2.2. The observed coalescences signals can be categorized based on the nature of the merging binary systems:

- **Binary Neutron Star (BNS):** a duo of neutron stars in a binary system.

- **Binary Black Hole (BBH):** a binary system featuring two black holes.

- **Neutron Star-Black Hole Binary (NSBH):** a binary system comprising a neutron star and a black hole.

Each unique binary pair produces a distinctive gravitational wave signal influenced by various factors characterizing the system, such as the individual masses and the orientation of the rotational plane respect Earth. Other Gravitational Waves sources expected but not observed so far are:

- **Pulsar:** Neutron stars in rapid rotation with a non spherical symmetry in their mass distribution are expected to emit a continuous wave signal whose amplitude depends on the amount of mass asymmetry. Such sources have not been detected yet since their expected amplitude is currently below the capability of measurement but their defection is expected in the proximal future.

- **Supernovae:** The collapse of a supernovae core, when not happening in a perfectly symmetric way, is expected to generate a signal so weak that the detection rate becomes low; in facts no signal has been detected so far even if many Supernovae events where found by traditional telescopes and even with future upgrades the probabilities of identifying one of such events remains low.

2.2 Gravitational Waves Interferometers

The actual existence of GW for many decades since their first theorising was up to debate and in particular many doubts were present regarding whether they were a real physical phenomena or just a mathematical artifact due to a particular gauge choice. While the first indirect confirmations of GW came in 1974 by observing the Hulse–Taylor binary pulsar orbital decay, the direct observation proved instead to be much more diffcult. In 1963 Gerstenstein and Pustovoit firstly proposed the idea of using interferometric techniques to detect the differential change in space-time metric of equation 2.10 by comparing the change of length experienced by a laser beam across the two perpendicular arms of an interferometer. In fact, in order to discriminate the true GW feeble signal from the background noise, at least a couple of interferometers located at a great distance apart are necessary. After the first rilevation in 2015 The concept of Gravitational Waves Interferometers (GW interferometers) became the new default when talking about Gravitational waves detection so that nowadays several detections are routinely reported, allowing a remarkable step forward in our exploration of the Universe.

2.2.1 Detection Principle

The current design of GW interferometers is based upon the optical layout of a Michelson interferometer a simple scheme of which can be seen in figure 2.3. The electric field of the laser light injected inside the system can be

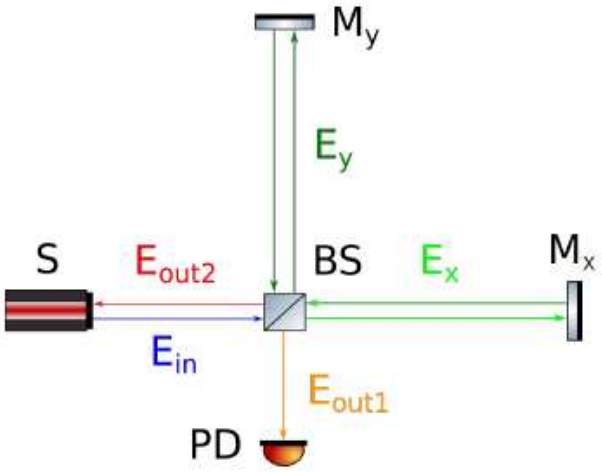

Figure 2.3: Simplified Virgo Optical layout from [12]. M are the two mirrors, BS is the beam splitter, PD is the detector, and S is the laser source.

expressed as:

$$E_{in} = E_0 e^{-i(\omega_\lambda t - kx)} \tag{2.13}$$

where E_0 is the maximum amplitude, k the module of the wavevector, ω_λ the laser frequency and and x the length of the injection stage. After encountering the Beam Splitter the power gets divided into the two arms, it gets reflected by the end mirrors M_x and M_y, and lastly, after traveling back through the whole system, the beams recombine at the beamsplitter so the total field at one of the output ports is:

$$E_{out} = E_1 + E_2 = \frac{E_0}{\sqrt{2}} \left(e^{-i(\omega t - 2kL_1 + \phi_1)} + e^{-i(\omega t - 2kL_2 + \phi_2)} \right) \tag{2.14}$$

where $2L_1$ and $2L_2$ are the total optical path lengths travelled by the two beams and ϕ_1 and ϕ_2 are additional phases shift induced by the reflections and other optical elements that in this simplified scheme are not considered. We have however to take into account that what we are able to measure is not the electric field but the intensity of the radiation so we can write:

$$I_{out} = |E_{out}|^2 = \frac{E_0^2}{2} \left[1 + \cos\left(k\Delta L + \Delta\phi \right) \right] = \frac{E_0^2}{2} \sin^2 \left(\frac{k\Delta L}{2} \right) \tag{2.15}$$

where in the last passage we simplified the expression by assuming that the interferometer is designed in such a way that the different phase shifts

are compensated. As we can see the measured intensity is in general only dependant from the relative difference in length of the two arms and we can so tune the unperturbed signal we measure at the output ports by tuning the length of the interferometer arms. The common choice is to operate GW interferometers close to the so-called darkfringe configuration at the output port 1 by setting the interferometer working point accordingly.
When a GW passes by, as we showed precedently, the spacetime contracts and expand repeatedly; this deformation affects the length of the arms of the interferometer in opposite ways and produces a rise of the signal from zero. To measure the effect we can start from the definition of the invariant length in GR ds:

$$ds^2 = g_{\mu\nu} dx^\mu dx^\nu \tag{2.16}$$

if we consider the passage of a plus polarized GW we can rewrite:

$$ds^2 = (\eta_{\mu\nu} + h^+_{\mu\nu}(t)) dx^\mu dx^\nu = 0 \tag{2.17}$$

In the event of the wave being perfectly perpendicular to the interferometer xy plane we can express the deformation of the x coordinate solving the previous equation as:

$$dx = \sqrt{\frac{c^2 dt^2}{1 + h(t)}} \simeq \pm c \left(1 - \frac{h(t)}{2}\right) dt \tag{2.18}$$

where h(t) is the specific wave equation solution of equation 2.10 that is passing by. If we want to calculate the collective change across one arm we must firstly integrate the previous equation over r the forward direction of motion of the light inside the arm obtaining:

$$\int_0^{L_1} dx = \int_0^{t_1} c \left(1 - \frac{h(t)}{2}\right) dt \tag{2.19}$$

and after we must integrate over the backward direction obtaining:

$$\int_{L_1}^{0} dx = \int_{t_1}^{t_2} c \left(1 - \frac{h(t)}{2}\right) dt \tag{2.20}$$

By inverting the last two equations in order to obtain the instant at which the wave reaches the mirror and the beamsplitter, we can calculate the total time a photon needs to travel across the interferometer arms:

$$(t_2 - t_0) = \frac{2L_1}{c} + \frac{1}{2} \int_{t_0}^{t_2} h(t) dt \tag{2.21}$$

To finish our calculation we now need to solve this equation for t_2 that appears both on the left side of the equation and as a bound of the integral on the right side. We can approximate the integral bound to be equal to the

total time a photon needs to travel inside the non-deformed interferometer $t = 2L/c$ with L the average non deformed length of an arm (the reasoning being that the variations involved are very small and the integrand term is already dependant on the GW passing by).

$$(t_2 - t_0) = \frac{2L_1}{c} + \frac{L_1}{c} h\left(t_0 + \frac{L_1}{c}\right) \frac{\sin(\omega_{gw} L_1/c)}{\omega_{gw} L_1/c} \tag{2.22}$$

The rightmost term here has been evaluated for a plane wave solution of equation 2.10 $h(t) = h_0 \cos(\omega_{gw} t + \alpha)$. Note also that we introduce ω_{gw}, the GW frequency, in order to differentiate from the laser light frequency ω_λ previously used.
Repeating the process for both arms and summing their contributions we can calculate the total phase difference induced by the passage of a GW:

$$\Delta\phi \simeq \omega_\lambda \left(2\frac{L_1 - L_2}{c} + \frac{2L}{c}\frac{\sin(\omega_{gw} L/c)}{\omega_{gw} L/c} h \cos(\omega_{gw} t + \alpha)\right) \tag{2.23}$$

Studying this function we can see that two limit behaviours are verified when the frequency of the GW passing is either too high or too low. For $\omega_{gw} \ll 2\pi c/L$ the frequency of the GW is too small to be dectected: the perturbation is "static" during the photons' travel time. For $\omega \gg 2\pi c/L$ the frequency of the GW is too high to be dectected: the many oscillations of the GW perturbation cancel out during the photon travel time averaging at zero.

2.2.2 Current GW interferometers

The current GW interferometers improve the classical Michelson interferometer design by employing Fabry-Perot cavities in the arms of the interferometer in order to increase the effective length of the instrument. To avoid any possible external influence the beam travels in the vacuum and all the core optics of the instrument are suspended by a multistage inverted pendulum. Currently there are five ground-based GW interferometers currently operational in the world: aLIGO Hanford, aLIGO Livingstone, AdV, KAGRA and GEO600. LIGO, or the Laser Interferometer Gravitational-Wave Observatory, consists of two identical interferometers, one in Livingston, Louisiana, and the other in Hanford, Washington. Advanced Virgo (AdV), the VIRGO interferometer, is a gravitational-wave observatory located near Pisa, Italy. The collaborations between VIRGO and LIGO allows to localize and study the sources of gravitational waves. KAGRA, or the Kamioka Gravitational Wave Detector, is a gravitational-wave observatory located in the Kamioka mine in Japan. It operates on the same principles as LIGO and VIRGO but employs some unique design features like its underground location, which helps shield it from various environmental influences, and the

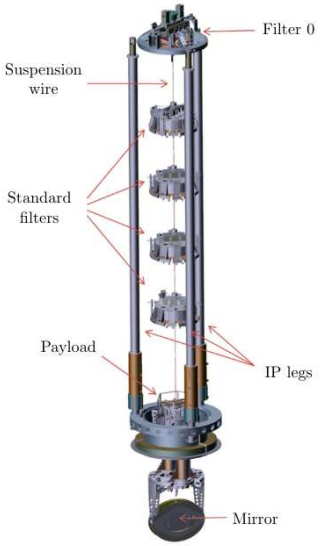

Figure 2.4: The four stage inverted pendulum system acting as suspension for the ineteferometer core optics

use of cryogenic technology to reduce thermal noise in the interferometer. The GEO600 (GEO stands for "German–British Gravitational Wave Detector") is a gravitational-wave observatory located near Sarstedt, Germany.

2.2.3 Noises in GW Interferometers

The amount of events gravitational waves interferometers are able to detect is dictated by the maximum strain sensitivity of the instrument. This can be understood in terms of the smallest signal that can be distinguished against the noise floor of the instrument and can be quantified in terms of signal-to noise ratio or SNR. The characterization and the minimization of all noise sources is therefore one of the main tasks in the design and in the commissioning of the interferometer. The collective performances of the systems composing the interferometric apparatus are summarized in the sensitivity curve $S_x^{1/2}(\omega)$ of the instrument: the output strain of the detector by summing all the noise sources in input without any real signal as a function of the frequency the square root of the power spectral density (PSD) of the detector output in absence of any detection event. As an example the sensitivity curve for Advanced Virgo can be seen in figure 2.6. As per [11] the PSD of a stationary process can be calculated as the Fourier

Figure 2.5: Pictures of four GW interferometers from around the world. Upper left: LIGO-Hanford (Washington State). Upper right: Kagra site rendering (Japan). Bottom left: VIRGO (Italy). Bottom right: LIGO-Livingstone (Louisiana)

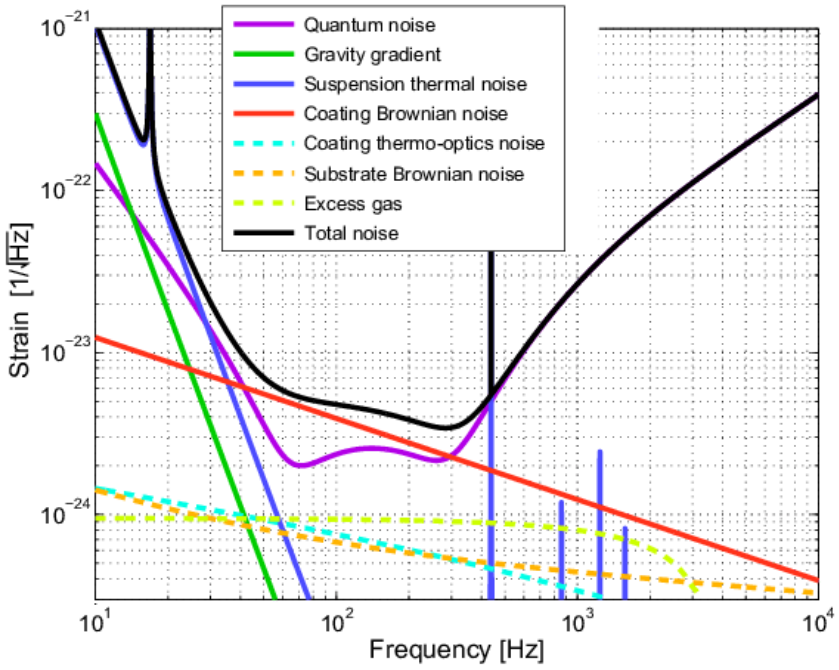

Figure 2.6: Advanced Virgo sensitivity curve from [83]. The different colored lines represent the estimated noise contribution from each different noise source.

transform of its autocorrelation function $C(\tau)$:

$$S_x(\omega) = \int_{-\infty}^{+\infty} C(\tau) e^{i\omega\tau} d\tau \tag{2.24}$$

The main quantity measured by GW interferometerss is the strain i.e. the relative length variation $\Delta L/L$ induced by the gravitational wave. Since we are interested in the strain amplitude, the characteristic PSD of the noise sources is usually converted in an Amplitude Spectral Density (ASD) $S_x^{1/2}(\omega)$ that has units of $1/\sqrt{Hz}$. Obviously the lower the sensitivity curve the higher the Signal to Noise ratio (SNR). A high SNR is highly desirable because this parameter ultimately determines the portion of observable Universe that is sensed by the GW interferometers. At present the noise floor is between 10^{-24} and 10^{-23} $1/\sqrt{Hz}$, allowing to probe signals with a signal-to-noise ratio ~ 8 from a sphere with a radius of the order of the hundreds of MPc, i.e. about 0.3 billion of light years (approx. 100 times the distance from the Andromeda galaxy and about 200000 times the distance from the closest known star-black hole binary, Gaia BH1).
The fundamental Noises one needs to tackle in an interferometer are:

- **Quantum Noise**: Noise relative to the quantum nature of light; it can be divided into two components:
  - Shot Noise: Arises from the discrete nature of photons. It is related to the statistical fluctuations in the number of photons detected and can limit the precision of the measurement in all frequency band.
  - Radiation Pressure Noise: Results from the quantum fluctuations in the electromagnetic field causing random forces on the mirrors, leading to displacement noise. It can limit the sensitivity band especially at low frequencies.
- **Seismic Noise**: Vibrations or movements in the Earth's crust can shake the interferometer's mirrors and optics, leading to unwanted signals. Seismic isolation systems are employed to mitigate this noise.
- **Gravity Noise**: Fluctuations in the local gravitational field due to density variations in the Earth, such as changing atmospheric pressure or ground motion, can can displace directly the interferometer's mirrors.
- **Thermal Noises**: All the noises related to stocastic vibrations of matter at finite temperature; the two dominant contributions being:
  - Coating Brownian Thermal Noise: At finite temperatures, due to the thermal vibrations of the atoms constituting the coating layers, the mirror surfaces experience thermal motion. This motion

introduces fluctuations in the position of the mirrors, contributing to noise in the interferometer.

– Suspension Thermal Noise: Mechanical noise arising from the suspension system that holds the mirrors. Any mechanical imperfections or vibrations in the suspension can affect the interferometer.

As per figure 2.6 we can see how different spectral region are dominated by different kind of noises in particular the main ones being: the suspension thermal noise at low frequencies, the coating Brownian thermal noise at mid frequencies and the quantum noise mainly at high frequencies. In particular the Thermal noises are currently the main concern since they are the limiting contributions in the spectral region of greatest sensitivity. A more in depth explanation of Thermal noise and in particular how it arises and can be measured in coatings will be given in section 7.1.

2.2.4 Future GW interferometers

Many of the noise sources affecting the current GW interferometers are inherent to their design and are so very hard to tackle. Moreover, as seen in subsection 2.2.1, the length of the arms influence the type of events we are able to detect and the amplitude of the interferometer signal. For these reasons, and for the need to increase the network of active interferometers to diminish the amount of blind spots across the celestial sphere, many projects exist to build new generation GW interferometers.
Among the many projects a few of the most notable ones and most likely to be built in the forseable future are: the European plan for Einstein Telescope (ET) [3], the American plan for Cosmic Explorer [4], the indian plan for LIGO-India [6], and the European plan for Laser Interferometer Space Antenna (LISA) [5]. ET will be an underground cryogenic detector planned to be built in the next decades. The main improvements this detector will implement will be a 10 km arm length, a three detectors triangle geometry, the capabilty to operate in two different frequency bands, and a cryogenic temperature operation. Cosmic Explorer will be a detector with 40 km arms. LISA will be a space-based detector with the aim to detect from 10^{-4} to 10^{-1} Hz, it will have 2.5 million km arms made by three orbiting satellites.

2.3 Coatings for GW interferometers

The mirrors of the GW interferometers are fabricated from large test masses in bulk SiO_2 weighting about 40 kg with a diameter of 35 cm. Those test masses are finely polished to be atomically flat and finally a Bragg dielectric mirror is realized by depositing on their surface a stack of alternating optical layers made of two coatings with different refractive indexes. The extreme

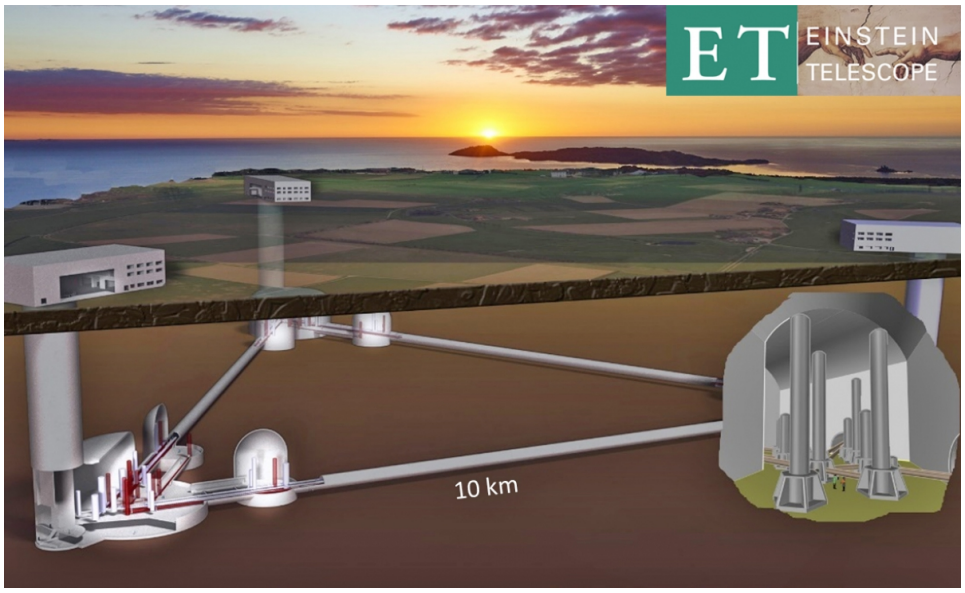

Figure 2.7: Concept image for the construction of Einstein Telescope (ET) a new kind of GW interferometers that is planned to be built in Europe in the next decades.

sensitivity which the GW interferometers are designed for poses highly demanding requirements on the coatings. On one hand, the mirrors have to be highly transparent. Due to the high optical power circulating into the interferometer cavities (750kW in the Virgo case), even a small absorption may lead to unwanted heating, with subsequent thermo-optical effects and degradation of the optical properties. On the other hand, it would be highly desirable to get mirrors contributing as little as possible to the thermal noise.

At the time of writing all the GW interferometerss adopt high reflection (HR) coatings for the core optics produced at the Laboratoire des Matériaux Avancés (LMA) in Lyon, France [7]. Said reflectors are obtained by the ion beam sputtering technique alternating high and low refractive index materials. The material currently in use are SiO_2, commonly referred as *silica*, as a low index material and Ti:Ta_2O_5, commonly referred as *titanium doped tantala*, as the high index one [25].

As per the previous section, the main noise source in the central detection band of the interferometers is the Coating Brownian Thermal noise hence the research on this topic is of the upmost importance: even a small improvement on the coating performance in this respect will result in a big improvement of the amount of space we are able to explore using the GW interferometers. The Coating Brownian Thermal noise spectral density $S(\omega, T)$ can be estimated trough the Fluctuation Dissipation theorem (see

section 7.1) as:

$$S(\omega, T) = \frac{4K_b T}{\pi^{1/2} w \omega} \frac{1-\sigma^2}{Y} \phi \tag{2.25}$$

where w is the width of the laser beam on the mirror, σ the Poisson ratio, Y the Young modulus, and ϕ the loss angle of the mirror (a measure of the energy dissipation see section 7.1). Current coating research focuses in finding materials whose mechanical properties lower the thermal noise. As the moment of writing the tantala layer of the multilayers has been identified as the main responsible for the mechanical losses of the mirrors so the research effort is mostly devoted in finding alternatives for the high refractive index materials.

2.3.1 Strategies to improve GW coatings

The LIGO-VIRGO-KAGRA (LVK) collaboration employs many energies in order to reduce the mechanical losses associated with the mirror's coatings while keeping the optical properties at within the design requirements. The main strategies currently adopted involve the search for different high-index materials, the study of different geometries of the Bragg's reflectors (for example using three materials instead of two), the study of new deposition and post-deposition treatments to improve the properties of the coatings, the research on single-crystalline epitaxial multilayers and so on.
This thesis work wants to explore the possibility to reduce the thermal noise of the coatings by inducing the formation of a controlled dispersion of crystallites inside the amorphous matrix. In traditional optical applications, coatings materials are commonly used in their amorphous state since the presence of crystalline grains act as a source of scattering. On the other hand, however, it is known that crystalline materials generally exhibit a lower thermal noise compared to their amorphous counterpart. The basic idea of this work is therefore to explore the possibility of creating an engineered dispersion of crystalline grains in order to improve the coating noise, while keeping optical scattering losses under control. This research entails the study of the crystallization process in amorphous optical coatings, the measurement of the noise performance and the evaluation of the scattering properties. All those aspects will be detailed in the following chapters.

Chapter 3

Samples production and characterization

3.1 Samples Production techniques

3.1.1 Ion Beam Sputtering Deposition

The current GW detectors around the world employ high reflective coatings deposited via ion beam sputtering (IBS) [15] [84] [85]. For the VIRGO interferometer and for both the LIGO's ones, the sole provider of these coatings is currently the Laboratoire des Materiaux Avances (LMA) situated in Lyon.
In conventional sputtering processes a target of the material one wants to deposit is placed in a vacuum chamber together with the substrate onto which one wants to deposit the coating. Between the two an high voltage is applied such that, upon introducing a gas inside the chamber this ionizes and impinges onto the target material. The ions, accelerated through the electric field, induce a sputtering of the target atoms and molecules that are ejected covering the whole chamber.
Ion beam Sputtering (IBS) is a variant of standard sputtering techniques. In this case an ion beam is created by a suitable source and accelerated towards the target with typical energies the order of 1 keV and currents in the hundreds 100 mA - 1 A range. In this way one can set independently the ion beam energy and current, which allow for a great control on the parameters of the sputtered species. With respect to other deposition techniques, IBS is able to deposit the highest optical quality films regarding their extremely low optical loss (absorption, scatter) and roughness, high density, and very high thickness homogeneity [85] [84]. In the case of oxides coatings, the deposition chamber can be filled with a controlled amount of oxygen, to induce reactive sputtering. The main drawbacks of IBS are the facts that there is low control on the material stoichiometry, and the long deposition

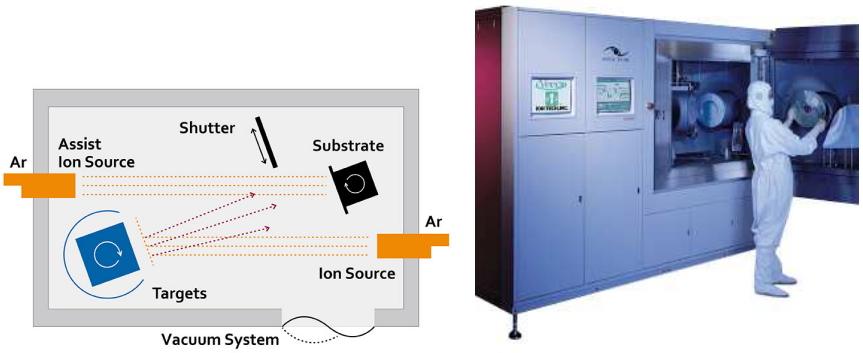

(a) (b)

Figure 3.1: a) Scheme of the Ion Beam Sputtering process b) The Veeco's SPECTOR, one of the machine used for the depositions of this work

time required to produce the coatings.
Three different machines are available at LMA for depositions:

- *Veeco's SPECTOR:* a commercial machine equipped with a single ion source and an assistance source (ion gun) directed towards the substrate. The ion gun is used to clean the substrate surface prior to the deposition and to assist the deposition process by providing additional energy to the sputtered species when they attach to the substrate.
- *Dual IBS (DIBS):* a custom machine, similar to the previous one, equipped with two different ion sources in order to deposit combined materials.
- *Grand Coater (GC):* one of the biggest sputtering machines in the world (two 35 *cm* diameter substrate can be placed inside it simultaneously), customly developed for the deposition of the mirrors of GW interferometers.

In the deposition of the samples used in this work an Ar atmosphere was used to sputter the target combined with a flux of O2 in order to correct the stoichiometry of oxide coatings. The Ar+ beam, before impinging on the target, is neutralized by a neutralizer that diffuse electrons to minimize the charging effects during the deposition. To improve the uniformity of the roughness and the thickness of the coatings the substrate are mounted on a planetary revolving sample holder.

3.1.2 Oven Annealing

Thermal treatments are one of the most simple and effective ways to improve the optical and mechanical properties of a coating. Indeed the standard

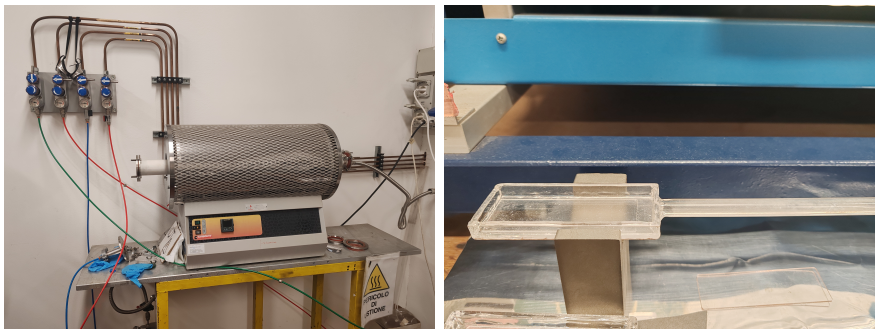

(a) (b)

Figure 3.2: a) Example of one of the oven used b) Quartz vessel

procedure adopted at LMA to produce the mirrors coatings for the GW interferometers include an annealing performed in air of 10 hours at 500°C for standard coating materials (Ta_2O_5 and Ti:Ta_2O_5).

In this work these kind of annealing were performed with a set of three different tubular furnaces. In each of these ovens a quartz vessel is used to hold the samples in the exact center of the oven since an error of few centimeters on the sample placement could lead to several tens of degrees of error on the treatment temperature.An example of one of the oven used can be seen in figure 3.2 as well as the quartz vessel used to place the samples. Each one of the oven used has been calibrated through the use of a thermocouple measuring not only the internal temperature reached but also the spatial uniformity of the temperature inside the oven. Three different oven models were used however, whenever possible, it was tried to preserve continuity between the oven model and the material studied to minimize the influence of calibration errors. The three oven used, all in Padova's laboratories, are: a Carbolite Gero D-7542, a Carbolite Gero 30-3000, and a Carbolite CTF 12/75/700.

3.1.3 Rapid Thermal Annealing

In the case of short high temperature treatments the heating and cooling ramps can strongly affect the sample and alter the results one want to investigate. A common solution in the semiconductor industry in these cases is to use a Rapid Thermal Annealing (RTA) machine, also known as Rapid Thermal Processing (RTP) machine. In this work a commercial RTA Jipelec Jetfirst 150 in Padova was used.

This RTA is a cold wall furnace with the capacity to process wafers up to 6 inches, is able to control the atmosphere during the process, and thanks to frequent calibrations of the instrument the maximum temperature error on any point of the sample is estimated at 3°C respect the target temperature

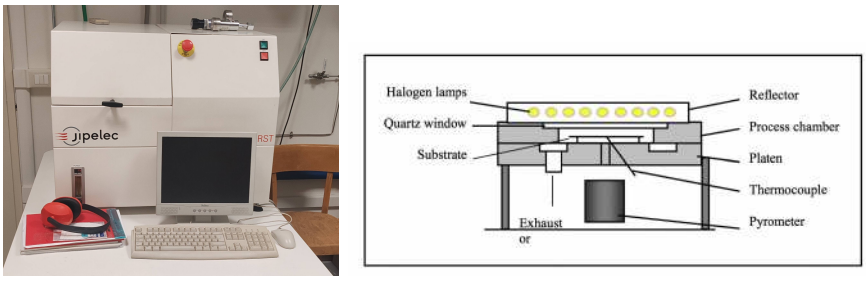

(a) (b)

Figure 3.3: a)The Jipelec Jetfirst RTA used in this work b) Scheme of functioning of the system

when working on a silicon sample (in case of non silicon samples the errors lies in the 5-10°C range [51]). The samples to be treated are placed inside the machine on top of a 6" inch wafer of Silicon that ensure an uniform distribution of the temperature during the use. The heating is provided by 18 halogen lamps placed outside the chamber behind a quartz glass window; the system reaches temperatures up to 1200°C, is able to control heating ramps up to 150°C/s, and is able to cool down in a non thermally controlled way the samples with a similarly fast cooling rate. The lamps are controlled by a feedback system that measures either via a thermocouple or via a pyrometer the Si wafer temperature. The process chamber is completely isolated and connected to a vacuum pump that reaches a vacuum level of 10^{-4} mbar; the process atmosphere can then be modified by flow-meters connected to N2 and O2 gas tanks. The machine allows to program complex treatment recipes with multiple heating phases and control of many parameters like the thermal ramps, the process temperature, the gas fluxes and their venting procedure.

3.2 Characterization techniques

3.2.1 Grazing Incidence X-Ray Diffraction

To probe the inside structure of a material in a non invasive way one of the best option is to employ the interaction of X-ray with matter. A variety of techniques exist each one relying on a different interaction; in this work the main one used was the X-ray diffraction (XRD).
XRD analysis of thin films proved to be the most important technique through the course of this work; as it will be explained later, to maximize the signal coming from the film under analysis, the type of measurement performed takes the name of *Grazing Incidence X-Ray Diffraction (GIXRD)*.
In XRD experiments the fact that the photons wavelength is comparable with the inter-atomic distances, combined with a Thomson-like elastic scat-

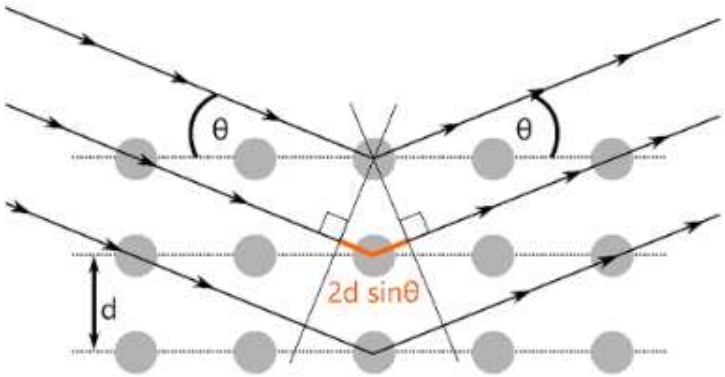

Figure 3.4: Visual representation of Bragg law. Courtesy of [52]

tering process from the electrons of the atoms composing the film to be studied, allows the rise of interference phenomena related to the spatial distributions of the atoms between the scattered photons. XRD phenomena arise with the increase degree of order between the atoms of a material and produce strong discrete diffraction peaks that can be employed to study crystalline materials. In a crystal, atoms are organized in periodic planes and the fundamental rule one must consider is the Bragg's law that relates the photons wavelength λ and their incidence angle θ on the crystalline planes, with the interplanar distance of said planes:

$$n\lambda = 2d \sin\theta \tag{3.1}$$

When this equation is satisfied with integer values of n, the conditions are met for a maxima of the constructive interference. A visual representation of Bragg's law can be seen in figure 3.4.

An instrument built to measure the pattern of the X-ray diffraction is usually called a *diffractometer*. There exist multiple standard configuration of such an instrument; among them one of the most common, and the one of interest in this work, is the Parallel Beam geometry. In this configuration both the X-ray source and the detector are placed on the same circumference whose center is on the sample surface; the main advantage this configuration allows respect the others is the increase in instrumental resolution compensated by a slight reduction in the intensity of the diffracted signal. A scheme of the geometry used and a picture of the instrument are available in figure 3.5

XRD Measurement in this work have been performed using a Philips MRD diffractometer, located in Padova, equipped with a Cu tube, operated at 40 kV and 40 mA. The probe beam was collimated and partially monochromatized to the Cu K-α line by a parabolic multilayered mirror and a metallic slit, the detector was equipped with a parallel plate collimator as

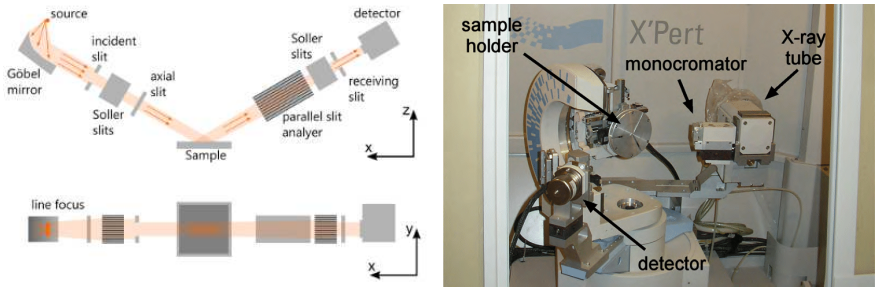

(a) (b)

Figure 3.5: a)Scheme of a diffractometer Parallel Beam geometry, courtesy of [52] b) Picture of the Philips MRD diffractometer used.

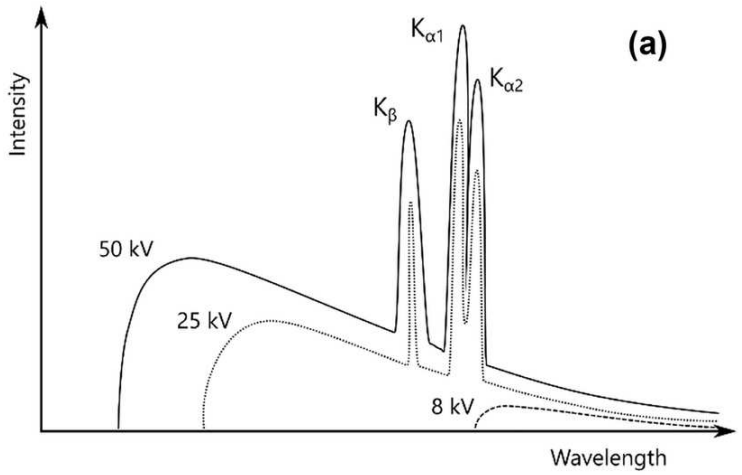

Figure 3.6: Example of an X-ray beam energy spectrum for different acceleration voltages of the X-ray tube. Image courtesy of [52]

well as a Soller slit. The text that will follow will cover only the principle of functioning of the elements actually used in our setup.
The X-ray beam originates from a vacuum tube where a strong current passing through a metallic cathode creates the emission of electrons that, accelerated through an electric field, impinge on a copper anode target. This electron flux cause the Cu atom to ionize in an excited state and, subsequently, leads to a photon emission. The emission spectrum (for which an example can be seen in figure 3.6 is dominated by the K family of emission lines and in particular the three main lines observable are the $K\alpha_1$, $K\alpha_2$, and $K\beta$ respectively at 1.54059 Å, 1.54443 Å, and 1.39223 Å. Occasionally, when the life cycle of the tube approaches its end, this spectrum can became contaminated by the K emission of the cathode filament whose atoms slowly contaminate the copper target. The light directly exiting the X-ray

tube is unsuited to an XRD experiment being both non-monochromatic and not focused on the sample. A first diffraction slit reduces the angular divergence of the beam and, if a lower intensity of the beam is needed during the experiment, a metallic beam attenuator is placed right after it. The choice of using a metallic attenuator rather than lowering the X-ray tube emission intensity comes from the fact that the life-time of an X-ray tube shortens faster if its current and voltage operation conditions, both related to the intensity of the x-ray beam produced, are changed.
After this first stage the beam passes through a Göbel parabolic multilayer mirror that strongly reduces the angular divergence of the beam and, most importantly, suppress the intensity of the $K\beta$ line by around 95%. While the $K\beta$ is almost suppressed by the mirror, the $K\alpha_1$ and the $K\alpha_2$ lines are too close in wavelength and, to further monochromatize the beam, a dedicated additional monochromator would be required. Except for very specific applications, however, this is usually not necessary and avoided since it comes at the cost of a reduction of the beam total intensity (see subsection 3.2.3 for an example of measurement at higher resolution).
The now collimated X-ray beam impinges on the sample surface. As previously described to originate a diffraction phenomena the incidence angle on the crystalline planes must exactly satisfy Bragg's law. In the case of a single crystal material this means that each lattice plane family give rise to a different diffraction peak accessible only at a specific angle between the beam and the sample. This condition translates into the needs for the diffractometer system to have enough degree of freedom such that the angles between the source, the sample, and the detector can satisfy Bragg's law for an arbitrary plane family. In our system this is ensured by having the sample stage mounted on a six axis goniometer able to perform independently the three translations and the three rotations. Given a single crystal with a specific orientation there exist only one position of the elements of the diffractometer able to access a certain diffraction peak and a great attention is required in aligning the sample. The situation becomes far more easier when dealing instead with polycristalline samples. In this case in fact, due to the presence of an enormous amount of crystalline domains each one with its own orientation, to excite a specific crystalline plane family it's no longer required a specific incidence angle since a portion of the material grains will always be aligned in the right way. When dealing with polycrystalline samples then only the angle at which the detector is positioned becomes relevant to investigate a material. The common convention refers to the incidence angle of the beam onto the sample surface as ω (with $\omega = 0°$ when the sample surface is parallel to the X-ray beam) and the detector angle as 2θ (whith $2\theta = 0°$ when the detector is placed in front of the beam). This notation has been used in literature to firstly decouple the incidence angle from the scattering angle and secondly to highlight the fact that the detector position always correspond to the double of the Bragg's angle for

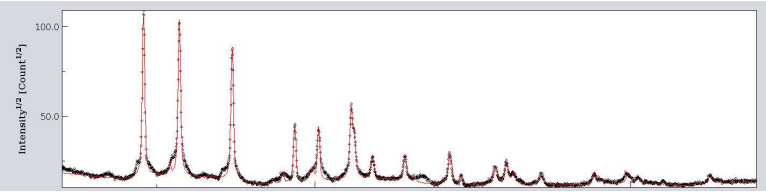

Figure 3.7: Example of a GIXRD measure. The red line is a least square Rietveld regression obtained via MAUD software [53]

the diffraction peak under analysis (the other sample's angles take the name of ϕ for the sample rotation on an axis perpendicular to the sample surface and χ for the rocking rotation).
The typical penetration depth of X-rays into matter ranges from a few microns up to hundreds of microns depending on the material under examination however, when dealing with a thin film, the thickness of the film is usually much smaller then the penetration depth. In order to maximize the signal coming from the thin film and reducing the background contribution from the substrate it is then common to implement a *Grazing Incidence X-Ray Diffraction (GIXRD)* configuration in which ω is kept constant at a low value exploiting the fact that the path of the beam goes as the inverse of the sine of the incidence angle. In GIXRD measurement then one perform a scan moving only the detector and so a diffractogram function only of 2θ is obtained. Varying the incidence angle as said changes the penetration depth of the X-rays in the material; by performing multiple 2θ-scans at different ω angles one can investigate, even if in a non very sensitive way, the homogeneity of the material across its thickness. An example of a GIXRD diffractogram can be seen in figure 3.7

The X-rays diffracted by the sample are collected by a proportional counter Xe detector. In our setup we mount a point detector meaning that each position of the detector directly correspond to a single point of the diffractogram (other options are possible like line detectors and area detectors). The detector, as the name suggest, is a Xenon filled ionizing chamber able to convert the X-ray radiation into an electrical current that is proportional to the intensity of the collected beam. The measure is given in counts per seconds (cps) although, since the intensity of the diffracted radiation depends on a multitude of factors related both to the instrument and the sample, diffractogram are often presented in arbitrary units on the y axis. The detector used posses a rather big acceptance angle (around 1 degree in 2θ) so in order to reduce its angular acceptance a Parallel Plate Collimator (PPC) is placed in front of it. A PPC is an object composed of several metal plates tightly spaced and placed perpendicular respect the plane defined by the X-ray source, the sample, and the detector. A similar function is provided by the *soller slit*, a smaller version of a PPC but placed

perpendicularly to it. While the former is required mainly to reduce the detector angular acceptance to increase the instrumental angular resolution, the latter provides a reduction of the angular divergence of the beam along the direction perpendicular to the scattering plane and it's used to remove unwanted background from the measurement.
Hidden inside a diffractogram there are multiple physical information regarding the sample studied however to retrieve them is a delicate process. The main properties accessible are the peaks positions, intensities, and shapes. This properties relate in a non trivial way to both the sample and the instrument used. A useful summary of their relation is shown in the following table [54]:

Property	**Microstructure**	**Macrostructure**	**Instrument**
Position	unit cell	Absorption Porosity	X-ray wavelength Alignment Beam divergence
Intensity	Atomic parameters	Preferred orientation Absorption Porosity	Geometry X-ray polarization
Shape	Crystallinity Disorder Defects	Grain size Strain Stress	X-ray line width Geometry Beam conditioning

Table 3.1: main XRD spectra components and their relation to instrumental and sample properties

The method commonly used to estimate this properties is called *Rietveld refinement* [57] and it's a least square regression of the full XRD spectra based on modelling how each one of the effects reported in table 3.1 affects the spectra. In the subsequent text only the main concepts of this approach will be described. For a more in depth explanation refer to [58].
In this technique the diffractogram considered as a set of measured intensites as a function of the detector position $h(2\theta)$ is expressed in a formal way as the convolution between two contributions: the sample characteristic diffraction pattern $f(2\theta)$ and the instrumental response $g(2\theta)$. Adding a general background $b(2\theta)$ we can write:

$$h(2\theta) = f(2\theta) \otimes g(2\theta) + b(2\theta) = b(2\theta) + \int_{-\infty}^{+\infty} f(\alpha)g(2\theta - \alpha)\mathrm{d}\alpha \qquad (3.2)$$

The information we want to access regarding our samples are encoded inside the f function however in general it's very complicated to separate the individual contributions of the f and g function in order to do so.

In the most general form the sample diffraction pattern can be written as the sum of a series of peaks each one characterized by a different position x_i, width σ_i and intensity I_i.

$$h(2\theta) = \sum_i P(x_i, \sigma_i, I_i) \tag{3.3}$$

The pattern described by the peaks positions it's characteristic of the specific structure of the material under investigation so a phase match of the experimental data against a database can be performed to identify a crystalline structure from it's spectrum. We used for this purpose the QualX software [59] with the PDF2 database [60]. Looking more deeply to the shape of these peaks what one finds is that the instrumental contributions produce a Gaussian shape of the peaks while the sample ones produce a Lorentzian shape. The general peak function assumed by diffraction peak is then a convolution between a Gaussian and a Lorentzian function however such a shape it's not analytical and so risk to significantly slow down the computation required in the refinement process. The common approach is then to model the diffraction peak as linear combination between a Lorentzian and a Gaussian function:

$$P(x) = \eta(x) G\left[x, H_G(x), I_G(x)\right] + (1 - \eta(x)) L\left[x, H_L(x), I_L(x)\right] \tag{3.4}$$

with H_G, H_L representing respectively the Gaussian and the Lorentzian peaks half-width half-maximum and I_G, I_L their intensities and η the degree of mixing between the two.
The instrumental response main effect is to produce a broadening of the diffraction peaks. Such effect is usually described trough the use of the *Caglioti* formula [55] that describes how the half-width at half-maximum of a peak changes as a function of the Bragg's angle:

$$H_G^2 = U \tan\theta^2 + V \tan\theta + W \tag{3.5}$$

Regarding the sample broadening effects they are mainly related to crystallites sizes and can be modeled through the use of the Scherrer's equation [56]:

$$\Delta H_L = \frac{K\lambda}{\tau \cos\theta} \tag{3.6}$$

where K is a dimensionless factor related to the shape of the crystallites, λ is the wavelength used, and τ is the mean size of the crystallites. Adding also the influence of the defective structure of the crystallites we can define a new quantity, the microstrain ϵ defined as the standard deviation of the values of the lattice parameters across the whole sample region examined. The Lorentzian halfwidth accounting also for this effect can be expressed as:

$$H_L = \frac{K\lambda}{\tau \cos\theta} + 4\epsilon \tan\theta \tag{3.7}$$

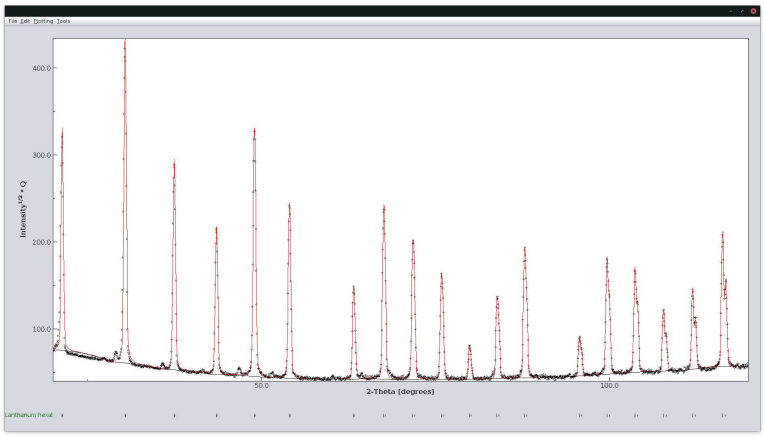

Figure 3.8: Lab6 Diffractogram. The red line is a least square Rietveld regression obtained via MAUD software [53]

Relying on the fact that the instrumental contribution is constant across different samples if we can find a sample with a known reference XRD spectra we can use it to characterize the instrumental response and estimate the U, V, W, and η parameters of our instrumental configuration. There exist multiple standard to perform such an operation, in this work a LaB6 standard powder provided by the NIST was used. The LaB6 powder firstly has an high number of diffraction peaks among the whole angular range allowing to thoroughly characterize the instrument response; secondly the powder chosen has big crystallites sizes with low degree of defects such that the Lorentzian contribution of the peak broadening can be neglected and only the Instrumental contributions are left for evaluation. The diffraction spectra of the LaB6 spectra as well as its modelling can be seen in figure 3.8. Calibration of the instrument was performed with the use of a PPC and a 0.04 rad soller slit, with a diffraction slit of 1/32 degree and an angle of incidence of 1 degree. Rietveld refinement in this work was performed by the aid of MAUD software [53].

3.2.2 in-situ GIXRD

As one of the main objective of this thesis is to investigate the crystallization kinetic, the possibility of following the evolution of the crystal structure of the material during an heating treatment was extremely interesting. To accomplish such a feat our diffractometer was equipped with an Anton Paar DHS900 (figure 3.9) thermal stage able to reach up to 900°C.
Since during an heating process the sample is undergoing evolution one must balance the XRD spectra acquisition time against the evolution in progress i.e. the time the instrument spend to acquire a measure must be negligible respect the time scale of the changes happening. In our measurement pro-

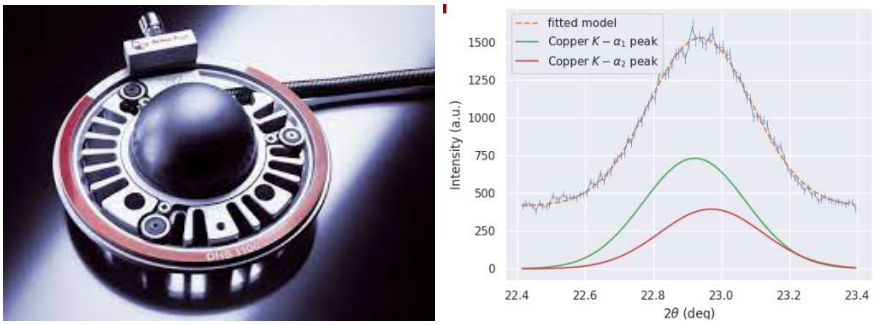

(a) (b)

Figure 3.9: a) AP DHS900 module used for *in-situ* GIXRD, b) Example of one of the single diffraction peak acquired during *in-situ* GIXRD measure and its fit

tocol this was achieved by limiting the acquisition of the diffractogram to just a single diffraction peak. An automatic procedure was then devised to fit the peak using the same instrumental parameters found from the LaB6 Rietveld calibration.

3.2.3 X-Ray Reflectivity

A useful technique to investigate a thin film thickness, density and roughness is the X-ray Reflectivity (XRR).
Let's consider a spherical wave with wavevector **k** propagating in free space from the origin that passes through an homogeneous slab of material with a different index of refraction n and thickness Δ. The passage of the wave through this region causes a phase shift to be introduced due to the difference in refraction index; we can write the refracted wave in a generic point **r** as:

$$\psi = \frac{e^{i\mathbf{k}\cdot\mathbf{r}}}{r}\left[1 + ik(n-1)\Delta\right] \tag{3.8}$$

In the keV energy range, the typical energy scale of an X-ray tube, the main interaction between X-rays and matter is the Thompson elastic scattering with the atomic electron clouds. If we calculate the process of interaction of the wave with the material's electrons the same refracted wave as before in the point **r** can then be calculated as[74]:

$$\psi = \frac{e^{i\mathbf{k}\cdot\mathbf{r}}}{r}\left[1 - i\frac{2\pi\rho r_e\Delta}{k}\right] \tag{3.9}$$

with ρ_e the electron density of the material and $r_e = 2.18794 \times 10^{-15}\ m$ the classical electron radius. Imposing the two previous equation to be equal one obtains:

$$n = 1 - \frac{2\pi\rho_e r_e}{k^2} = 1 - \frac{\rho_e r_e \lambda^2}{\pi} = 1 - \delta \tag{3.10}$$

Since the index of refraction is always smaller then 1 when the X-ray impinge on the interface between vacuum (or air) and a physical medium at a small angle undergo the phenomenon of total external reflection, i.e. the beam is completely reflected from the interface and the transmitted component has an exponentially decaying behavior with a penetration depth which is generally very small (typically a few nm). The critical angle at which this phenomenon occurs is:

$$\theta_c = \sqrt{2\delta} = \sqrt{\frac{4\pi\rho_e r_e}{k^2}} = \sqrt{\frac{\rho_e r_e \lambda^2}{\pi}} \tag{3.11}$$

By measuring the critical angle at which the external reflection appears one then directly measure the electronic density of the material. This quantity, if the stoichiometry of the sample is known, is a function of the material density ρ and one can then write:

$$\rho = \frac{\rho_e}{N_A} \frac{\sum_i c_i M_i}{\sum_i c_i f_{1,i}} \tag{3.12}$$

with N_A the Avogadro's number, c_i the stoichiometric coefficients of the atomic specimen present in the material, M_i the atomic masses of said atoms, and $f_{1,i}$ the real part of their atomic scattering number (a measure of the amplitude of the wave scattered by a single atom of the specimen considered at the target wavelength).
If one measure the absolute specular reflectivity of a sample, i.e. the ratio of light reflected by the surface with respect to the incident amount, as a function of the incident angle then this function will remain equal to 1 until the critical angle and then start to decrease exponentially since when the incidence angle becomes greater then the critical angle the X-ray wave start to penetrate inside of the material. The rate at which the reflectivity decays is connected to the quality of the material surface and can be used to estimate its roughness. When the thickness of the material is smaller than the penetration depth of the wave interference phenomena from the waves refracted at the two surfaces of the material start to happen. This result in two main effects: the decay of the reflectivity becomes tied not only to the roughness of the front surface but also to the roughness of the back one and to the material absorptivity, and interference fringes called *Kiessig fringes* appear whose period is related to the the total thickness of the material. An example of a typical XRR measurement of a sample in which some fringes are visible can be seen in Figure 3.10

The XRR measurement requires an higher degree of resolution respect to the GIXRD ones: the critical angle ranges usually between $0.1° - 0.3°$ and the decay of the reflectivity happens in the span of $1° - 2°$; moreover, since the Kiessig fringes are inversely related in their spacing to the thickness, the higher the instrumental resolution achieved the greater the maximum

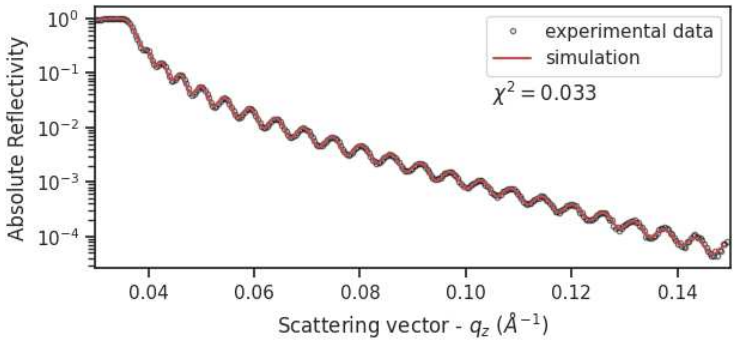

Figure 3.10: Example of a typical XRR measurement. In the region before the critical angel (around 0.03 Å) the sample experience total reflection and the absolute reflectivity remains constant. The oscillations visible from 0.04 Åonwards are Kiessing fringes due to the thickness of the sample creating inteferences phenomena.

material thickness measurable. To this scope the diffractometer configuration described in subsection 3.2.1 is changed by placing a an high-resolution four-bounce symmetric Bartels monochromator right after the Göbel mirror and the PPC is replaced with a three-bounce symmetric analyzer; both this devices exploit the Bragg diffraction from the (2 2 0) crystallographic planes of near perfect Ge crystals to improve the resolution up to $1 \cdot 10^{-4}$ degree. The data acquired are analyzed through the use of REFLEX software [67].

3.2.4 Pair Distribution Function analysis

All the diffraction methods described in 4.3.2 are appropriate for the study of already formed crystalline grains. However, in order to study the very initial moment of the grains formation, it is necessary to use a different approach, adequate to study both crystalline and amorphous materials. This approach consists in measuring the atomic pair distribution function (PDF) of a sample, defined as:

$$G(r) = 4\pi r[\rho(r) - \rho_0] \tag{3.13}$$

where

$$\rho(r) = \frac{1}{4\pi r^2 N} \sum_i \sum_{j \neq i} \frac{b_i b_j}{\langle b \rangle^2} \delta(r - r_{ij}) \tag{3.14}$$

Here, ρ_0 is the atomic number density of the material and $\rho(r)$ is the atomic pair density, which is the mean weighted density of neighbour atoms at a distance r from an atom at the origin. The sums in $\rho(r)$ run over all atoms in the sample, b_i is the atomic scattering factor of the $i - th$ atom,

$\langle b \rangle$ is the average scattering factor and r_{ij} is the distance between atoms i and j.

In this kind of experiments, high energy X-rays are transmitted through a small sample and the diffraction pattern is recorded on a 2D detector X-ray camera placed after the sample. The difference with a standard diffraction experiment is that, due to the high energy of the X-ray beam, the radiation is scattered on a very wide angular range which means that a large portion of the reciprocal space can be explored. In this diffraction pattern, both contribution from Bragg scattering due to crystalline grains and from the amorphous matrix are present, and for this reason this technique is sometimes called *total scattering*. By analyzing the overall diffraction pattern it is possible to reconstruct the PDF, which provides real space information independently on the degree of ordering of the material. In these experiments the variable Q is generally used to measure locations in reciprocal space. Q is the magnitude of the scattering vector and is given by: $Q = \frac{4\pi sin\theta}{\lambda}$, where θ is half the scattering angle (2θ) and λ is the X-ray wavelength. In total scattering experiments, Q has to be as large as possible, up to several tens of Å^{-1}. In contrast, in standard X-ray experiments typically reach a maximum Q of 5Å^{-1} or so. Once the scattering intensity pattern has been collected on the CCD detector, one may perform an integration along the azimuthal angle to obtain a 1D intensity plot vs Q, which constitutes the raw data the analysis begins with. Various mathematical operations are then applied to the data, as described e.g. in [31], but the crucial point is that at the final step the 1D diffraction pattern is Fourier-transformed to get a function of the real space distance r. It can be shown that the resulting function is precisely the PDF defined in 3.13.

The PDF function is a measure of the probability of finding a pair of atoms separated by a distance r. The peaks in the actual function corresponds to interatomic distances that are often encountered in structure under examination (see fig. 3.11).

As explained, total scattering experiments need a high photon energy and a very good signal to noise ratio to be performed, which requires the use of synchrotron sources. The results presented in this thesis work are obtained at the ESRF beamline ID11a in Grenoble. This beamline is operated by an in-vacuum undulator, of which there are two available (U22 and CPM18) differing in period and magnetic lattice. The beam energy is selected by means of a double bent crystal monochromator. The coherence and source size of the beam has been measured as 18.5 micron FWHM vertically. In our experiments the beam energy was set at E = 78.395 keV, corresponding to a wavelength $\lambda = 0.1582$ Å.

The beam is focused at the sample position by means of a Kirkpatrick-Baez mirror to a $1\mu m \times 1\mu m$ area. The experiments were performed by means of a large diffractometer located in the experimental hutch EH3. This hutch contains a high resolution diffractometer, situated 94 m from the

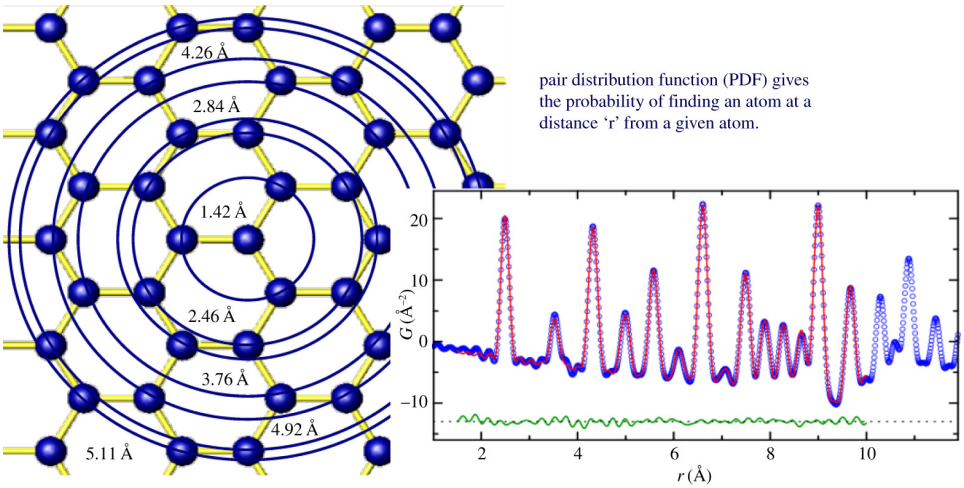

Figure 3.11: A schematic understanding of the PDF. Each atom is placed at the origin and larger and larger circles are drawn. Every time an atom is encountered, a unit of intensity is added to a histogram at the position r that is the radius of the circle at the intersection point. Thermal motion of materials causes the histogram to broaden into a Gaussians, and so the PDF is well represented by a sum of independent Gaussian functions. Image taken from [32].

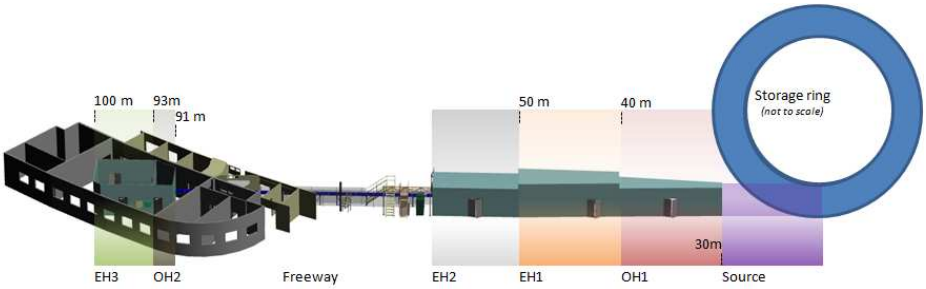

Figure 3.12: A schematic of the ID11 beamline at ESRF. Image taken from [33].

source. The run out of the rotation axis is about 0.8μm, which is compatible with the focal spot size. Granite translations are used to align and scan the diffractometer in the beam, and a granite gantry system holds the imaging detector. The diffractometer has movement in x, y, z, θ, and ω and on it is mounted a sample stage with movement in x, y, z, rx and ry.

On the top of this goniometric system it is possible to mount a furnace for non-ambient measurements. We used this tool to perform real-time measurements of the evolution of the sample PDF at high temperature, in order to clarify the initial stages of the crystallization process. The diffraction

Figure 3.13: The high-resolution X-ray diffractometer in the experimental hutch of the ID11 beamline. Image taken from [33].

pattern has been measured by means of a FReLoN camera suitable for 2D acquisition. This is optimised for very rapid readout, allowing full (2048 x 2048 pixels, 16 bit) frames to be read out in 240 ms, which can be further increased binning or the use of regions of interest.

3.2.5 Raman Spectroscopy

Another useful non invasive technique to investigate the properties inside the bulk of a material is the Raman Spectroscopy. In Raman measurements one excite the target material with a probe laser and analyze the energy spectra of the radiation diffused by it.
As the probing radiation interact with the material it excites the electrons of the material; these electrons subsequently relaxate back and emit photons doing so. If the electron during the process just described ends on a final level different than its initial one the wavelength of the emitted photon will be different from the wavelength of the probing radiation and will carry information regarding the energy difference between the various electronic levels. The difference between the energy of the scattered photon and the energy of the probing radiation is usually called *Raman Shift* and expressed in cm^{-1}. In figure 3.14 the two main processes happening in a Raman scattering measurement, Stoke and anti-Stokes scattering, are depicted. Due

to the energy of the probe radiation being usually in the VIS range the transition excited are usually the vibrational and rotovibrational transitions of the material and is possible so to obtain unique patterns each one related to the interatomic distances and to the atom specimens involved.
The effects of an electric field, like the one of the probing radiation, on a material are encompassed by the polarizability equation:

$$P_j = \epsilon_0 \chi_{jk} E_k \tag{3.15}$$

where χ_{jk} is the medium electrical susceptibility. For a sinusoidal electric field in the form of:

$$E = E_0 \cos(\omega t) \tag{3.16}$$

the vibrational state of the material, excited by the electric field, are also sinuisoidal in the form:

$$Q_n = Q_{0,n} \cos(\omega_n t) \tag{3.17}$$

where $Q_{0,n}$ is the amplitude of the n-th vibrational mode and ω_n its frequency. The effect of the external electric field on the singular vibrational modes of the material can be expressed by writing the electrical susceptibility as a Taylor's expansion over the vibrational modes:

$$\chi_{jk} = \chi_{0,jk} + \sum_n \sum_{i=0}^{\infty} \left(\frac{\partial^i \chi_{jk}}{\partial Q_n^i} \right)_0 Q_n^i \tag{3.18}$$

Truncating the expansion at the first order and combining the previous equations we can write:

$$\begin{aligned} P_j = \; & \epsilon_0 \chi_{0,jk} E_{0,k} \cos(\omega t) + \\ + \; & \frac{1}{2} E_{0,k} \sum_n Q_{0,n} \left(\frac{\partial \chi_{jk}}{\partial Q_n} \right)_0 [\cos(\omega t + \omega_v t) + \cos(\omega t - \omega_v t)] \end{aligned} \tag{3.19}$$

As we can see the electric field produces three main effect on the material: a response at the same frequency of the radiation, the Rayleigh scattering of the material, and two responses at the frequencies $\omega - \omega_v$ and $\omega + \omega_v$, respectively the Stokes and the anti-Stokes processes earlier described. Since the electrical susceptibility is a tensorial quantity, in crystalline materials where it's non isotropic, the response of the Raman measurement becomes dependant also to the relative orientation of the crystalline material and the crystalline lattice orientation and so, as it will be shown in section 4, The Raman measurement can become useful also to assess the orientation of crystalline regions. For a more detailed explanation of Raman scattering processes refer for example to [43].
In this work vibrational properties of the samples were characterized in Padova using a Horiba XploRA Plus spectrometer using a probing laser either at 532 nm or at 785 nm.

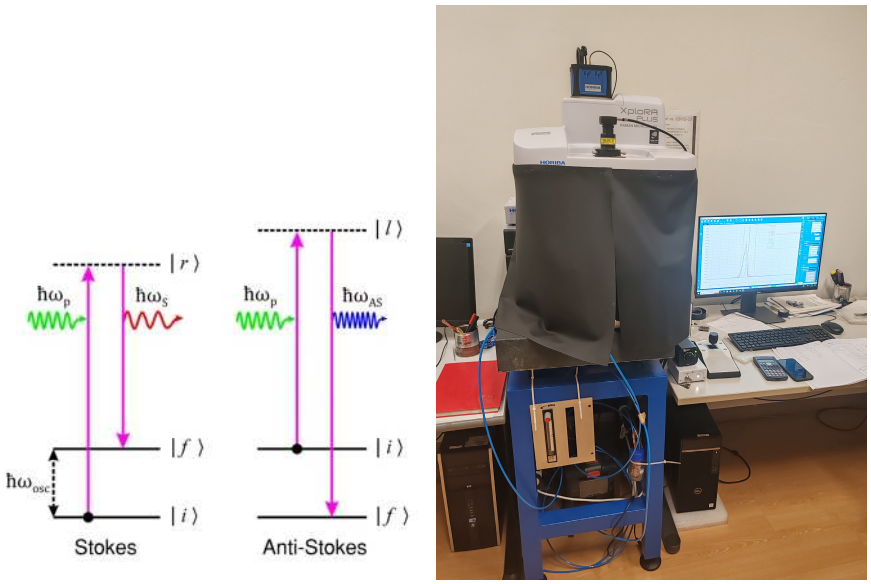

(a) (b)

Figure 3.14: a) Scheme of Raman scattering processes [42] b) The Horiba Xplora Plus spectrometer used.

3.2.6 Atomic Force Microscopy

Among the surface characterization techniques one of the most useful ones is the Atomic Force Microscopy (AFM). The AFM can acquire the topography of a surface with resolution up to the Armstrong level in height and is especially versatile in its application to virtually any kind of material one needs to investigate. The AFM technique is an advanced type of scanning probe microscopy in which a cantilever with an attached fine tip whose end diameter is comparable with the atomic feature one desires to investigate. The AFM working principle relies on the fact that as the tip approaches the material it starts to feel different interactions with the surface like Van der Waals or magnetic forces whose specific nature depends on the specific materials of both the tip used for probing and the sample under study. Cantilever position is monitored trough the use of a laser bouncing on it and impinging back on a four quadrant detector; as the interactions start to affect the tip the cantilever deflects and the laser moves from the center of the detector. This information is used as an error signal that controls a piezo-electric actuator placed below the sample. By a suitable feedback loop the piezo is operated so to keep the error signal close to zero, while the sample is scanned in the surface plane. By measuring the voltage fed to the piezo actuator, it is possible to reconstruct a map of the sample surface, and, in some cases, also to gather additional information like the change in hardness of the material studied, electrical and magnetic properties etc.

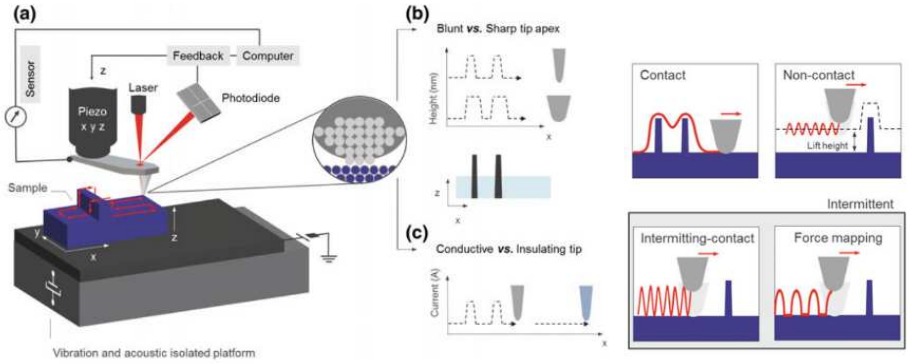

(a) (b)

Figure 3.15: a) General AFM scheme of functioning b) Scheme of the main measurement modes a modern AFM system can work under. Both images courtesy of [44]

Three main modes of operation can be exploited in an AFM measurement: contact, non-contact and intermittent differentiated as the name suggest by whether the tip actually enters in contact with the sample surface and whose case of operation differs mainly by the type of interaction is able to be sustained during the measure. In non-contact mode, the only acquisition mode used in this work, the cantilever is made vibrate to its own resonance frequency and the amplitude and frequency of this movement is continuously monitored. The interactions forces affect both the vibration frequency and the amplitude of the oscillation of the cantilever and a feedback system maintains fixed the distance between the sample and the surface.

Images have been acquired using a Nanosurf FlexAFM visible in figure 3.16. To ensure the maximum image quality the instrument is placed on a leveled table with both an active and a passive dampening system in order to isolate it from the ground and so reduce the vibrations in Padova's laboratories. The tips used for the measurement were 125 μm long silicon tips highly doped to ensure a correct discharge of the cantilever during the measurement, tip radius was garanteed at less then 7 nm, and were coated with a reflective 30 nm Al coating. The tip resonant frequency was 330 kHz, the capacity 42 N/m, and the reflective coating was deposited with low stress resulting in a cantilever bending of less than 2°

3.2.7 Rutherford Backscattering Spectrometry

The main technique used to characterize material composition in this work has been the Rutherford Backscattering Spectrometry (RBS). As the name suggest the technique working principle is based on the the fact that a positive charged particle impinging on the atoms of a materials experience

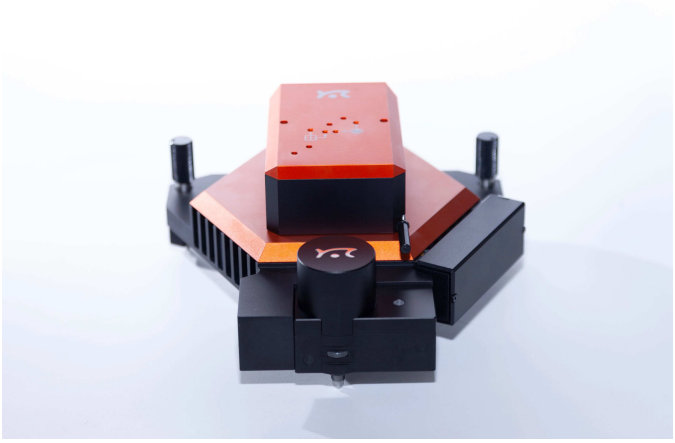

Figure 3.16: The Nanosurf FlexAFM used for measurements in this work

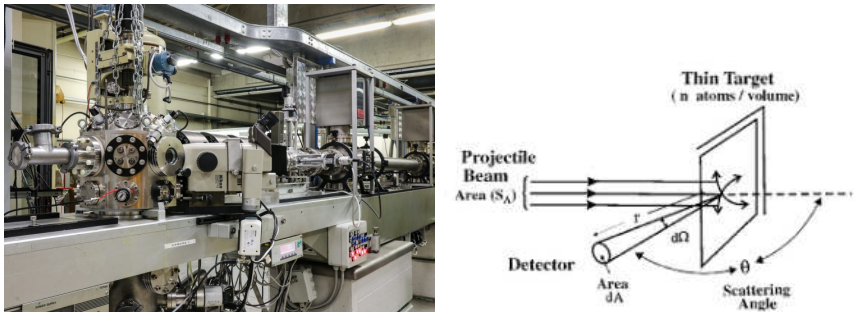

(a) (b)

Figure 3.17: a)AN2000 accelerator at INFN Legnaro National Laboratories in Legnaro (PD) b) Scheme of functioning of the system

a recoil due to interaction of said particle with the nuclei proportionally to their atomic number.
In a standard RBS experiment an accelerator is used to produce an ion beam of light-element nuclei (typically He4+ nuclei), the focalized beam impinges on the target sample to be studied, and an energy sensitive detector with low angular acceptance is placed at an high angle with respect to the beam propagation direction. A scheme of a real setup like the one just described can be seen in picture 3.17.

The observable quantity from the described RBS technique is an energy resolved spectra of deflected particles. This is called RBS yield and can be expressed as:

$$Y(\theta, E) = \sum_s Y_s(\theta, E) = \sum_s N_s Q \Omega_d \frac{d\sigma_s(\theta, E)}{d\Omega} \tag{3.20}$$

where θ is the scattering angle, Q is the total incoming ions number, N_s is

the atomic density of a specific atomic species, Ω_d is the detector solid angle, and $d\sigma_s/d\Omega$ is the differential cross section of each atom species involved in the process. The choice of the incident beam energy as well as the atom nuclei used inside it affects the main type of interaction occurring between the beam and the sample. The aforementioned choice of using light nuclei and a correct energy tuning guarantees that the ions and the sample interact only via the electromagnetic force in an elastic manner. Other variation of this techniques using non-elastic processes or nuclear interactions between the beam and the sample exist but are not of interest for the comprehension of this thesis.
Under the assumption of a pure Coulomb interaction and in the center of mass reference frame we can then rewrite the differential cross section from the equation before as:

$$\frac{d\sigma_s(\theta, E)}{d\Omega} = \left(\frac{Z_b Z_s e^2}{8\pi\epsilon_0 E}\right) \frac{1}{sin^4(\theta/2)}. \tag{3.21}$$

The energy E_1 of the scattered particle can then be written in relations to the atomic masses of the ion beam and the target particle m_b and m_s as:

$$E_1 = E \cdot \frac{\sqrt{m_s^2 - m_b^2 sin^2(\theta)} + m_b cos(\theta)}{m_b + m_s} = E \cdot f(m_b, m_s, \theta). \tag{3.22}$$

When the ion-beam parameters are fixed (i.e. the atomic mass m_b, the charge Z_b and the incoming energy E) the energy of the scattered particle at a certain angle θ depend only on the specific atomic species involved in the process and so a measure of this energy can identify the element involved.
This basic principle of the Rutherford Scattering, however, is more complicated when a real material is involved since the beam, while traveling trough it, interacts multiple times with its atoms and so the energy that reaches each one of them is not a constant. At the MeV energy regime an ion travelling through a material loses energy mainly due to the interaction with the electrons present inside of it and so, in a neutrally charged sample, this energy loss can be tied directly to the atomic species involved and to the depth of travelling of the beam. For each material stopping power functions $dE(E)/dx$ quantifying the energy loss per travel unit length have been defined and empirically determined over large amount of data and are commonly available [45]. From this functions in single-element materials we can define the stopping power for a specific atom species, ϵ, by averaging them over the atom density. For multi-element materials instead, the equivalent stopping power can be well estimated using the Bragg rules that states that it's equal to the sum of the single elements stopping powers multiplied by their own concentration. The stopping power function for an arbitrary

material can then be written as:

$$\frac{dE}{dx} = \sum_i \rho_i \epsilon_i \tag{3.23}$$

With the aid of such functions the energy of the beam at a certain depth can be written as:

$$E = E_0 - \Delta E = E_0 - \int_0^x \left(\frac{dE}{dx}\right) \mathrm{d}x \tag{3.24}$$

The scattering event occurs with initial energy E and deflect the particles with an energy $E_1(E)$ as previously described. This ion travels back trough the material and again interacts with it such as its final energy E_2 is:

$$E_2 = E_1 - \Delta E = f \cdot E - \int_0^{x/\cos\theta} \left(\frac{dE}{dx}\right) \mathrm{d}x. \tag{3.25}$$

In an RBS measurement a detector collects this deflected beam and reconstruct its energy spectra. From this spectra the main physical quantities that can be deduced on the basis of the equations written before are: the stoichiometry, the areal density of the sample, and a rougher estimate of how these two quantities vary as a function of the depth inside of the sample. Since all the information one can estimate from an RBS measurement are all tied together in a tightly manner, the analysis of the data from an experiment of this kind in general is not straightforward and is performed through the aid of a software that simulates the energy spectrum [46].

All the RBS measures in this thesis have been carried on at the AN2000 accelerator at INFN Legnaro National Laboratories in Legnaro (PD), with a 4He+ ion beam accelerated up to 2 MeV and a scattering angle of 160°.

3.2.8 Optical Microscopy

Visual investigation of a sample surface, while lacking the deep insight provided by the other technique presented before, can still be an easy and powerful tool in investigating a material characteristics.

Microscopic images presented in this work have been taken using a Keyence VHX-7000N digital microscope (figure 3.19) able to magnify up to 2500x. The instrument is able to perform basic roughness measurements by the aid of a motorized z-axis as well as reconstruct 3D images of a sample surface. The software coming with the instrument provides numerous analysis tool and in particular one able to compute the grain size distribution that proved particularly useful (see section 4). The instrument has also the possibility to be equipped with various polarizers and optical filters in order to enhance the contrast between the objects under study. The instrument is located inside an ISO-7 clean room in Padova in order to reduce the risk of any contamination of the samples by dust present in the air

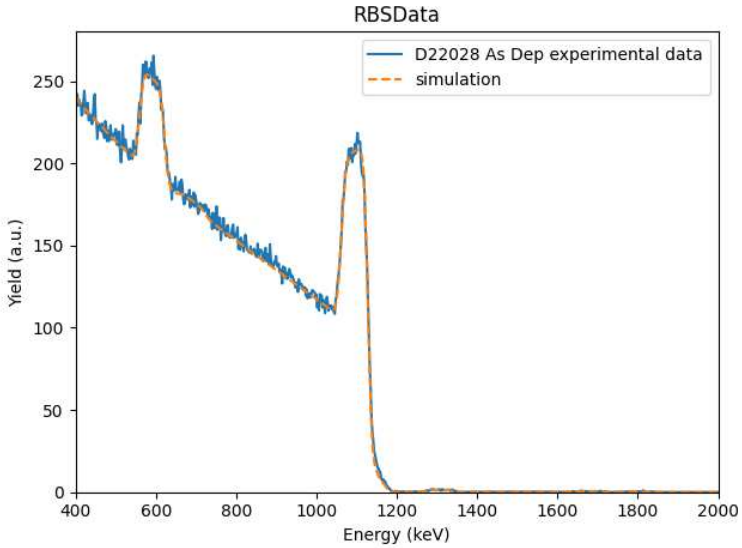

(a)

Figure 3.18: Example of an RBS measure

Figure 3.19: Keyence VHX-7000N digital microscope used.

Chapter 4

Controlled Crystallization of Ta2O5 Thin Films

As explored in chapter 2, while the current main design strategy to improve GW interferometers coatings consists in searching for different materials able to a reduce the level of the Coating Brownian Thermal Noise (CBTN), in this work we focus on the possible application of a meta-material composed by crystalline grains embedded into an amorphous matrix.
Since what we aim to study is the applicability of a general process rather than the specific characteristic of a single material, when firstly designing these experiment the choice to focus onto pure tantala coatings was made. Ta2O5 has a simpler chemical structure respect Ti:Ta2O5, is one of the most studied optical materials due to its high index of refraction, has excellent chemical stability, and its mechanical performances are not too far from the titanium doped version [15].
In this chapter, after a brief explanation of the theory behind the crystallization process in amorphous materials given in section 4.1, the results of the investigation of Ta2O5 after thermal treatment will be presented. Following that in section 4.3 the results of the experiments aimed at obtaining a certain crystalline fraction are reported and in section 4.3.1 a study of the grain size distribution achievable in our material is shown.

4.1 Theory of crystallization

The transition between amorphous and crystalline materials represents a fundamental change in the structural arrangement of atoms or molecules within a substance. Amorphous materials, characterized by a lack of long-range order, can be interpreted as a local energy minimum of the Gibbs free energy that a certain configuration state a solid can assume. This configuration is not the most stable one and tend naturally to transition into crystalline structures due to the much lower internal free energy of

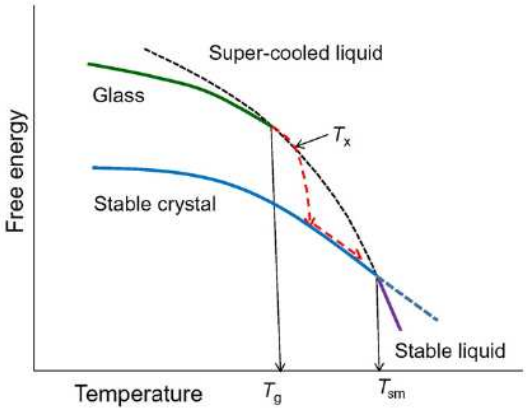

Figure 4.1: Scheme of the general relationship between the phase of a material and its free energy in function of the temperature

the latter. This transition from a metastable configuration to the stable energy minimum however, can require enormous times to the point where some materials are deemed stable in the amorphous phase. The material's inherent tendency to seek a more thermodynamically stable and ordered structure, needs often to be triggered by external factors that helps the various atoms inside the material's matrix to cross the energy barriers that keep them in place into their final configuration. Multiple processes are able to cause this transition but the most common one (and the one used in this work) is the *Thermal Annealing* process where a material is heated for a long period of time usually below the material melting point. By controlling the heating, the soaking and the cooling of the material one can relieve internal stresses, improve mechanical properties, and alter the microstructure of the material hence inducing the aforementioned transition from amorphous to crystalline.
The crystallization phase transition, although occurring in different possible ways and to some extent not fully understood, can be summarized in a few steps:

- Nucleation: the formation of small, ordered regions called nuclei within the amorphous material.
- Growth: the growth of the nuclei by incorporating nearby atoms or molecules, in a specific crystalline arrangement
- Propagation: the macro-process of multiple nucleated regions mending together
- Completion: the progressive end of the process due to the absence of material to be further converted.

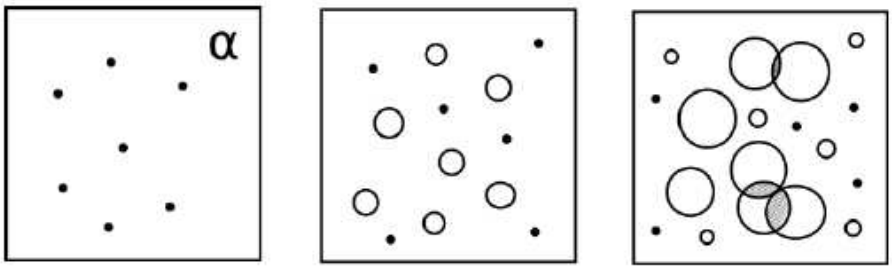

Figure 4.2: Progressive crystallization of a medium via nucleation and growth of the crystallized nuclei

. While each of these phases must occur subsequently, it's possible for different regions of the material to undergo them at different times.
A key difference that must be noted is whether the material transition from amorphous to crystalline occours in an homogeneous or an heterogeneous way. In the former case there exist only one bulk medium and the crystallization nuclei form spontaneously as an effect of the annealing process, while in the latter either alien inclusion inside the amorphous matrix or the presence of surfaces aid the nucleation. Only the case of homogeneous crystallization will be covered here.
The description of a material phase can be obtained by a combination of extensive and intensives quantities depending of the ensamble description one wishes to adopt. Using the extensive quantities S, V and N, respectively the entropy, the volume occupied, and the mole numbers of its components respectively, the internal energy U of a material can be written as a function of state of those variables.

$$U = U(S, V, N) \tag{4.1}$$

When dealing with phase transition however the important thermodynamic potential one must consider is the Gibbs free energy G:

$$dG = dU - d(ST) + d(PV) = -SdT + VdP + \mu dN \tag{4.2}$$

where the last equation follows from thermodynamic's first law. The intensive quantities T, P, μ, i.e. the temperature, the pressure and the chemical potential respectively, are introduced. Since the intensive variables are also functions of state of the extensive ones Gibbs free energy is also a state function. A system is in equilibrium when Gibbs free energy is absolutely minimized.
Lets now consider a volume of amorphous material where a small crystallization nucleus appears. A certain amount of atoms n will then change their phase collectively and a change in the Gibbs energy will manifest. While

the crystalline phase has the lowest free energy, the creations of interfaces between the phases induce an extra energy cost due to surface tension; the two phenomena compete in the change of free energy:

$$\Delta G(n) = \Delta G_v + \Delta G_s = g_v n + g_s n_s \tag{4.3}$$

with the subscription v and s indicating the volume of the cluster and its surface, g the Gibbs energy per atom and n the number of atoms. Assuming a spherical shape of the crystalline region with radius r and the mean interatomic distance to be a, the amount of atoms on the surface can be written as the ratio between the surface area of the nuclei and the average projected atom area πa^2:

$$n_s = \frac{4r^2}{a^2} \tag{4.4}$$

Equally the number of atoms in a volume can be written as the ratio between the total volume and the average volume occupied by an atom; assuming the atoms to be spheres with volume a we can write:

$$n = \left(\frac{4}{3}\pi r^3\right) / \left(\frac{4}{3}\pi a^3\right) = \frac{r^3}{a^3} \tag{4.5}$$

We can now rewrite equation 4.3 as

$$\Delta G = g_v n + g_s n_s = \left(g_v \frac{r^3}{a^3} + g_s \frac{4r^2}{a^2}\right) \tag{4.6}$$

Since the volume term g_v is negative and the surface one g_s is positive the variation in free energy initially is positive, has a maximum ΔG^* at $r_c = -4ag_s/g_v$ and then decrease monotonically (Figure 4.3). This means that crystalline nuclei smaller than r_c are energetically unfavorable and thus will tend to dissolve, while nuclei larger than r_c have a tendency to grow further to minimize their energy. The growth rate of these nuclei can be related to the difference between the rate of atoms joining the crystalline structure $\dot{n}_+$ and the rate of atoms leaving it $\dot{n}_-$ as:

$$v_g = \frac{dR(n)}{dt} = \frac{n^{-2/3}}{3} a(\dot{n}_+ - \dot{n}_-) \tag{4.7}$$

These rates are temperature dependant processes and can be expressed, following the approach of [61] as the product of two Arrhenius-like processes the first related to the formation of a defect either in the amorphous or the crystalline structure and the second related to the change in Gibbs energy in the new configuration:

$$\dot{n}_\pm = 3n^{2/3} K \; exp\left(\frac{-(E_f + E_m)}{K_b T}\right) \; exp\left(\mp \frac{\Delta G(n+1) - \Delta G(n)}{2K_b T}\right) \tag{4.8}$$

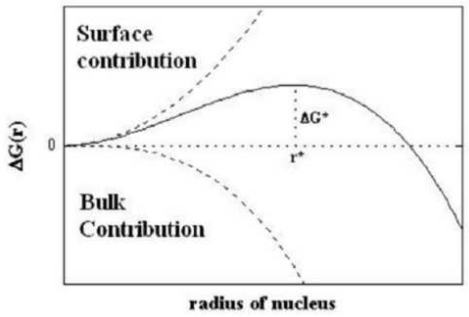

Figure 4.3: Example of Gibbs Free energy as a function of the crystalline cluster radius.

Where E_f represent the activation energy required to create a defect inside the structure and E_m the energy required for said defect to move inside the material. Plugging equation 4.8 into equation 4.7 we obtain the expression:

$$v_g = aKe^{-(E_f+E_m)/K_bT}\left(e^{-\frac{\Delta G(n+1)-\Delta G(n)}{2K_bT}} - e^{\frac{\Delta G(n+1)-\Delta G(n)}{2K_bT}}\right) \tag{4.9}$$

and, under the assumption that the variation in free energy is small when a single atom is added or removed to the cluster respect K_bT and under the assumption that we are considering only clusters with a dimension bigger than the critical size, we can rewrite this formula as:

$$v_g = \frac{V_0}{K_bT}e^{-\left(\frac{E_f+E_m}{K_bT}\right)} \tag{4.10}$$

In a similar fashion one can also express the rate of formation of new nuclei per unit volume inside of the material J_{ss}. Following the approach of [79] one finds:

$$J_{ss} = \frac{J_0}{\sqrt{K_bT}}e^{-\left(\frac{E_f+E_m+\Delta G^*}{K_bT}\right)} \tag{4.11}$$

When comparing the two last equations the general behavior is that the nucleation process starts at lower temperatures with respect to the growth process, peaks, and starts rapidly to decrease. The growth rate display a similar behaviour but shifted in temperature with the highest growth rate usually being near the material melting temperature. A scheme of this process is reported figure 4.4. Thus, by choosing the appropriate temperature and duration of a thermal treatment, it is possible to induce different grain concentrations and different size distributions. The temperature range close to the melting temperature where the growth rate is high and the nucleation is basically suppressed is called Ostwald–Miers range or metastable supercooling. In this region no new nuclei are allowed to form and only

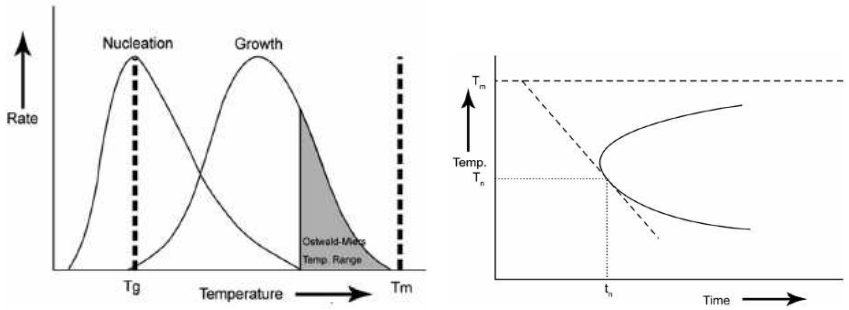

(a) (b)

Figure 4.4: a) General competitive behaviour between the nucleation process and the crystal growth b) TTT diagram showing the general relation between temperature, time, and transformation rate

those already present can grow. The combination of the nucleation rate and of the growth rate determines the rate of tranformation of the amorphous material into the crystallized one. Empirically it is found that the transformation rate behaves essentially as the product of the nucleation rate and the growth speed, peaking in between the two. Since different combination of temperature and time can lead to different amounts of crystallized material as well as potentially changing the microstructure and the phase of the crystalline material, traditionally the way employed to summarize these information is trough the use of *TTT diagrams* in which upon the Temperature-Time plane isoline depicting a certain level of Transformation are reported.

4.1.1 The Johnson-Mehl-Avrami-Kolmogorov Equation

Lets now consider an ideal case in which a certain volume V of amorphous material starts at a time t_0 an isothermic annealing treatment and evolves into a crystalline material. At a general time a portion of the material V_c will have transitioned into the crystalline phase and a certain number of crystalline clusters $N(t)$ will be present. The two quantities v_g and J_{ss}, once chosen a specific material, depend only on the temperature and can so be assumed as constant during an isothermal crystallization process. The variation of the number of nuclei formed per unit time t can be written as:

$$\dot{N}(t) = J_{ss}[V - V_c(t)] = J_{ss}V_f(t) \tag{4.12}$$

Where V_f is the volume of the amorphous fraction still to be transformed. Similarly if we consider a crystalline region nucleated at a time $t_0 < \tau < t$ its radius can be written as:

$$r(t, \tau) = v_g(t - \tau) \tag{4.13}$$

The crystalline regions forming inside the material can grow in different shapes but can reasonably approximated as spheres disregarding the specific details. The only thing we must not disregard is the dimensionality of the object we are dealing with: if our grains are for example columns of material with a constant section forming inside the amorphous matrix the ratio between the crystallized volume of a cluster and the effective radius will be proportional to r while if our grains are perfect spheres their ratio will be proportional to r^3. The exponent of r can be identified as the characteristic dimensionality of the growth process. For an *n-dimensional sphere* the general formula for its own volume is:

$$V_{n-sphere} = \frac{\pi^{n/2}}{\Gamma(\frac{n}{2}+1)} r^n = A(n) r^n \tag{4.14}$$

with Γ being the Euler's gamma function.
We can then write the variation in the crystallized volume at the time t due to nuclei originated at the time τ as

$$\mathrm{d}V_{c,\tau} = V J_{ss} A(n) v_g^n (t-\tau)^n \mathrm{d}\tau \tag{4.15}$$

However the last expression does not take into account that, at a given time t, a part of the volume is already crystallized and therefore not available. The real variation rate of the crystallized volume is therefore obtained by rescaling equation 4.15 by the fraction of available amorphous volume:

$$\mathrm{d}V_c = \mathrm{d}V_{c,\tau} \left(1 - \frac{V_c}{V}\right) \tag{4.16}$$

This is now a differential equation easy to solve. Defining the crystalline fraction as:

$$\chi(t) = \frac{V_c(t)}{V} \tag{4.17}$$

we can solve it as:

$$\frac{\mathrm{d}V_c}{V} = \frac{\mathrm{d}V_{c,\tau}}{V}\left(1 - \frac{V_c}{V}\right) \implies \frac{\mathrm{d}\chi}{1-\chi} = \frac{\mathrm{d}V_{c,\tau}}{V} \implies ln(1-\chi) = -\frac{V_{c,\tau}}{V} \tag{4.18}$$

We can now write by integrating across all the times between 0 and t and using equation 4.15:

$$\begin{aligned} ln\left[1-\chi(t)\right] &= -\int_0^t \frac{\dot{N}(\tau)}{V} r(t,\tau)\mathrm{d}\tau \\ &= -\int_0^t A(n) J_{ss} v_g^n (t-\tau)^n \mathrm{d}\tau \\ &= \frac{A(n) J_{ss} v_g^n}{n+1}(t-\tau)^{n+1}\Big|_0^t \qquad = -\left(\frac{t}{\tau_c}\right)^{n+1} \end{aligned} \tag{4.19}$$

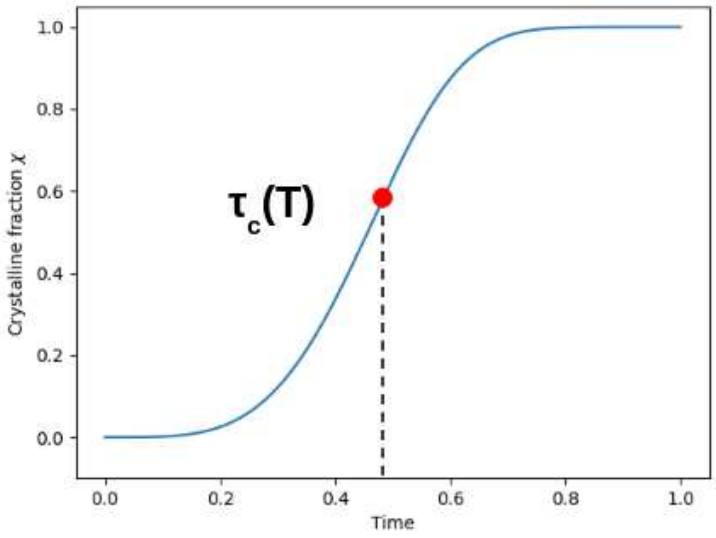

Figure 4.5: Example of Avrami transformations

Where we defined the *crystallization characteristic time* as

$$\tau_c = \left(\frac{n+1}{A(n) j_{ss} v_g^n} \right)^{\frac{1}{n+1}} \tag{4.20}$$

Expressing now the crystallized fraction and defining the characteristic exponent $\alpha = n + 1$ we obtained the so called Avrami or JMAK equation:

$$\chi(t) = 1 - exp\left[- \left(\frac{t}{\tau_c} \right)^{\alpha} \right] \tag{4.21}$$

Since the crystallization characteristic time is a function of just the nucleation rate and the growth speed we can calculate its dependence to temperature variation plugging equation 4.10 and 4.11 in equation 4.20 as:

$$\begin{aligned} \tau_c &= \left[\frac{\alpha \Gamma \left(\frac{\alpha+1}{2} \right) (K_b T)^{\frac{2\alpha-1}{2}}}{\pi^{\frac{\alpha-1}{2}} J_0 V_0^{\alpha-1}} \right]^{1/\alpha} e^{-\left(\frac{\alpha E_f + \alpha E_m + \Delta G^*}{\alpha K_b T} \right)} \\ &= \tau_0 (K_b T)^{\frac{2\alpha-1}{2\alpha}} e^{-\left(\frac{E_c}{K_b T} \right)} \end{aligned} \tag{4.22}$$

4.1.2 Multi-step Annealing

The JMAK equation can be readily extended to cover the case of a multi-stage annealing, i.e. a thermal treatment composed of different stages and duration. This is useful to model what happens to samples that underwent a first annealing as a standard part of their production process and are

subsequently treated a second time. In the following we will assume that the heating and cooling ramps occur fast enough so that their effect can be neglected with respect to the actual soaking time..
We can retrace the steps followed in the derivation of Avrami's law to derive the kinetic equations of a two steps annealing process. At time t_0 the sample starts an annealing with temperature T_1 until a time t_1 where it changes to a temperature T_2. The nucleation time and the growth rate instead of being constant like in the previous case become now time dependant:

$$\dot{N}(t) = \begin{cases} J_{ss1} & t < t_1 \\ J_{ss2} & t \geq t_1 \end{cases} \tag{4.23}$$

and

$$v_g(t) = \begin{cases} v_{g1} & t < t_1 \\ v_{g2} & t \geq t_1 \end{cases} \tag{4.24}$$

The expression of the radius of a crystalline cluster nucleated at time τ hence becomes:

$$R(t,\tau) = \begin{cases} v_{g_2}(t-\tau) & t_1 < \tau < t \\ v_{g_2}(t-t_1) + v_{g_1}(t_1-\tau) & \tau \leq t_1 < t \\ v_{g_1}(t-\tau) & \tau < t \leq t_1 \end{cases} \tag{4.25}$$

As before we now solve the differential equation for the crystallized fraction and we integrate it in time to obtain:

$$ln\left[1-\chi(t)\right] = \int_0^t \frac{\dot{N}(\tau)}{V} R(t,\tau)\mathrm{d}\tau$$

$$= \begin{cases} \displaystyle\int_0^t A(n_1) j_{ss_1} v_{g_1}^{n_1} (t-\tau)^{n_1} \mathrm{d}\tau & t < t_0 \\ \left(\displaystyle\int_{t_0}^t A(n_2) j_{ss_2} v_{g_2}^{n_2} (t-\tau)^{n_2} \mathrm{d}\tau \right. & \\ \left. + \displaystyle\int_0^{t_0} A(n_1) j_{ss_1} \left[v_{g_2}(t-t_0) + v_{g_1}(t_0-\tau) \right]^{n_1} \mathrm{d}\tau \right) & t > t_0 \end{cases}$$

$$= \begin{cases} -\left(\dfrac{t}{\tau_{c_1}}\right)^{\alpha_1} & t < t_0 \\ \left(-\left(\dfrac{t-t_0}{\tau_{c_2}}\right)^{\alpha_2} \right. & \\ \left. + \left(\dfrac{t-t_0}{\tau_{c_1}}\right)^{\alpha_1} \left(\dfrac{v_{g_2}}{v_{g_1}}\right)^{\alpha_1} \left[1 - \left(1 + \dfrac{v_{g_1}}{v_{g_2}} \dfrac{t_0}{t-t_0} \right)^{\alpha_1} \right] \right) & t > t_0 \end{cases}$$

where. to maintain the formulation in the most general form, we accounted

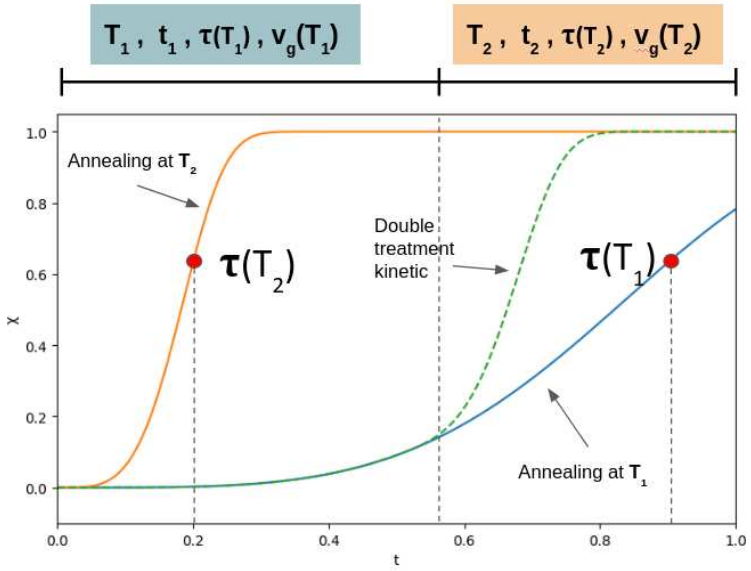

Figure 4.6: An exemplary two steps annealing process and its derived crystallization kinetics

for the possibility of the growth process happening with a different dimensionality at the two treatment temperatures by distinguishing between the critical exponent of the first treatment α_1 and the one of the second treatment α_2.
It is also possible to derive a general expression for a completely arbitrary (non isothermal) treatment where the temperature changes continuously with time. This solution can be useful e.g. to model the effect of slow ramps on the crystallization.

$$ln[1-\chi(t)] = -A(n)\int_0^t J_{ss}[T(\tau)]\left\{\int_\tau^t v_g[T(\tau)]\mathrm{d}\tau\right\}^{n(\tau)}\mathrm{d}\tau \qquad (4.26)$$

4.1.3 Assessing the Crystalline fraction

There exist multiple techniques able to probe the crystalline state of a sample but each one comes with its own limitation and only by combining multiple of them it's possible to get a full picture [62]. A not exhaustive summary of the techniques able to spot the crystallization happening in a material together with their main advantages and disadvantages is here reported.

- **Transmission Electron Microscopy:**
  - Great precision over grain size distribution and percentage of crystallized material
  - Measurements in situ not possible

  - Hard to prepare samples for analysis and require to destroy samples

- **X-Ray Diffraction:**
  - Fast and non destructive way to investigate samples
  - Provides information on both grain size and crystal fraction
  - Possibly of measurement in-situ
  - Indirect measure, prone to multiple errors

- **Differential Scanning Calorimetry:**
  - Best way to monitor the kinetic of the process
  - provides no information regarding crystal fraction or grain size distribution
  - Require preparation of ad-hoc sample whose preparation is not trivial

- **Optical microscopy:**
  - Fast and non invasive measurement for grain size distribution
  - Measurements in situ not possible
  - can only measure "big" grain sizes

4.2 Optical and morphological characterization

In order to investigate the properties induced by crystalline inclusion in an amorphous matrix the first step is to obtain a reliable way of producing samples with a tailored degree of crystallization. In this thesis we focus on Ta_2O_5 coatings, as this is a standard material used for the high index layers of optical Bragg gratings, SiO_2 being the low - index one. As discussed in chapter 2 it is known that Ta_2O_5 layers are the main responsible for the coating browninan noise. Furthermore this material is the one that, for a given annealing duration, shows the tendency to crystallize first and so it is the one for which our investigation is more meaningful. In the field of GW interferometry, Ta_2O_5 is generally doped with TiO_2, as this mixture is shown to display better thermal noise properties and to withstand annealing at higher temperature without crystallizing. The effect of the TiO_2 doping on the crystallization process will be discussed in paragraph 4.3.4.
To study the effect of the annealing process on Ta_2O_5 thin films, we began by observing in closer details the morphology of samples annealed to the point where some crystallization has occurred in the sample. To this purpose we considered a set of ion beam sputtered samples prepared according to the standard LMA protocol, i.e. pre-annealed at 500°C in order to favor

Sample	Step 1	Step 2	Step 3	Step 4	Step 5	crystalline fraction
K0	-	-	-	-	-	0
K1	6h, 630°C	-	-	-	-	$(0.05 \pm 0.03)\%$
K2	6h, 630°C	3h, 630°C	-	-	-	$(0.84 \pm 0.15)\%$
K3	6h, 630°C	3h, 630°C	3h, 630°C	-	-	$(4.7 \pm 0.6)\%$
K4	6h, 630°C	3h, 630°C	3h, 630°C	3h, 630°C	-	$(10.3 \pm 0.6)\%$
K5	6h, 630°C	3h, 630°C	3h, 630°C	3h, 630°C	3h, 630°C	$(28.3 \pm 3.0)\%$

Table 4.1: Soaking temperature and time (hours) of successive annealing steps applied to samples from series K, together with the crystalline fraction measured by optical microscopy. Heating and cooling ramps of 100°C/hour were used. All sample underwent an initial Annealing of 10 hours at $500°C$. The same treatments were also applied to samples from series Z.

the relaxation of the as-deposited amorphous films. After a preliminary investigation performed by XRD (see the paragraph 4.3.2 for details) we established that an additional treatment at around 630°C for several hours is able to partially crystallize the samples. Thus, a set of samples (series K) were prepared according to the treatments reported in table 4.1.

Visual inspection of sample surfaces was carried out using the digital microscope. Samples were illuminated with coaxial lighting and a pair of polarizing filters was placed in the optical path. Optical microscope images for K samples are shown in Figures 4.7. All the images demonstrate a uniform background with some randomly distributed grains of different colors. The average size and areal density of the grains increase with increasing annealing time. The detected color and intensity of light reflected from the grains is dependent on the relative orientation of the polarization filters, while the uniform background appears unchanged under the same conditions. From these observations we infer that the uniform background represents the areas where the coating is still in its amorphous phase, while grains represent optically anisotropic regions where the Ta_2O_5 coating is locally crystallized.

To confirm that the observed grains are indeed crystalline aggregates, we characterized the vibrational properties of the samples with a Horiba XploRA Plus spectrometer at exciting laser wavelengths of 532 nm and 785 nm. To this scope we used samples analogous to the ones from the series K, but deposited on a silica substrate (series Z), as the background Raman signal from the SiO_2 substrate was much smaller than that of the Si substrate of samples K from series. We focused on the differences between homogeneous-looking areas and areas where one or more grains were visible, such as regions R1 and R2 in Fig. 4.10(b), respectively.

The resulting Raman spectra are shown in Figure 4.8(a). The signal from region R1 shows a Ta_2O_5-related feature at $673\,cm^{-1}$ and is otherwise dominated by signal from the SiO_2 substrate. Conversely, new features are

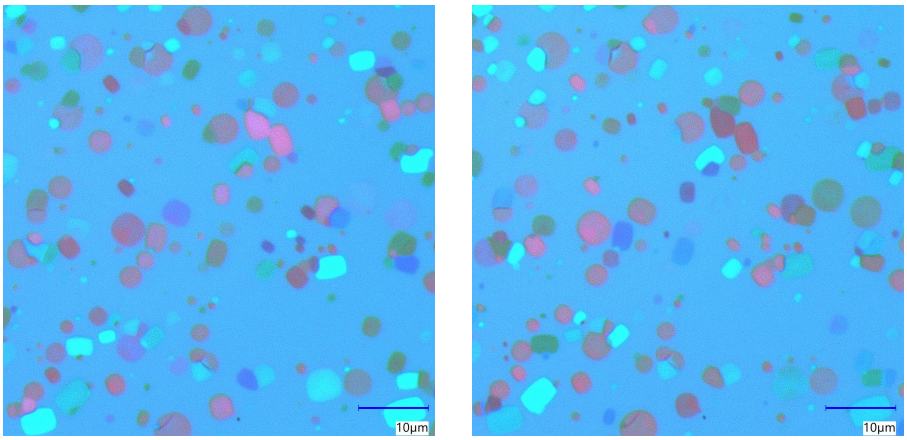

Figure 4.7: 2500x magnification optical microscopy image of the same area on sample K5 with two different polarizer positions. Background is unchanged, grains change color and/or contrast.

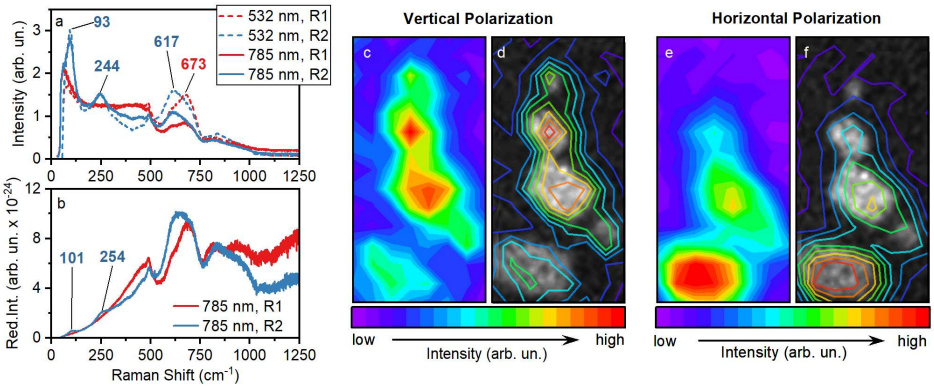

Figure 4.8: (a) Raman spectra of R1-like and R2-like regions acquired at 532 and 785 nm. (b) Corresponding reduced Raman spectra at 785 nm. (c)-(f) R2-like region with five individual grains, as observed via optical microscopy and Raman maps at 532 nm: panels (c) and (e) show relative intensity maps of the 244 cm^{-1} feature with vertical and horizontal polarizations, respectively; panels (d) and (f) show the intensity maps of panels (c) and (e) overlapped with an optical microscopy image of the corresponding region.

visible in the R2 spectrum, with peaks arising at 93, 245 and 617 cm^{-1}. The peak at 673 cm^{-1} is not visible in R2 case, at least not as a resolved individual feature. Signal from SiO_2 is present also in this case, although it is much less relevant than in R1 case. Comparison between the 532 nm and 785 nm signal shows the Ta_2O_5 spectral features are not changed in shape or position, with the only major difference given by a change of background signal between ∼500 and 1000 cm^{-1}. This latter effect can be due either

to an actual quenching of fluorescence signal from the SiO_2 substrate or to a variety of wavelength-dependent instrumental effects such as etalon interference due to the thin-film geometry, a change of the confocal optical probe size along the surface normal , etc. The consistency of the Ta_2O_5 spectra allows us to study it with either laser wavelength. Notably, the spectra gathered from R1 and R2 regions are consistent with the reported spectra from amorphous and crystalline Ta_2O_5, respectively [25, 39]. This confirms that the grains with different refractive index contrast are indeed crystalline grains of Ta_2O_5 embedded in an amorphous matrix.

In order to eliminate the influence of temperature and laser wavelength and thus gain a clearer picture of the vibrational density of states and Raman coupling, we represented the spectra into their reduced form as follows [37]:

$$\mathcal{I}_R(\omega) = \omega(\omega_L - \omega)^{-4} \left[n(\omega) + 1\right]^{-1} \mathcal{I}_0(\omega)\,, \tag{4.27}$$

where $\mathcal{I}_0(\omega)$ is the experimentally determined intensity, ω_L is the incident laser frequency, and $n(\omega)$ is the following temperature-related boson factor:

$$n(\omega) = \left[\exp(\hbar\omega/k_B T) - 1\right]^{-1}. \tag{4.28}$$

$\mathcal{I}_R(\omega)$ can be represented as $\mathcal{I}_R(\omega) = C(\omega)\rho(\omega)$, where $C(\omega)$ is the coupling function and $\rho(\omega)$ is the vibrational density of states (VDOS). The reduced spectrum is thus proportional to the VDOS, providing a spectrum not affected by temperature and incident laser frequency. The reduced spectra for 785 nm are shown in Figure 4.8(b). The previously observed shift of the peak at around $600\,\mathrm{cm}^{-1}$ between R1 to R2 cases is confirmed, as is the presence of spectral features at low wavenumbers, though their spectral position is changed. Non-linear peak fitting shows that the new positions for the peaks, which we observed at $93\,\mathrm{cm}^{-1}$ and $244\,\mathrm{cm}^{-1}$ in Figure 4.8(a), are $101\,\mathrm{cm}^{-1}$ and $254\,\mathrm{cm}^{-1}$, respectively. These latter two values are therefore corresponding to the true position of these features in the VDOS and coupling. Furthermore, we studied the dependence of the Raman response of the crystalline grains with respect to the polarization direction of the the incident laser beam. We identified a region with several grains, as shown in Figures 4.8(d) and (f), which was mapped by performing a Raman spectral mapping on a grid-like pattern. By examining the relative intensity in each spectra of grain-related peaks identified in Fig. 4.8(a), we obtained the spatial intensity distribution for each spectral feature. We repeated this process for two incident laser polarizations, horizontal and vertical, which are rotated 90° with respect to one other. We acquired the intensity maps at 532 nm rather than at 785 nm because of the higher signal-to-noise ratio.

Figures 4.8(c) and (e) show the relative intensity maps of the peak at $244\,\mathrm{cm}^{-1}$ for vertical and horizontal polarizations, respectively. If the maps are superimposed on the optical microscope image [Figures 4.8(d) and (f)], we can see that the intensity map reproduces the position of the grains.

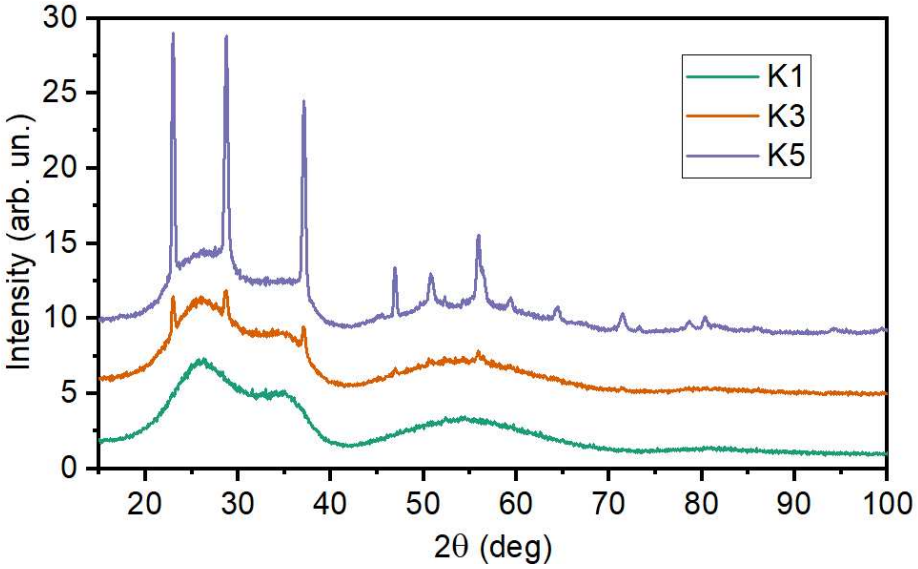

Figure 4.9: GIXRD spectra of samples K1, K3 and K5.

However, the signal from different grains clearly depends on the input polarization used.

The different response to polarized light allows us to conclude that each grain is nearly single-crystalline, with different crystallographic orientations with respect to each other in agreement with the observations in polarized-light microscopy reported in Fig. 4.7.

GIXRD measurements were then performed to study the average crystallization process on the whole sample. The diffraction spectrum for all samples was measured by keeping the primary beam fixed at an incidence angle of 1° with respect to the sample surface and moving the detector goniometer (2θ-scan) with 2θ ranging from 15° to 100° (see Fig. 4.9).

Diffraction spectra for samples K1, K3 and K5 are reported in Fig. 4.9. The spectrum for K1 does not show any sharp features, which is consistent with the spectrum of amorphous Ta_2O_5. Meanwhile, well-defined diffraction peaks are visible in the spectrum for K5. The same features are visible in the K3 spectrum, which represents an intermediate case between K1 and K5, where the peaks appear above the background but are still low in intensity. The obtained diffraction spectra are in good agreement with the ones reported by other authors for crystallized Ta_2O_5 [40, 41]. Thus, the intensity of the diffraction peaks is directly related to the crystalline fraction in samples K1, K3 and K5, providing further confirmation that the structures observed in microscopy and Raman measurements are indeed a collection of crystalline grains dispersed in the amorphous coating matrix.

To perform a more quantitative analysis, a Ta_2O_5 sample identical to the ones of the series K has been treated for 100 hours at 630°C to obtain

Sample	χ XRD (%)	χ Optical microscope(%)
Z0	0	0
Z1	2.3 ± 0.3	3.9 ± 0.6
Z2	9.4 ± 0.4	13 ± 2
Z3	34 ± 1	30 ± 7
Z4	76 ± 1	70 ± 10
Z5	100	100

Table 4.2: Crystalline fraction from optical and XRD measurements.

a fully crystallized state. Assuming that the peak intensity at $2\theta = 28°$ is proportional to the crystallized volume, we estimated the crystalline fraction from the GIXRD spectra by normalizing the various measurements with respect to the peak intensity of the fully crystallized sample. Those results are compared to the analysis of the optical microscope images. We performed a particle count analysis on pictures taken at several spots on each sample. This gave us a statistically significant estimate for the crystalline fraction of the coating volume, reported in Table 4.1: the crystalline fraction is below 1% for samples annealed less than 9h (K1 and K2), while it grows dramatically in samples with longer annealing times. The two estimates are in very good agreement, as it can be seen from values reported in Table 4.2.

In conclusion, we demonstrated that by by performing a suitable annealing treatment at sufficiently high temperatures and/or for sufficiently long times it is possible to induce the formation of a collection of crystalline grains within the volume of the coating. The total amount of crystallized volume can be estimated either by GIXRD, either by analyzing the surface covered by the crystalline grains under optical microscope.

4.3 Crystallization Kinetics

In this section we will study how the crystallization process in Ta_2O_5 coatings evolve with time.

4.3.1 Grain size and grain density

By using a dedicated image analysis software, we were able to study the samples of the K series (see Tab. 4.1) in order to characterize the dependency of the observed grain dispersion as a function of the treatment duration. In Fig. 4.10 (a - e) are reported a set of images obtained for the different treatments.

This analysis also allowed us to quantitatively estimate the size distribution and areal density of grains ρ_N for each sample. We calculated

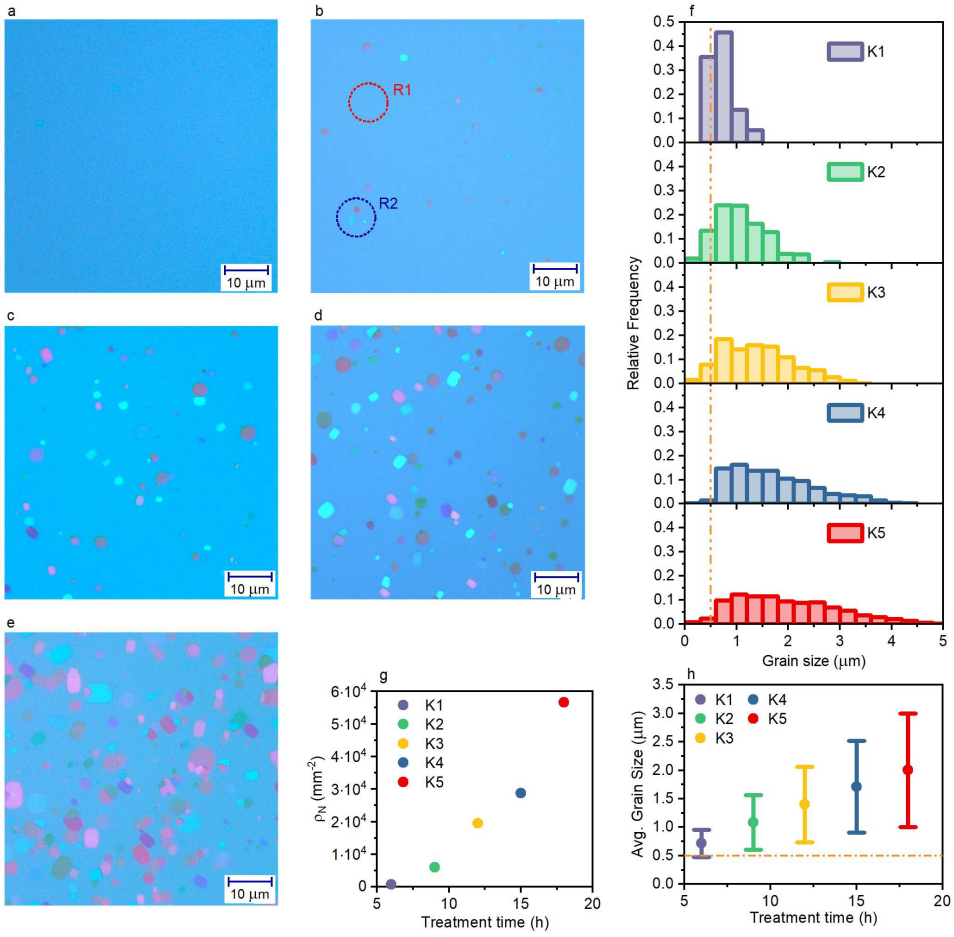

Figure 4.10: Optical microscope images taken with polarizing filters of samples (a) K1, (b) K2, (c) K3, (d) K4 and (e) K5. (f) Relative frequency distributions of grain size detected by optical microscopy. Crystal grain areal density ρ_N (g) and average grain size (h) against total annealing time at 630°C. The circled areas R1 and R2 in (b) indicate two regions without and with visible grains, respectively. Orange lines in (f) and (h) show the comparison with coating film thickness.

the grain size as the square root of measured grain areas, in order to remove differences due to grain shape. The size distribution of grains for each sample, normalized to 1 to provide the relative frequency, is reported in Fig. 4.10(f), while the average grain size and the crystal grain areal density as a function of the treatment duration are reported in Fig. 4.10(g) and (h), respectively. The distribution in Fig. 4.10(f) resembles grain size distributions of crystallization models reported in previous studies [38]. The average grain size increases linearly with the treatment time, in agreement with the basic hypothesis of the JMAK model. We note that, already for

the least crystallized sample K1, the average crystal size is larger than the coating film thickness, which is about 500 nm [orange dotted line in Figures 4.10(f) and (h)]. This indicates that, in these annealing conditions, the grain growth becomes quickly limited by the coating thickness and the growth velocity we are considering here has probably to be understood as a 2D growth velocity. By fitting the data in fig. 4.10(h) we obtain an estimation of $v_g = (0.112 \pm 0.004)\,\mu m/\text{hrs}$. On the other hand, the areal density displays a strange behaviour which cannot be explained by assuming a uniform nucleation rate, as in this case this would give a linear increase of the grain density with time, at least at short times. Even more strange is the fact that, as time goes by, the available amorphous volume for the nucleation of new grains is more and more limited, so one would rather expect the grain density to display a *sub-linear* behavior with time. This discrepancy suggests that in our samples the JMAK model can be applied only at very early stages of the crystallization process.

4.3.2 Volume fraction

The crystallization kinetics of tantala was studied in a wide range of temperatures with a combination of *in-situ* GIXRD experiments and *ex-situ* ones across multiple samples. As observed in the previous paragraph, the intensity of the XRD spectrum of crystalline Tantala can be taken as proportional to the volume fraction of the crystalline phase. Therefore by measuring in the same conditions different samples, we can estimate the relative content of crystallized volume fraction. Furthermore, taking advantage of the thermal stage fitted to the sample holder of our diffractometer, we can perform in-situ measurement and directly observe the growth of the crystalline fraction as a function of time.
We started the study by investigating a set of samples produced at LMA (deposition run C19088) of $\sim 500nm$ of Ta_2O_5 deposited on fused silica wafers with a thickness of 6 mm later reduced to a few millimeters by cutting it with a diamond saw. A first sample was measured via GIXRD *in-situ* to asses the temperature where the characteristic time of the crystallization transition is comparable with the available measurement time (between a few hours and a few days). To this purpose, the sample was mounted in the XRD heating stage and was soaked at increasing temperatures from room temperature to 800°C with steps of 10°C; at each temperature the sample would spend a total time of 2.5 hours and after a diffraction spectrum has been taken ranging from $2\theta = 20^\circ$ to $2\theta = 80^\circ$. The time to acquire the spectrum is around 2.5 hours, so this experiment can be regarded as a multi-step annealing at increasing temperature. An example of some of the acquired spectra can be seen in figure 4.11; as it can be seen the first stages of the crystallization starts to be visible around 680°C.

Once found the desired temperature range, we perfomed a set of isother-

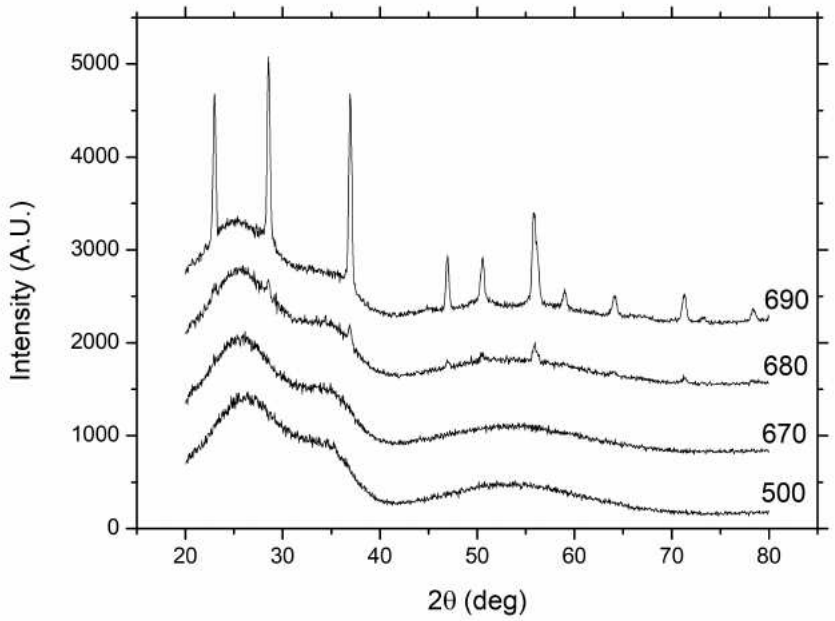

Figure 4.11: Diffractograms acquired on a single Ta_2O_5 sample during an thermal treatment covering several soaking temperatures

mal in-situ experiments. Using the heating stage of the diffractometer, the sample is brought quickly and maintained at the target temperature, while a set of spectra are measured. In order to obtain a faithful measurement of the spectra evolution, the temperature had been chosen so that the crystallization occurs with a slow enough characteristic time. For the same reason, instead of measuring a full diffractogram, we measured just the most intense peak in the range between 22.4 to 23.4 degrees. Such a measurement requires only few minutes. In figure 4.12 are reported the evolution with time of the diffraction spectrum. The same experiment has then been repeated at several different temperatures.

In order to expand the temperature range of our investigation, we studied also some samples prepared by ex-situ annealing at high temperature (around 700°C). At such temperatures, the transformation of the sample is too fast to be followed *in-situ* by the GIXRD measurement so we resolved to prepare several samples via RTA and observe only their final crystallization state via GIXRD in the same conditions adopted to measure the in-situ samples, so that the intensity of diffraction spectrum can be used to size the amount of crystalline fraction. Different combinations of temperature and treatment times were used to obtain samples with different degree of crystallization and the samples were classified either as amorhpous, partially crystallized, or crystalline. In figure 4.13 the temperatures and times

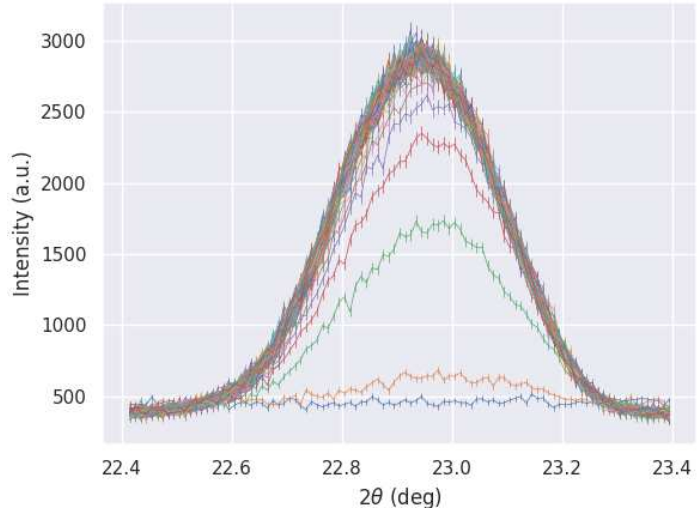

Figure 4.12: Diffraction peaks measured at different times in-situ. The blue line are the data acquired at the start of the process. The system then evolves increasing in intensity (Orange line, Green line, Red line...) and then saturates.

of treatment of the samples as well as their classification is depicted. Samples used for this phase were taken from a single deposition run (S19177) of ~ 500 nm of Ta_2O_5 on silicon wafers.

In-situ treated samples treatment temperatures have been corrected taking into account the fact that in the diffractometer thermal stage the heating is performed from the bottom of the sample and so a thermal gradient is present. Since the samples used for this study were prepared by cutting thicker silica wafers, the final temperature on the surface of the wafer , i.e. where the coating is present, is dependent on the sample thickness d. To estimate the correct temperature to attribute to each of our treatments we equated the heat flux across the substrate:

$$J_{in}(T) = -C\frac{T - T_0}{d} \tag{4.29}$$

with the heat flux irradiated by the film:

$$J_{out}(T) = \epsilon\sigma(T^4 - T_{env}^4) \tag{4.30}$$

where T is the real temperature of the film, T_0 the nominal treatment temperature corresponding to the temperature on the bottom of the wafer, T_{env} the environment temperature, C is the silica thermal conductivity $C = 1.3$ W/mK, ϵ the tantala emissivity $\epsilon = 0.6$, and σ is the Stefan-Boltzmann

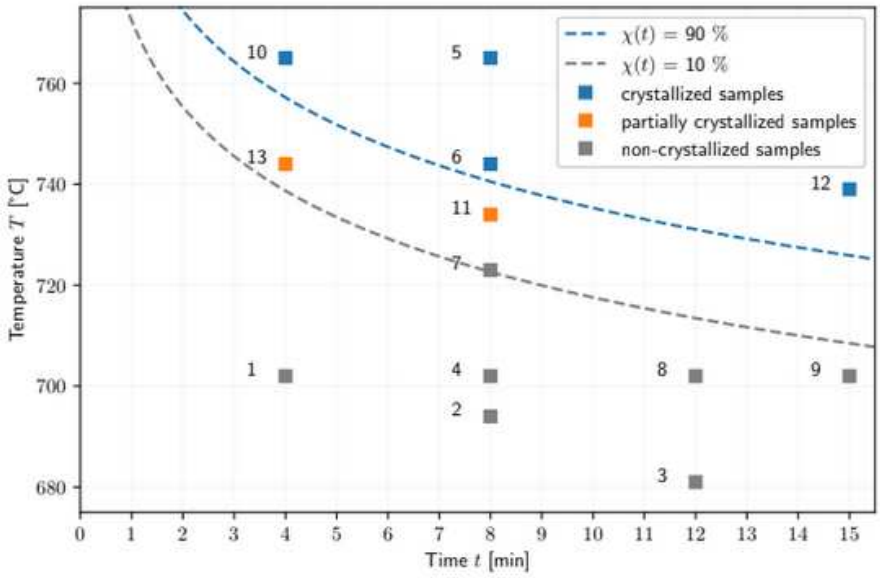

Figure 4.13: Annealing ccombinations explored via RTA. The sample produced have been characterized as either amorphous ($\chi < 10\%$), partially crystallized ($\chi > 10\% \wedge \chi < 90\%$), or fully crystallized ($\chi > 90\%$)

constant. We obtained a new estimate of the treatment temperatures at 637°C, 644°C, 651°C, 659°C, and 680°C with an estimated error of ±10°C each.

The set of diffraction peaks collected for each sample has been interpolated using a pseudo-Voight model with only the peak area, the peak FWHM, and the peak position as free parameters. In figure 4.14 it is reported the percentage of crystallization obtained by plotting the intensity of the diffraction peak at 2theta = 23° as a function of time and normalizing the asimptotic value to 100%. This corresponds to the assumption that when the peak intensity does not evolve anymore with time the sample can be considered fully crystallized. This assumption has been confirmed qualitatively with the help of the optical microscope which showed, for long-treated sample, that the whole surface is completely covered by crystal grains. Even though we cannot exclude that a fraction of material is still in the amorphous state (for instance, at the grain boundaries) we assume that this fraction is negligible on the whole coating volume.

The former data have then be fitted through the JMAK model leaving the critical exponent α and the crystallization time τ_c as free parameters. To this scope, eq. 4.21 can be rewritten as:

$$ln(-ln(1-\chi)) = Aln(t) + B \tag{4.31}$$

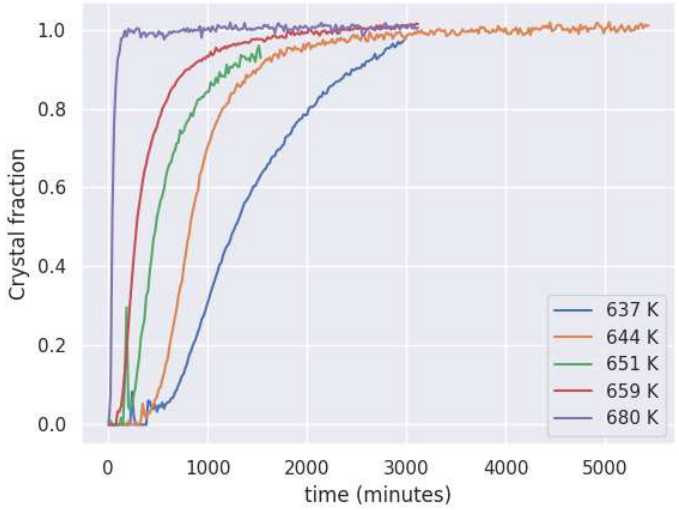

Figure 4.14: Crystalline fraction versus treatment time for five samples treated at different soaking temperatures. The crystal fraction has been estimated by acquiring the intensity of a single diffraction peak and by normalizing it to its own asimptotic value.

where $A = \alpha$ and $B = -\alpha ln(\tau_c)$. By plotting the data in this anamorphosis (see figure 4.16) we can see that all the plots are characterized by two regimes. The first regime can be interpreted as the unconstrained growth of the grains following their nucleation. By fitting those data to eq. 4.31 we obtain the results reported in table 4.3. As it can be seen, all the exponents are close to 4, as expected for the three-dimensional growth of crystalline grains (see eq. 1.19 with n = 3). At longer times, the Avrami plot shows a deviation from this initial behaviour, for which the slope decreases. This is to be attributed to the fact that when the average grain size becomes comparable to the sample thickness, the growth proceed in a 2D fashion.

Samples produced via RTA did not need any correction to obtain the treatment temperature since the system heating in this case is much more uniform. Since those samples could be characterized only ex-situ, the estimation of the crystallized fraction was only approximate. Thus, after investigation via GIXRD the RTA samples were classified as either non-crystallized, partially crystallized, or crystallized. It was then possible to obtain an estimate of the crystallization times at these higher temperatures, albeit with a much higher relative error taking into account that the crystallization time τ_c, according to eq 4.21 corresponds to the time where the crystallized fraction is a 69% of the total.

A parametrization of the dependence of the crystallization times respect

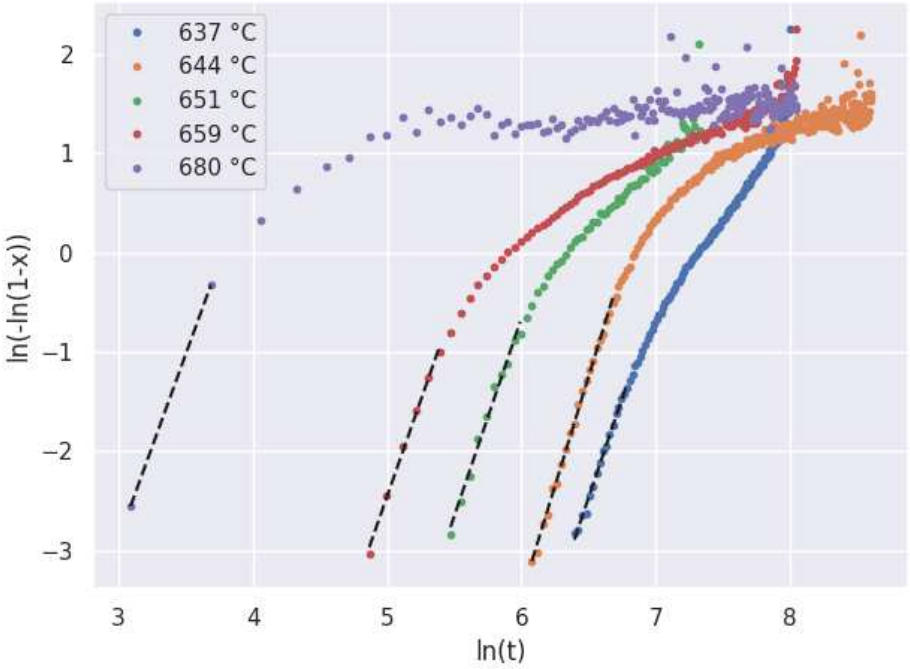

Figure 4.15

Figure 4.16: Data obtained through the analysis of the crystallization kinetics of Ta_2O_5Crystalline fraction $\chi(t)$ versus time. The data have been transformed in order to make the Avrami process appear linear through the transformation 4.31.

Temperature (°C)	τ_c (min)	α
637	1200 ± 200	4 ± 1
644	900 ± 120	4.4 ± 0.1
651	450 ± 50	4.1 ± 0.2
659	300 ± 200	3.9 ± 0.2
680	50 ± 10	3.7 ± 0.5

Table 4.3: Parameters obtained from the analysis of Ta_2O_5 isothermal crystallization kinetics

to the treatment temperature valid in a wide range of temperatures was then produced by combining the *in-situ* data with the RTA ones. To this degree equation 4.20 was linearized in the form:

$$ln\left[\tau_c^4 (K_b T)^{-7/2}\right] = a - \left(\frac{-Q}{K_b T}\right) \tag{4.32}$$

In figure 4.16 the data from the in-situ and ex-situ analysis have been plotted together according to eq. 4.32. As it can be seen, the data nicely confirm the expected dependence. By performing a linear regression on the data we obtain $a = 0 \pm 10$ and $Q = (2.4 \pm 0.1) \cdot 10^{-18}$ J.

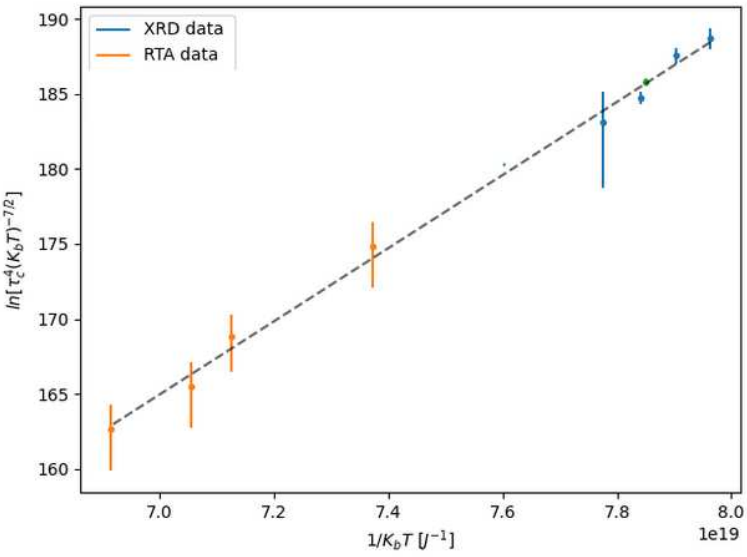

(a)

Figure 4.17: Dependence of the crystallization time from the treatment temperature. The data have been linearized through equation 4.32. The dashed line is the least square regression model.

4.3.3 Multi-temperature crystallization

We then studied how multiple stage of annealing affect the kinetics of our samples. In subsection 4.1.2 we showed how the parameters of the isothermal crystallization are able to describe even the non-isothermal one. We tested the accuracy of our model by treating a sample *in-situ* 11 hours at 650°C and at subsequently increasing the temperature to 680°C for 4 more hours. Using the same analysis procedure from the isothermal experiment we obtained the data regarding the crystalline fraction versus time. The data have then been fitted through the use of equation 4.1.2 obtaining an estimate of the isothermal crystallization time of the two temperatures used: $\tau_{650} = (580 \pm 30)$ min and $\tau_{680} = (190 \pm 40)$ min. Figure 4.18 shows the data of this experiment as well as the least square regression of eq 4.1.2. In figure 4.19 a comparison of the estimated crystallization times in a multi-step treatment respect the prediction obtained through the data of isothermal treatment is shown; notably the crystallization times estimated through the double kinetics experiment have been found to be in agreement with the crystallization times estimated through the isothermal data.

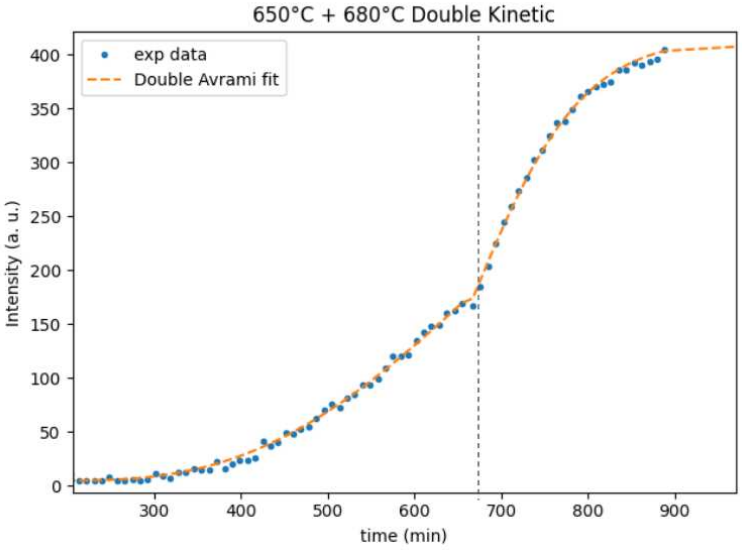

(a)

Figure 4.18: Experimental data and fit for a double treatment crystallization kinetics experiment.

The current standard post deposition treatment GW coatings undergo consist of a 10 hours 500°C annealing to relax their structure. We wanted to explore whether this treatment affects the crystallization transition in our samples even if the material is left in an amorphous state after it. We

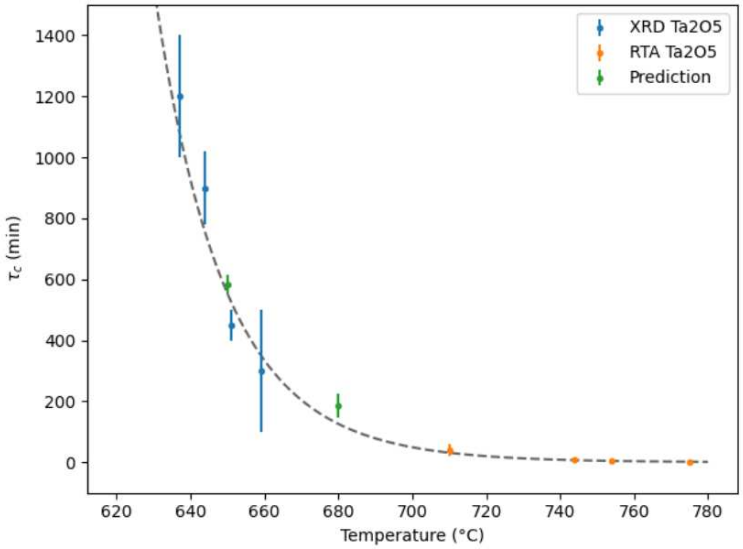

Figure 4.19: Comparison between the crystallization times measured in an isothermal process and the crystallization times predicted through a double kinetic experiment. The dashed line is the modellization performed on the isothermal data through the JMAK model.

took a batch of samples all obtained from the same deposition run (S22022) and treated half of them in an oven for 10 hours at 500°C to replicate the standard treatment, batch A, and left half of them as deposited, batch B. Taking one samples from each batch at the same time we then treated them via RTA to induce a partial crystallization state obtaining in the end nine different set of samples. Investigation via GIXRD showed that consistently across all samples batch A displayed a much higher degree of crystallization respect batch B proving that even if no crystallization is evident after the standard post-deposition annealing of 10 h at 500°C structural changes are happening in the material.

4.3.4 Effect of Ti Doping on Crystallization Kinetics

While the objective of this work was to study pure tantala crystallization kinetics to ease the understanding of how crystalline regions affect the coating loss angle and scattering, the material currently used in GWI is titanium-doped tantala. The choice of this dopant mainly comes from the fact that it has been observed that titanium doping in tantala allows for higher temperature and/or longer annealing time without the development of crystallization. We hence investigate how the presence of TiO_2 affects the crystallization kinetics.
The same experimental approach used to study the isothermal kinetic of

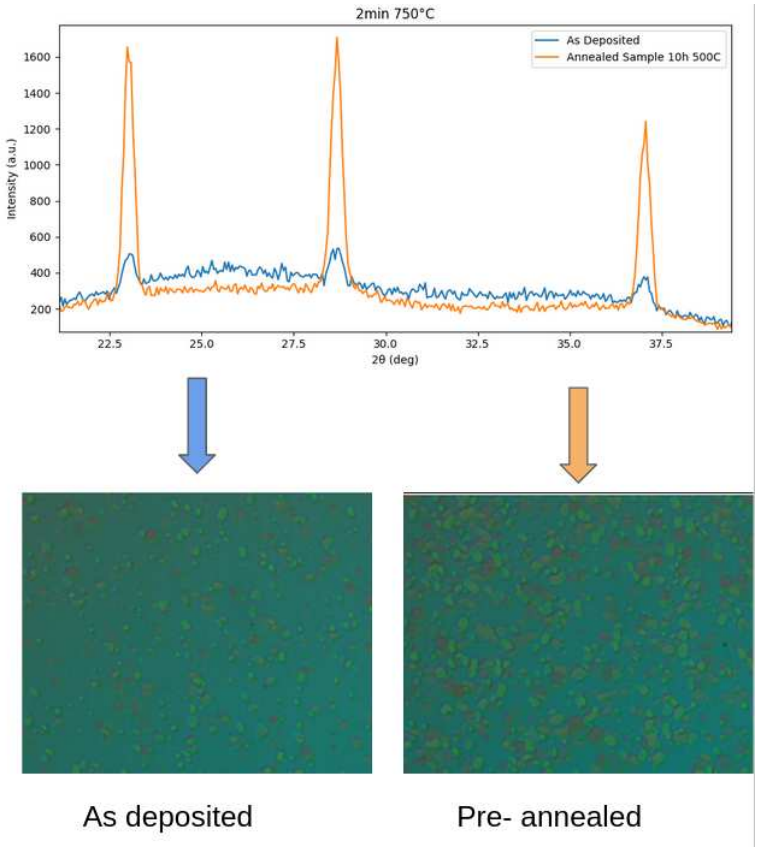

Figure 4.20: Comparison between the crystallization stae of a 10 hours 500°C pre-annealed sample from batch A and an as deposited sample from batch B. On the top the GIXRD spectra of the two samples, on the bottom two optical images of the samples.

tantala was used on four different samples of Ti:Ta_2O_5. After a first preliminary investigation in which it was observed that the sample crystallized with the same diffraction spectra as pure tantala (see subsection 5 for more details), four treatment temperatures, 680°C, 690°C, 700°C, and 720°C, were chosen and the samples measured *in-situ* accordingly. The obtained data can be seen in figure 4.22 in an Avrami plot .

The fitting of the initial part of the kinetics provide us with the values shown in Tab. 4.4. As it can be seen, the crystallization times obey the eq. 4.31 found in the case of pure Ta_2O_5, but with a very different energy value $Q = (3.52 \pm 0.09) \times 10^{-18}$ J as visible in figure 4.23. The retardation effect induced by Ti on tantala kinetics can be easily seen by comparing the two Avrami model parametrizations obtained for the two material as in figure 4.24. This indicates that the energy required to promote the combined nucleation and growth of the Ta_2O_5 crystal grains is increased by the presence

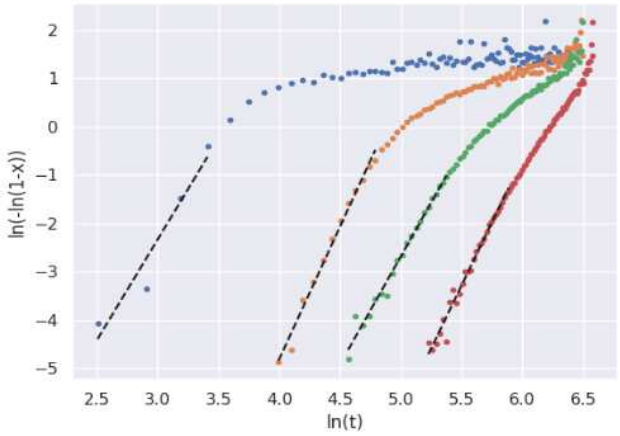

Figure 4.21

Figure 4.22: Data obtained from the study of isothermal crystallization kinetics in Ti:Ta_2O_5 for the Crystalline fraction versus time

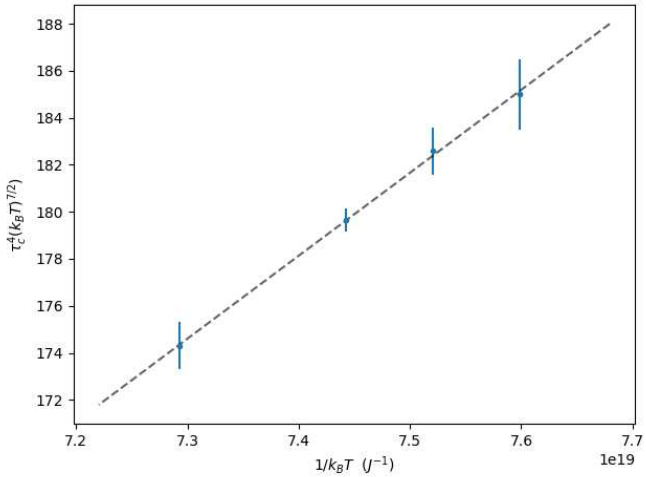

Figure 4.23: Data obtained from the study of isothermal crystallization kinetics in Ti:Ta_2O_5 for te dependence of the crystallization time from the soaking treatment temperature.

of Ti. The detailed mechanism leading to this phenomenon is still to be understood.

Temperature (°C)	τ_c (min)	α
680	489 ± 7	5.2 ± 0.1
690	271 ± 4	4.5 ± 0.1
700	131 ± 2	5.5 ± 0.2
720	35 ± 4	4.2 ± 0.8

Table 4.4: Parameters obtained from the analysis of Ti:Ta_2O_5 isothermal crystallization kinetics

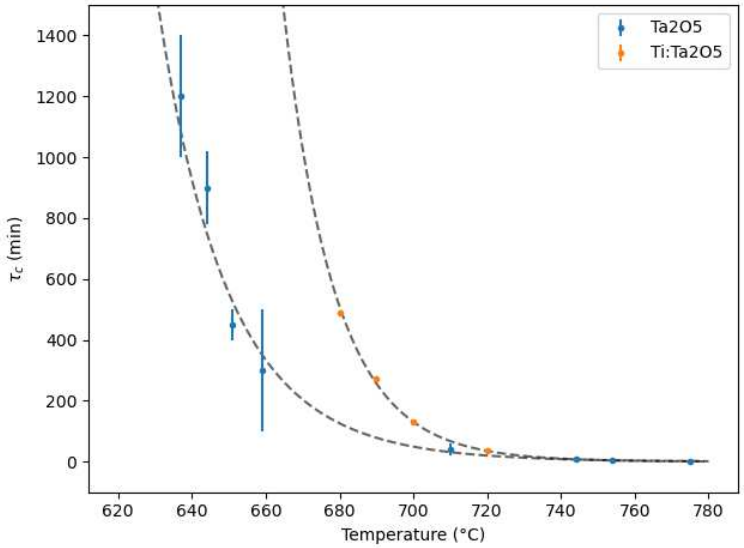

Figure 4.24: Comparison between the crystallization times for Ta_2O_5 and Ti:Ta_2O_5 as a function of temperatures. The two dashed lines are the modelization performed in this chapter.

Chapter 5

On the structure of crystalline grains in annealed Ta_2O_5

5.1 Structural analysis of crystalline grains in annealed Ta_2O_5

The structural properties of crystalline tantala and the specific morphology in which it forms in our samples is of key interest to fully understand the optical and mechanical changes induced by thermal treatments. Although in literature many works exist on the properties of Ta_2O_5 the structure in which tantala crystallizes at low temperatures is not fully agreed on since many different polymorph of Ta_2O_5 can coexist in a single sample [34] [35] [36].

Figure 4.9 shows the typical diffraction spectrum one of our tantala samples displays once it crystallizes. The diffractogram we obtain is compatible with the ones available in literature and, upon a search-match process on the peak positions performed the with QualX software [59] based on data from the PDF2 database [60], several structures of tantalum oxides appeared to be compatible with our XRD data. Among them β-tantala with an orthorhombic unit cell with a Pccm symmetry and with lattice parameters $a = 6.217$ Å, $b = 3.677$ Å, and $c = 7.794$ Åis often encountered in literature (Fig. 5.2).

Among the many structure found we favoured in our analysis a more recently proposed one from [21] since it was able to match the predictive power of other structures while utilizing a lower amount of free parameters in the cell model. The proposed unit cell is a variation of δ-tantala characterized by a P6/mmm symmetry and unit cell parameters a=7.19 Åand c=3.83 Åshown in Fig. 5.3.

We tried to perform a Rietveld refinement on the diffraction spectra ac-

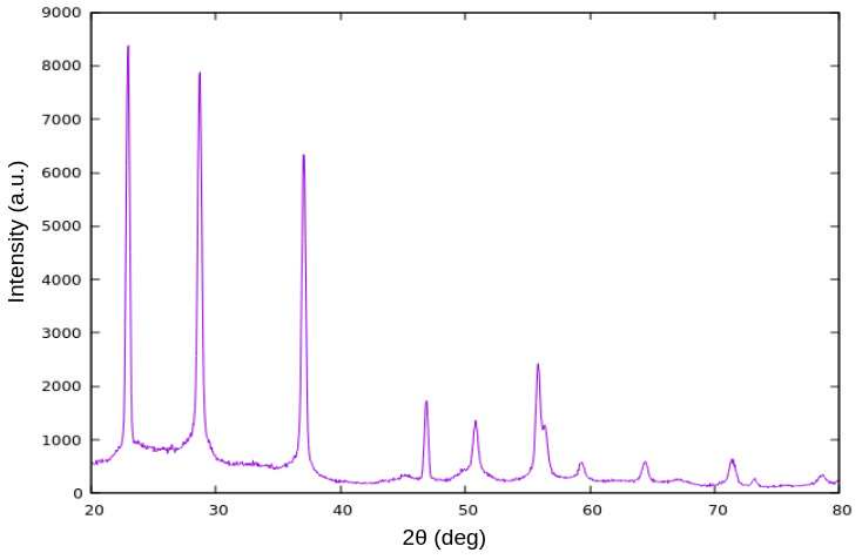

Figure 5.1: Diffraction spectrum of Crystalline Ta_2O_5

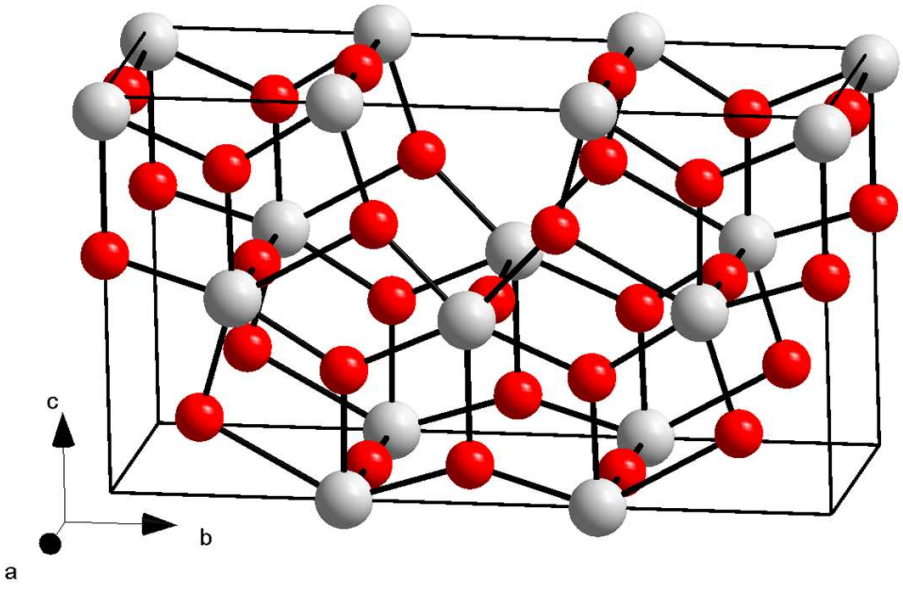

Figure 5.2: Caption

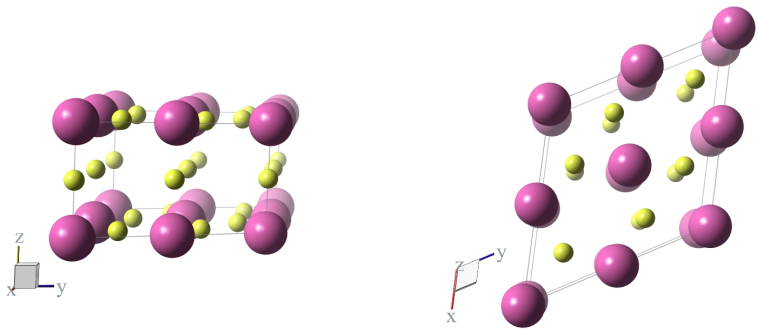

(a) (b)

Figure 5.3: Ta_2O_5 unit cell derived from the δ-tantala phase with P6/mmm symmetry.

quired, using multiple cell structure among the ones available in literature. We used the MAUD software [53] assuming a simple model of a polycrystalline sample and considering the GIXRD geometry used in our experiments to obtain the experimental spectra. The peak broadening is modeled with the help of an isotropic strain-size model and the experimental resolution was calibrated by means of a LaB_6 standard. In our refinement we considered as free parameters the lattice parameters, the isotropic B factors, B_{iso}, the size Δ and RMS- microstrain ϵ parameters. No changes in the atomic positions are allowed. Other parameters necessary to model the instrumental data such as the beam intensity, the spectrum background etc. were refined in the process but we are not considering them thereafter for sake of brevity. We considered as most plausible candidates from our preliminary assignment two phases: orthorombic β-tantala (space group $Pccm$) and δ-tantala (space group $P6/mmm$). The latter phase is structurally much more simple than the former, thus it would be desirable to get a description of our results in terms of this model or some modification of it.

Multiple Rietveld refinement performed on various set of data indicated that the proposed unit cells are able to explain the data with the same level of predictive power. An example of a Rietveld refinement performed on our data can be seen in figure 5.4 where the δ-Ta_2O_5 model hase been used. As it can be seen, while the overall agreement is not bad, some smaller features indicated with arrows, are not correctly captured by our model.

In order to better elucidate the structure of our Ta_2O_5 coatings after crystallization, we resorted to a dedicated experiment at the ID 15a beamline at the ESRF synchrotron radiation facility in Grenoble, as described in paragraph 3.2.4. The scope of the experiment was twofold: on one hand, by taking advantage of the high SNR of synchrotron experiments, investigate

Parameter	Units	β-Ta_2O_5	δ-Ta_2O_5
a	Å	6.212 ± 0.003	7.224 ± 0.002
b	Å	3.972 ± 0.002	-
c	Å	7.884 ± 0.003	3.900 ± 0.002
α	deg	90	90
β	deg	90	90
γ	deg	90	120
B_{iso}	$Å^2$	1.94 ± 0.03	1.47 ± 0.04
Δ	Å	2190 ± 40	1800 ± 40
σ_{RMS}	-	0.00005 ± 0.00001	0.0046 ± 0.0002
R_{WP}	%	15	13

Table 5.1: Rietveld refinements for the two structural models β-Ta_2O_5 and δ-Ta_2O_5 obtained on a typical spectrum of a fully crystallized sample.

in-situ the diffraction features of crystalline Ta_2O_5 during the evolution from amorphous to crystalline. On the other hand, investigate in more detail the size of the crystalline nuclei by means of a total scattering experiment.
In this experiment a set of Ta_2O_5 samples deposited on a Si substrate by means of Ion Beam Sputtering have been studied. We considered three samples with different thicknesses, as reported in table 5.2. The samples

Sample code	Thickness (nm)	PDF Size (Å)
D	2500	60.9
G	1000	75.8
E	500	102.5

Table 5.2: Samples used for the in-situ PDF experiment.

were mounted on a heating stage and the X-ray scattering was measured as a function of time while the samples were kept at a fixed temperature $T = 690°C$ using the 2D detector placed after the sample. The integration time required to measure a full spectrum was of 0.2 s, while a total measurement lasted several minutes. At this temperature such an acquisition was sufficient to observe the transformation of amorphous Ta_2O_5 into a crystalline, as witnessed by the appearance of narrow Bragg rings on the diffractogram and the disappearance of the amorphous signal (see Figure 5.5). For each frame, the 2D diffractogram has been transformed into a 1D plot by integration along the azimuthal angle, while the radial distance was transformed in q units by a suitable calibration procedure.

Figure 5.6 shows the time evolution of the diffraction data obtained

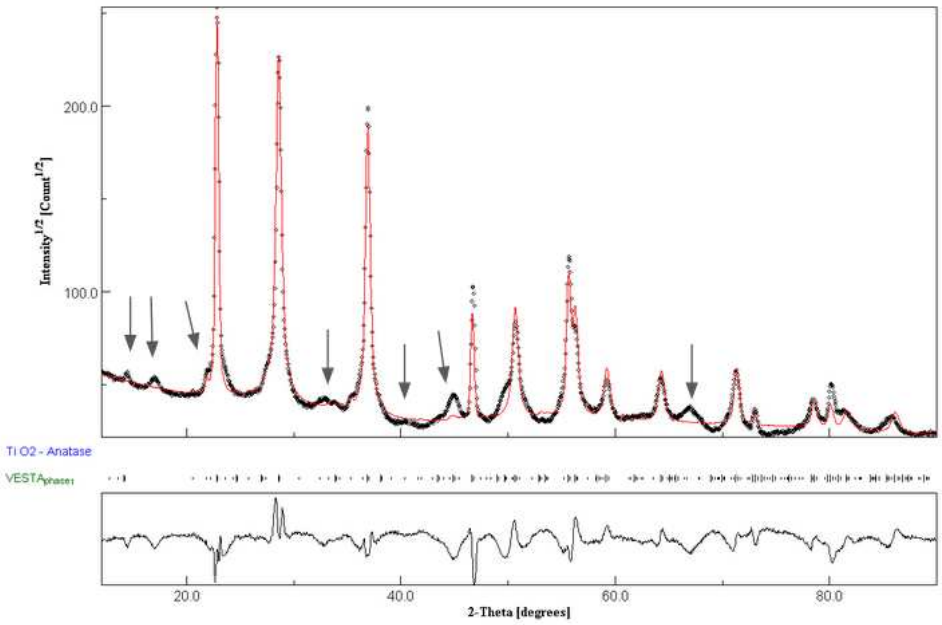

Figure 5.4: Rietveld Refinement of crystallized pure tantala diffractogram using the unit cell proposed in [21]. The arrows on the picture show how some features of the data are completely absent from the model prediction leading to the belief of a polimorphism happening in the material.

versus time in our three samples. We can see that in sample E, there is a peak at $Q \sim 2.2$ Å^{-1} which is not present for the sample D. In the case of sample G, instead the same peak, initially absent, appears only around the spectrum number 10. A number of other small features are also visible by comparing the spectra. It can be seen that the intensity of the peak at $Q \sim 2.2$Å^{-1} is correlated to the intensity of the small peaks at $Q \sim 1.0$Å^{-1} and $Q \sim 1.2$Å^{-1}. It is clear that those peaks correspond to the ones highlighted in Fig. 5.4 which were not previewed by the δ-Ta_2O_5 model, hinting that the above-mentioned features originate from a second crystalline phase which may or may not start to form together with the main tantala phase. Another possible explanation is that we are in presence of a polymorphism in which, after a certain time, a part of the main phase may transform into a second one characterized by the new peaks. The comparison among the three samples when the transformation process has ended is reported in Fig. 5.7.

Besides the formation of the secondary phase, it should be noted that the intensity of the peak at $Q \sim 1.6$Å^{-1} is very different for sample D with respect to the others. For what concerns the peak positions, we can see that the three samples present some differences also in this respect. However this feature can be explained in terms of a systematic error of the

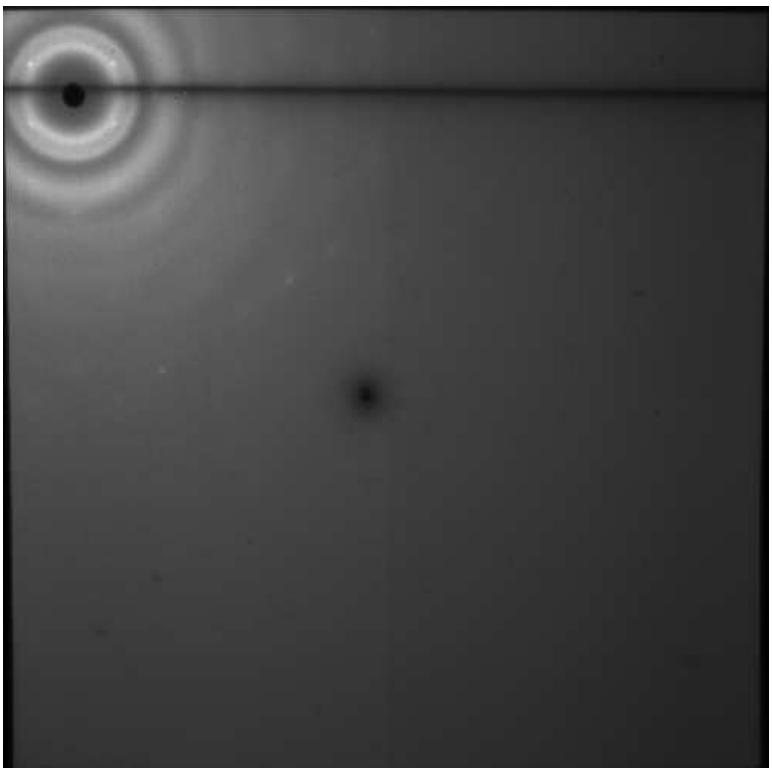

Figure 5.5: 2D Diffractogram recorded at ESRF for sample D

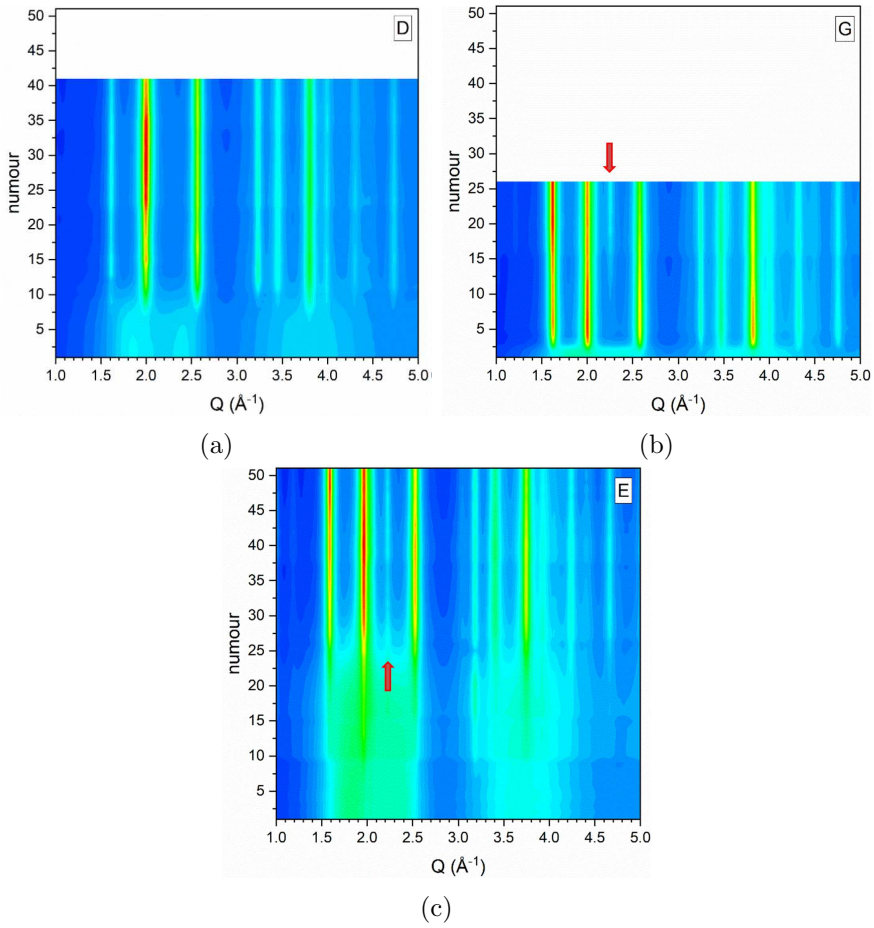

Figure 5.6: Time evolution of the diffraction spectra for the three samples of Tab. 5.2. The colormap represents the signal intensity in arbitrary units. The arrows shows how in two out of the tree samples a second set of peaks appear during the treatment.

apparatus: due to small movements of the sample stage (e.g. caused by thermal dilation when the stage heats up to high temperature), the sample - detector distance may vary from measurement to measurement, which brings a fictitious "stretching" of the data along the x - axis.

The samples D and E appears as two extreme cases, as the former shows a very small amount of the unknown phase, while in the latter it seems to be present along all the measured time interval. We tried to fit the former by using assuming a $P6/mmm$ hexagonal model, as in Fig. 5.4 . The agreement is rather satisfactory, however in this case, we used a model with a shorter lattice parameter i.e. $a \sim 3.62$Åand $c \sim 3.90$Å.

To get further insight, we processed our diffraction data in order to compute the Pair Distribution Function. The results are reported in Fig. 5.9,

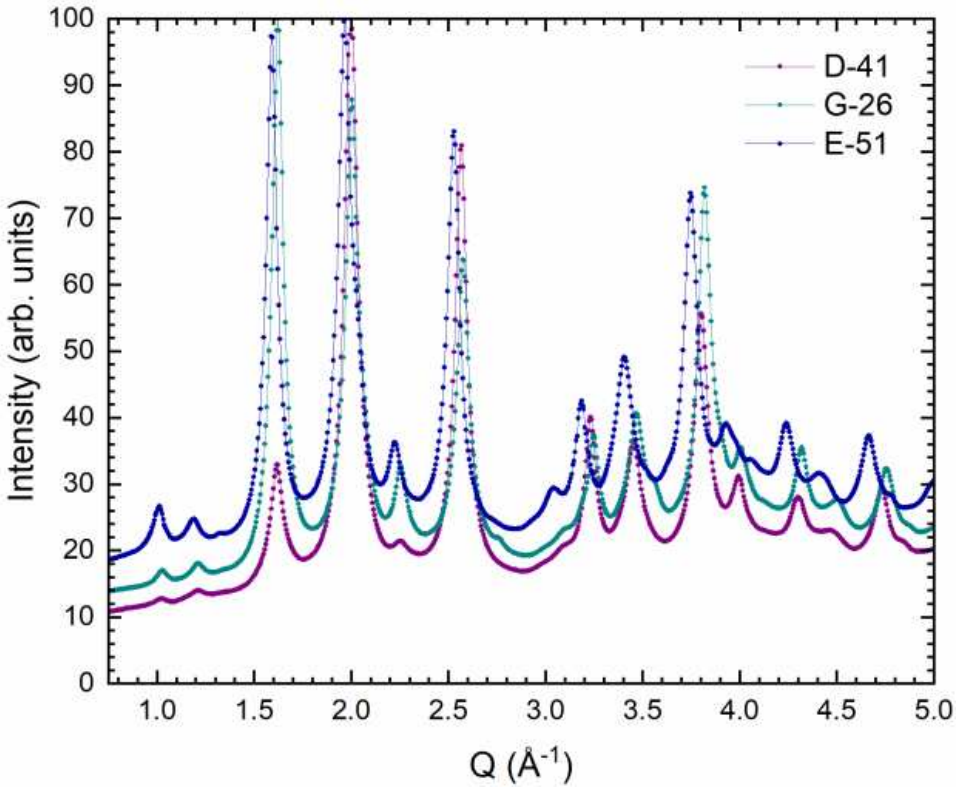

Figure 5.7: Diffraction spectra acquired for the three different sample at ESRF after the crystallization process occured.

together with a fit computed using the same structural model assumed in Fig. 5.8. It can be seen that the model correctly fits the data for distances larger than > 15 Å, while at smaller distances there is a noticeable disagreement. This can be interpreted by considering that the $P6/mmm$ model used is an approximation for the average structure, while at shorter distances the structure locally deviates from such a model.

By repeating the Rietveld fit over all the spectra, it is possible to extract the time evolution of the lattice parameters and of the coherent diffraction size for sample D. The latter quantity should not be understood as the average size of the crystalline grains reported in fig. 4.10, but as a measure of the average range over which the lattice can be considered periodic. As it can be seen, in a first stage after the appearance of the Bragg peaks the structure evolves, with the lattice parameters changing towards their equilibrium value. On the other hand, the domain size is initially limited to about 1 nm and after the stabilization of the structure, increases quickly to an equilibrium value around ~ 60 Å.

This result is also coherent with the PDF analysis performed at the beginning and at the end of the experiment and with the results obtained

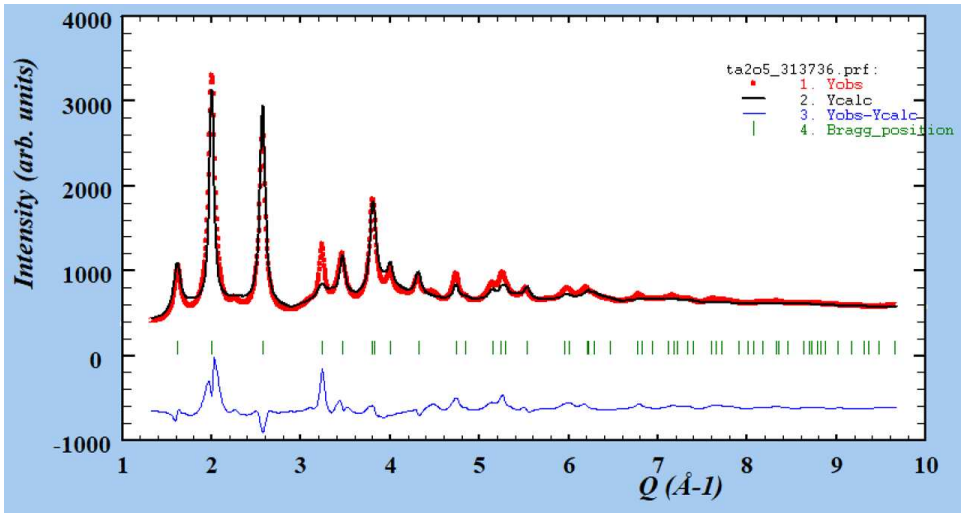

Figure 5.8: Comparison of the diffraction data for sample D (spectrum #41) corresponding to a fully crystallized situation and a Rietveld fit based on a $P6/mmm$ unit cell similar to the one described in fig. 5.4 but with a different choice of the lattice parameters. The blue line on the bottom is a difference plot.

from the XRD analysis in Tab 5.1, when the sample is in its fully amorphous or fully crystallized state, respectively. In figure 5.11 the two PDFs are reported for sample D. As it can be seen, in the amorphous state the analysis reveals a correlation up to $\sim$ 10Å, while the crystallized sample show a long range order that extends beyond $\sim$ 100Å. The fact that PDF analysis can probe correlations up to those distances is one of the advantages of this technique. This value is not in disagreement with the Rietveld analysis since the latter considers the average correlation length while PDF can sense even extreme values as it is based on a direct treatment of the diffraction spectrum and not on a model-based fitting.

The analysis of sample E confirms that the hexagonal structure cannot be used to describe the experimental data. A reasonable agreement can be found assuming a more complicated monoclinic cell belonging to the point group $P2/m$ (see Fig. 5.12. The fit results provides $a \sim 6.28$Å, $a \sim 4.05$Å, $c \sim 5.32$Å, and $\beta \sim 93$°C. It is possible to consider this second cell as a distortion of the higher symmetry phase $P6/mmm$ used to analyze the previous sample, but additional studies are required to clarify those aspects. The PDF analysis was repeated for the three samples to characterize. Using this analysis we characterized the size of the coherent diffraction domains, which are reported in table 5.2. Interestingly they seem to be anti-correlated with the film thickness hinting that in thinner coating layers the crystalline grains develops with a higher degree of long-range order, perhaps for some reason

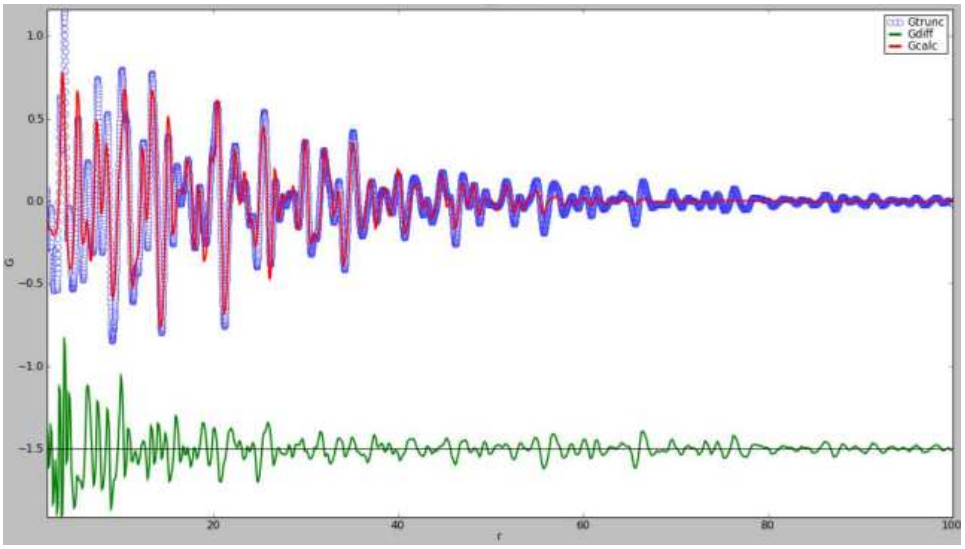

Figure 5.9: Computed PDF function for the sample D after crystallization (blue dots) and fitting (red line) using the same structural model used to fit data in Fig. 5.8. On the bottom the difference plot (green).

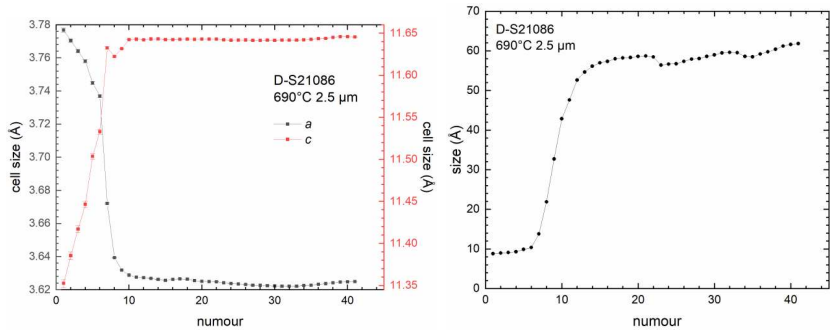

(a) (b)

Figure 5.10: a) Time evolution of the lattice parameter for sample D assuming an hexagonal unit cell with space group $P6/mmm$. b) time evolution of the coherent diffraction size. The time step is 0.2 s.

related to the 2D growth mode of the latter. To conclude, the structure of crystallized Ta_2O_5 can probably be understood in terms of a $P6/mmm$ hexagonal model. This structure describes quite well the average structure of the crystallized fraction, even if local deviations occurring on the short scale (possibly related to an orthormbic distortion) are present.
The hexagonal phase identified as the best candidate for the structure of our crystallized Ta_2O_5, predicts a density of the material of 8.6 g/cm^3 if we compute it using the cell parameters found from our Rietveld analysis. As

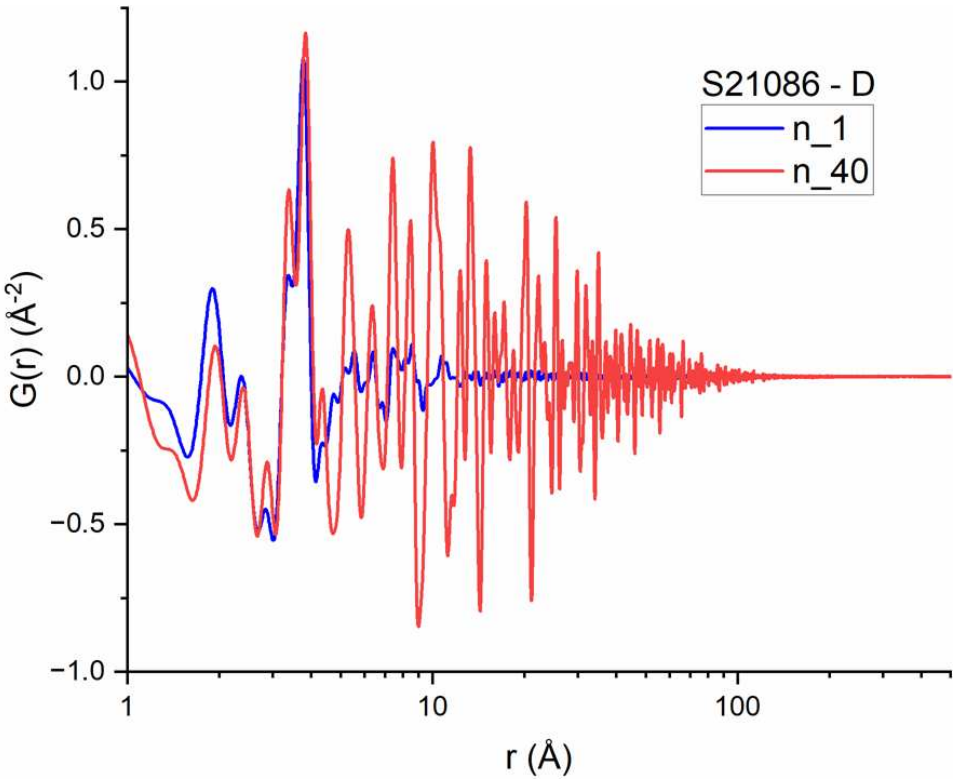

Figure 5.11: Comparison of the PDF before and after thermal treatment in sample D.

the density of amorphous tantala from LMA is 7.5 g/cm^3 [15], we expect that crystallized regions are about 13 % denser with respect to the matrix.

This finding is in agreement with AFM measurements performed on partially crystallized samples, see Fig. 5.13, which show in correspondence with crystalline grains a depression of the sample surface of about 10% of the film thickness.

As the refractive index is determined essentially by the electronic density of a material, we may expect that the same variation of the material density could be observed on the material refractive index. From a refractive index of 2.08 [15] we expect hence the refractive index of the crystallized material to be around 2.35 and we expect very strong scattering phenomena due to the high contrast.

5.2 Crystalline phases in TiO_2:Ta_2O_5

When TiO_2 is added to Ta_2O_5, new phases are detected in samples annealed for sufficiently long time and/or at sufficiently high temperature. In

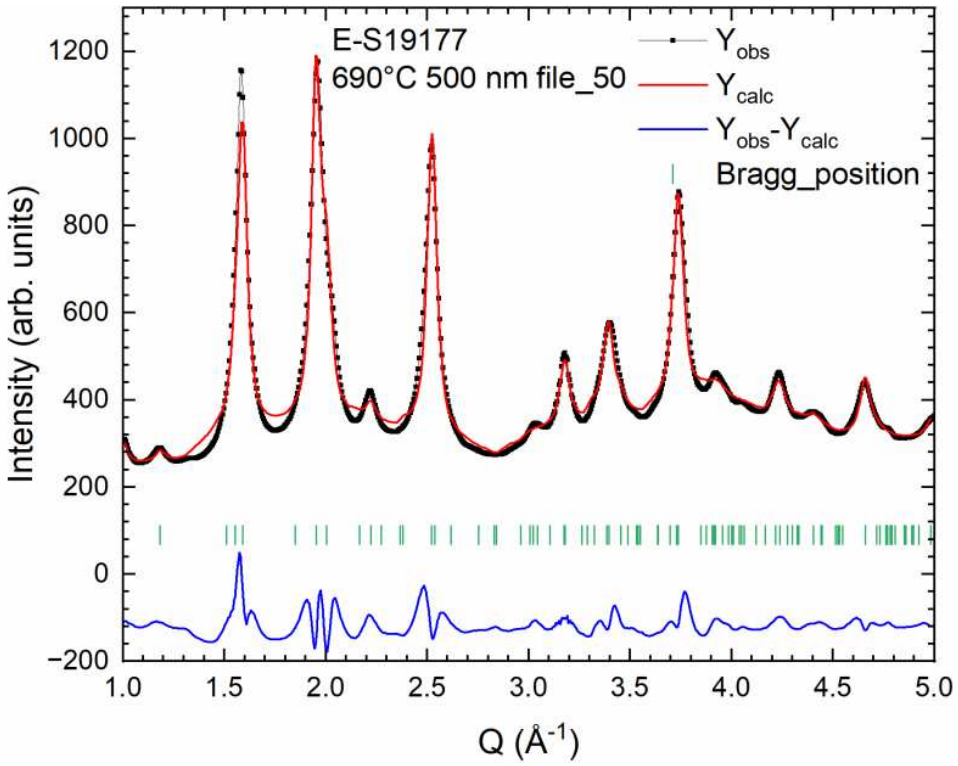

Figure 5.12: Rietveld fitting of the diffraction spectrum for sample E. The model assumes a P2/m monoclinic unit cell.

Fig. 5.14 it is reported a comparison between a titania-doped coating with about 25% TiO_2 treated at 680°C and another one treated at 990°C. While the sample treated at lower temperature is characterized by a diffraction spectrum analogous to the ones observed in the preceding section, the sample treated at higher temperature develops an additional series of peaks. From a search-match analysis performed with the QualX sowtware [59], it turns out that the additional peaks corresponds to the formation of crystalline TiO_2 in the anatase form. The ternary phase diagram for the system Ti-Ta-O [77] predicts, for the temperatures and the concentrations used in this study, that TiO_2 and Ta_2O_5 should exist as a homogeneous solid solution. Our data displaying instead crystalline tantala and crystalline titania point towards a demixing process happening in the material. The reason for this demixing is not clear and further investigation is required to understand its origin.

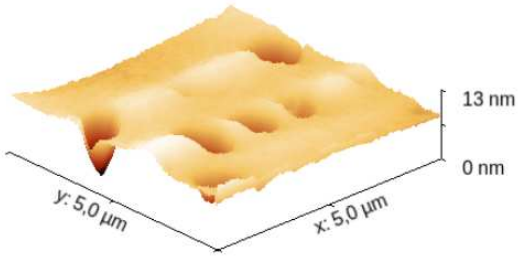

Figure 5.13: 3D AFM image of a partially crystallized Ta_2O_5 sample. The surface present valleys whose depth correspond roughly to 10 % of the coating thickness (for this sample $\sim$ 200 nm total thickness).

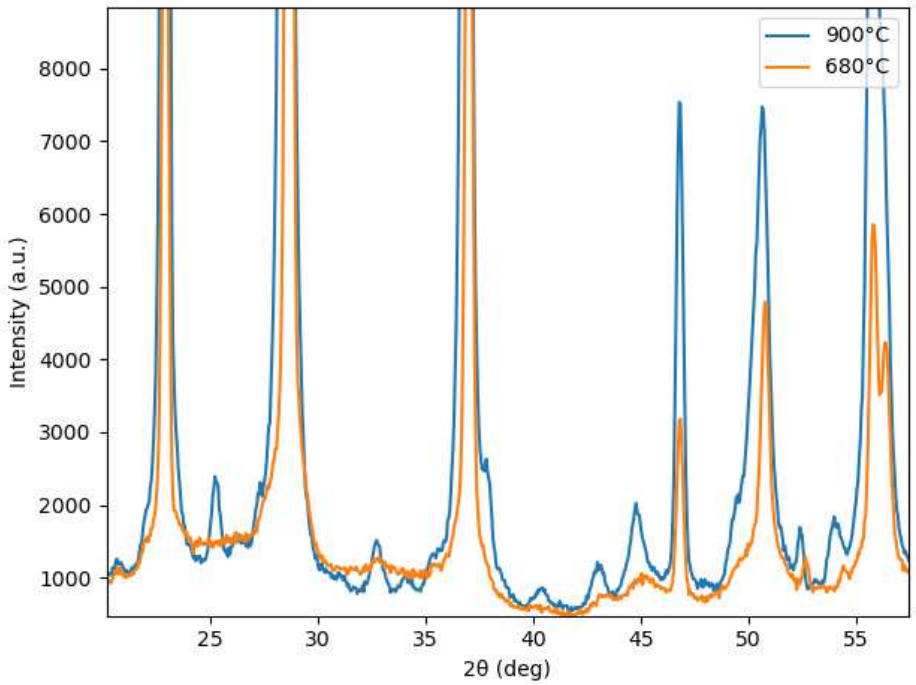

Figure 5.14: Diffraction spectra of two samples of Ti:Ta_2o_5 treated at different temperatures. The sample treated at higher temperature develop a new set of peaks related to the formation of crystalline TiO_2 in the anatase phase

Chapter 6

Optical Characterization

We have seen in chapter 2 how the extreme sensitivity of GW interferometers poses strong requirements on the quality of the optical components of the system. Among the issues one has to consider, one of the most important concerns regards the optical losses and in particular those due to scattering. Stray light originated by imperfections in the optics deviates from the main beam: if allowed to recouple with the interferometer beam at a later stage, such light can bring in phase noise due to the vibrations of parts that back-reflect it and can also cause power noise.
The main expected disadvantage of inducing a partial crystallized state on a coating is that the crystalline grain act as a source of scattering. The amount of the induced stray light is expected to be strongly dependent on both the crystalline fraction and the grain size distribution: therefore it is crucial to investigate the link between the optical losses and these two quantities.
This chapter offers a brief introduction to the most useful concepts to investigate stray light, section 6.1, and will present the unique characteristics of scattering in a thin film, section 6.2. Section 6.3 presents the design ideas and the construction of the facility dedicated to the study of stray light in Padova and lastly section 6.4.1 presents the measurement performed and the results obtained.

6.1 Stray Light

The challenge of Stray light in optical systems arises from the many interactions between light with surface boundaries across different media. As light traverses these boundaries classical optics principles such as Fresnel's equations and Snell's law allow to predict the behavior of the reflected and the refracted beam: these laws assume the surfaces to be perfectly smooth and the material to be homogeneousHowever, any realistic modelling need to include imperfections, which makes the picture more complex.

The introduction of surface roughness disrupts this conventional understanding, giving rise to surface scattering: portions of the incident light deviates from the predicted paths, introducing complexities that are central to the stray light problem. Furthermore, if the medium is heterogeneous, incorporating small optical defects, volume scattering becomes a relevant factor. Within the material more reflections and refractions arise as the light beam travels trough it. Often, both surface and volume scattering need to be considered. To correctly address the stray light problems one must then toughly investigate the optical design, the material properties, and the environmental factors involved.
In GW interferometers the preferred approach to tackle stray light induced noise is to minimize the amount of stray light which is produced and to absorbe it. This ends up in setting strong requirements on te quality of the optical components; for instance the substrates of the Advanced Virgo mirrors have been polished to a level of few atom layers; the requirements for the total losses of the mirror coatings by scattering are a few parts per million.

6.1.1 Bidirectional Scattering Distribution Function and Total Integrated Scattering

When a beam impinges on a sample the different possible processes of scattering diffuse the light across all directions around the sample. Defining a sphere centered on the point where the beam hit the sample, see figure 6.1 for reference, at each point across its surface the amount of light scattered depends on the relative orientation of the beam and the sample, the wavelength, the power, and the inherent characteristics of the sample (material, roughness, cleanliness...). Those behaviours are accounted for by a number of functions, each one focusing either on a specific portion of the scattering sphere or on a different source of scattering. The *Bidirectional Reflectance Distribution Function (BRDF)*, for instance describes the scattering happening in reflection from a surface, while the *Bidirectional Volume Distribution Function (BVDF)*, describes the scattering happening in the bulk of a sample. All these functions are just a subset of a more general one called the *Bidirectional Scatter Distribution Function (BSDF)* that describe the scattering happening across the whole scattering sphere disregarding the origin of the scattered light.
The BSDF, defined in 1970 by F. E. Nicodemus [78], is historically defined as the ratio between the differential radiance over the differential irradiance of a surface:

$$BSDF(\theta_i, \phi_i, \theta_s, \phi_s) = \frac{dL}{dE} = \frac{dP_s(\theta_i, \phi_i, \theta_s, \phi_s)}{d\Omega_s} \cdot \frac{1}{P_i \cos\theta_s} = \frac{P_s(\theta_i, \phi_i, \theta_s, \phi_s)}{P_i \cos\theta_s \Omega_s} \tag{6.1}$$

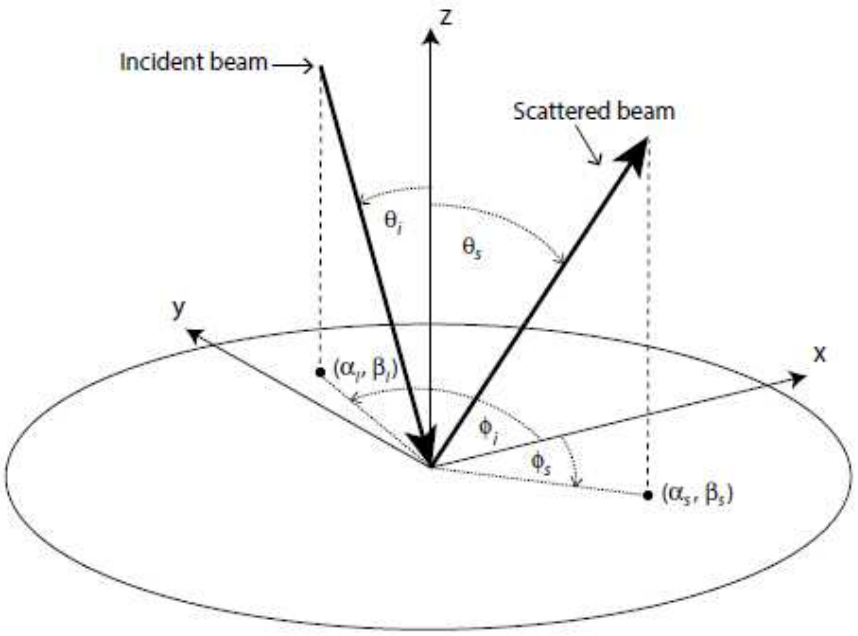

Figure 6.1: Scattering Geometry adopted through this work. Image from [28]

where P is the optical power, the subscript "i" indicates the incident beam, the subscription "s" indicates the scattered component, and the leftmost term is obtained by substituing the derivative of the power respect the solid angle with the ratio between the scattered power P_s over a small solid angle Ω_s. This definition works only when describing the scattering originating from a surface, hence the appearance in it of the therm $1/\cos\theta_s$ accounting for the change in the projected area for the scattering at different scattering angles. Since in general one wants to describe the light scattering as a product of multiple sources and not just a single surface, it has become the norm to utilize not the *BSDF* but the *cosine corrected BSDF (cBSDF)* since in most cases the cosine term hold no physical meaning.

$$cBSDF = BSDF \cdot \cos(\theta_s) = \frac{P_s}{P_i \Omega_s} \tag{6.2}$$

While in this work we differentiated between this two quantities, in literature there is much confusion and one must pay attention because often the *cosine corrected BSDF* is indicated just as *BSDF*.
In general measuring and modelling the *BSDF* function can be very difficult. In many applications where the fine details of the scattering distribution are not required, it's common to utilize a different function: the *Total Integrating Scattering (TIS)*. As in the case of the *BSDF*, the *TIS* was originally defined

to describe surface properties hence, even if in its name the therm *Total* appears, this quantity usually describe only the amount of light that is scattered in in one semisphere defined by the sample surface by an object thus it may be useful to differentiate between the reflected TIS and the transmitted TIS. In our case we focus on the reflected TIS, here TIS_R:

$$TIS_R(\theta_i) = \int_{\Omega_R} \frac{1}{P_i} \frac{dP_s}{d\Omega_s} d\Omega = \int_0^{2\pi} \int_0^{\pi/2} \frac{P_s}{P_i \Omega_s} \sin\theta_s d\phi d\theta_s = \tag{6.3}$$

$$= \int_0^{2\pi} \int_0^{\pi/2} cBSDF \sin\theta_s d\phi d\theta_s \tag{6.4}$$

Since energy conservation must hold one can then in general describe the power balance in a scattering event as:

$$P_i = P_T + P_R + P_A = P_{T,spec} + P_{T,scatt} + P_{R,spec} + P_{R,scatt} + P_A \tag{6.5}$$

With the subscriptions T, R, and A standing for Transmission, Reflection, and Absorption. Equation 6.3 is then equal to:

$$TIS_R = \frac{P_R}{P_i} = \frac{P_{R,spec} + P_{R,scatt}}{P_i} \tag{6.6}$$

so the TIS value is an adimensional number between 0 and 1; however other definitions of the TIS are commonly used in literature, in particular the other most widespread one found in many references like [47] is:

$$TIS_R = \frac{P_{R,scatt}}{P_{R,spec} + P_{R,scatt}} \tag{6.7}$$

This definition can be used for highly reflective surfaces but cannot be assumed valid in general. For instance for an AR coated surface where $P_{R,spec}$ tends to vanish, one would get TIS =1 regardless of the sample roughness. Moreover this definition requires a way to differentiate between the reflective scattering and the specular reflection, a task that is not univocally accomplished. A particular care must be withheld then when interpreting TIS results from different sources due to the different definitions. While the *TIS* has the advantage of being both an easier to understand and to measure quantity with respect to the *BSDF*, it's also a potentially misleading quantity since it's much more prone to systematic errors in its measurements (see Appendix A for a more detailed explanation). The main problem associated with *TIS* measurements is that often they are provided as a single number disregarding any information on how this measurement was taken. A perfect measure of the whole scattering half-sphere is impossible and in many cases even small regions not collected can lead to big differences in the final estimate of a sample *TIS*.

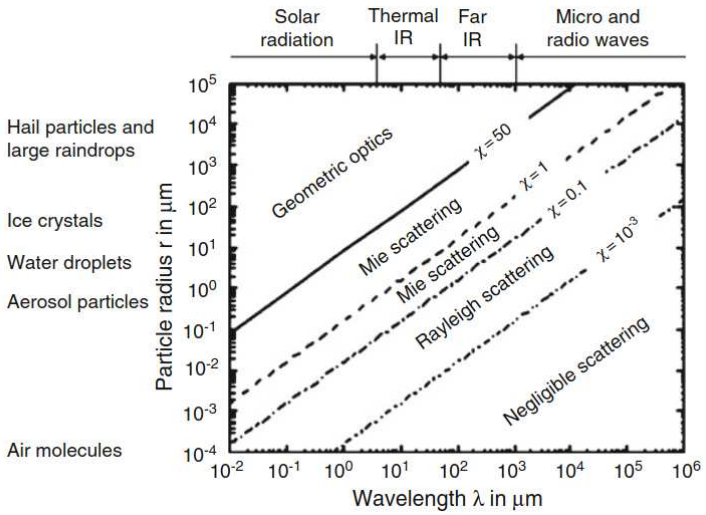

Figure 6.2: Regions of application of the different scattering theories. Image courtesy of [49]

6.2 Scattering sources and models

The scattering processes due to the presence of small defects may be differentiate on the base of the relation existing between the incident wavelength λ and the characteristic dimension r of the object originating the scattering. Empirically it can be found that different regimes are expected depending on the dimensionless parameter:

$$x = \frac{2\pi r n_{env}}{\lambda} \tag{6.8}$$

with n_{env} refractive index of the environment where the scattering is taking place. For small values of this ratio, $x \lesssim 0.1$, the individual features of the scattering sources are basically irrelevant and in almost all cases the phenomena occurring can be described through the *Rayleigh scattering model*. Starting from $x \sim 0.1$ the shape of the sources become relevant; in the case of spheres an exact solution of Maxwell's equations can be found producing *Mie Scattering Theory*. This framework actually works for spherical objects across all dimensions and naturally produce Rayleigh scattering when x is small. For non-spherical object the situation becomes more complicated and one must usually solve numerically Maxwell's equations. However, in the range $0.1 \lesssim x \lesssim 100$, Mie Theory usually approximates well enough the results for most practical applications. For values of x greater than 100 lastly usually one can use geometric optics for easiness of use. A visual summary of these models application region can be seen in figure 6.2

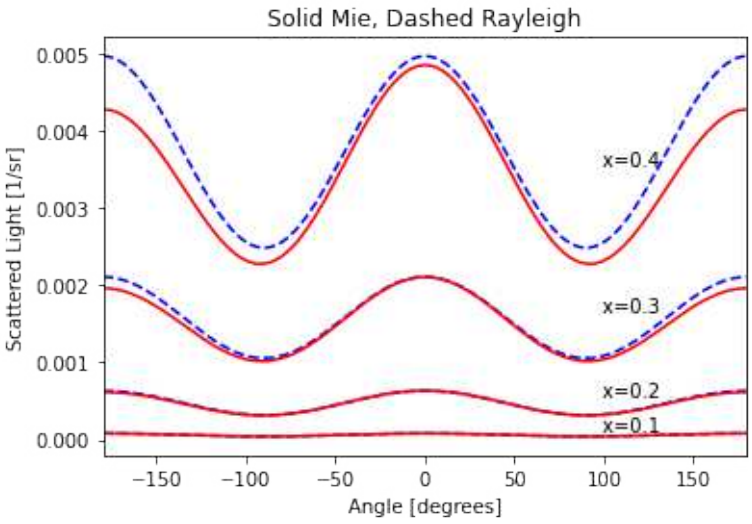

Figure 6.3: Comparison between Rayleigh scattering model BSDF and Mie Theory BSDF for different values of the size parameter x.

6.2.1 Rayleigh scattering

When dealing with objects whose dimension is much smaller than the wavelength of the incident radiation we fall in regime of the Rayleigh Scattering taking its name after Lord John Rayleigh who first described this effect in 1871 [48].
Assuming a spacial region randomly filled by small objects, in Rayleigh scattering, due to the random positions of the scatterers and due to their small dimension, the resulting radiation scattered at a generic point is incoherent regardless of the coherence properties of the impinging radiation. For a single scatterer of radius r composed by a material with refractive index n it can be found that the intensity of the scattered radiation I_s at an angle θ from the incident light and at a distance d from it is:

$$I(\theta, I_0, r, d) = I_0 \frac{1 + \cos^2\theta}{2d^2} \left(\frac{2\pi}{\lambda}\right)^4 \left(\frac{n^2 - 1}{n^2 + 1}\right)^2 \left(\frac{r}{2}\right)^6 \tag{6.9}$$

where I_0 is the intensity of the incident radiation of wavelength λ. In the case of multiple Rayleigh sources, due to the incoherence of the process, one can simply calculate the total intensity as the sum of the individual ones.

6.2.2 Mie scattering

As the x ratio increases the Rayleigh approximation fails to describe the scattering phenomena. In general one must then solve the Maxwell equations for the incident wave imposing the boundary conditions dictated by the specific

shape and material originating the scattering. This task is quite daunting and, most of the times, it's not realistic to solve exactly the diffraction problem. In the case of spherical particles inside an homogeneous medium, however, an exact solution exist and, in most practical applications, when the x ratio it's not too big, the specific geometric shape of the scatterers can be reasonably well approximated by a sphere. This model it's called *Mie scattering* after Gustav Mie who published it in 1908 [50]
The electric field scattered at an arbitrary position $\vec{r}$ after an electromagnetic wave traveling through the $\hat{z}$ axis interacting with an object placed in $\vec{0}$ can be written as:

$$\begin{pmatrix} \vec{E}_s(\vec{r}) \\ \vec{E}_p(\vec{r}) \end{pmatrix} = \frac{\exp\left[i\vec{k}\cdot(\vec{r}-\hat{z})\right]}{-i\vec{k}\cdot\vec{r}} \begin{bmatrix} S_1 & S_3 \\ S_4 & S_2 \end{bmatrix} \begin{pmatrix} \vec{E}_s(\vec{0}) \\ \vec{E}_p(\vec{0}) \end{pmatrix} \tag{6.10}$$

where the p and s subscriptions are used to differentiate between the polarization state of the wave. The S_i terms of the equation compose the scattering matrix of the process and depend upon the scatter angles θ_s and ϕ_s, the wavelength of the incident wave, and the size of the scatterer. To obtain the actual values of the scattering coefficients S_i one needs to solve Helmoltz equations:

$$\nabla^2\vec{E} + k^2\vec{E} = 0 \qquad\qquad \nabla^2\vec{H} + k^2\vec{H} = 0 \tag{6.11}$$

taking into account the fact that the scattering particles are homogeneous spheres, it's possible to find solutions for the S_i parameters in terms of Legendre's polynomial and spherical Bessel functions [27]. Another consequence of the spherical geometry is that the S_3 and S_4 term are null i.e. the scattering process maintains the polarization of the incident wave.
When the geometry of the scattering is not fundamental it's common, and simpler, to calculate with Mie theory the efficiencies of the scattering process: the extinction efficiency Q_e, the scattering efficiency Q_s, and the absorption efficiency Q_a with the former quantity being equal to the sum of the latter two. The efficiencies are defined as the ratio between the cross section of the process σ over the projected area of the particle:

$$Q_{e,a,s} = \frac{\sigma_{e,a,s}}{\pi r^2} \tag{6.12}$$

and have simple expressions in terms of the same multipole coefficients used for S_i. The scattering efficiencies are expecially useful when dealing with the scattering from an extended medium since we are usually interested on the attenuation a beam passing trough it experience. It can be shown that the attenuation in such a condition follows the Lambert-Beer law [80]:

$$-\frac{dI}{dz} = \mu_s I = \rho\sigma_s I = \rho\pi r^2 Q_s I \tag{6.13}$$

where ρ is number of particles per volume and z the direction of propagation.
As said, Mie theory is an exact solution of Maxwell equation for spherical scatterers so the values of S_1 and S_2 can be analytically determined however this task is still quite daunting. It can be shown, however, that Mie's scattering (contrarily to Rayleigh's one) is nearly-independent on the wavelength of the used radiation. The common solution is to adopt computational tools able to rapidly calculate their value; the one we use here is MiePython [68].

6.2.3 Bulk scattering

The first source of scattering one must take in account is the bulk scattering of the materials i.e. the scattering that originates inside the materials due to defects present inside their volume. Typical sources of scattering in an amorphous coating, from the biggest to the smallest ones, are external inclusions, bubbles, compositional inhomogeneities, crystalline regions and the molecules composing the material themselves.
The total scattering loss across a medium, accounting for different scattering sources can be written as:

$$-\frac{dI}{dz} = I\pi \sum_{i=1}^{N} \rho_i r_i^2 Q_s(x_i, n_i) \tag{6.14}$$

with x_i the size parameter and n_i the refractive index of the defect.
While bulk scattering is in many application the weakest form of scattering, Bulk scattering is unavoidable and much harder to mitigated since cleaning or polishing the material is ineffective. Bulk scattering is the leading contribution when dealing with gases where the per-molecule scatter is much higher respect liquids and solids.

6.2.4 Surface contamination

A second origin of scattering phenomena is the contamination of the surface of a material with external particles most commonly dust. Study of this type of scattering proves itself to be difficult since it's strongly dependant on the dimensions, the shapes, and the materials of the contaminants. As it can be seen in figure 6.4 the BSDF in this case has both the contributions of a back scattered wave and of a forward scattered one that reflects on the surface; we can write for this BSDF then:

$$BSDF(\theta_s, \theta_i) = \frac{1}{(2\pi/\lambda)^2 \cos(\theta_s)} \sum_{i=1,2} \sum_{j=1}^{N} f(x_j) \frac{1}{2} \left[R|S_i(x_j, n_j, \theta_f)|^2 + |S_i(x_j, n_j, \theta_b)|^2 \right]$$

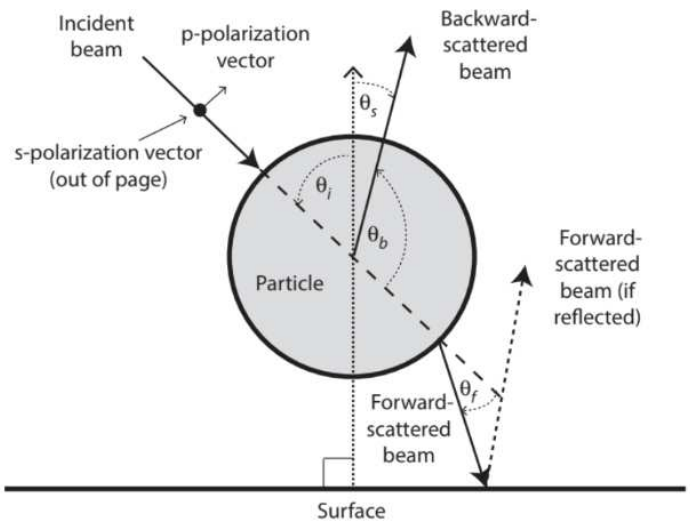

Figure 6.4: Scheme of the scattering happening at a surface due to particulate deposited on it. Image courtesy of [28]

where $\theta_f = \theta_s - \theta_i$ is the angle of forward scattering, $\theta_b = 180 - \theta_s - \theta_i$ the backward scattering angle, x_j are the size parameters of the contaminants, n_j are the refractive indexes of the contaminants, and f is the particle density function i.e. the number of particles with size parameter x per unit area. Due to the complexity surface contamination adds to the analysis of the scattering of a sample it's of the utmost importance to avoid it as much as possible hence it's advisable to perform scattering measurement only on thoroughly cleaned samples in clean environments to reduce this source to a minimum.

6.2.5 Surface Roughness

The last source of scattering we will explore in this text is the scattering originating due to the surface roughness of a material. Surface topography introduce perturbations of the wavefront that are usually described trough Rayleigh-Rice perturbation theory [69]. In transparent media both the transmitted and the reflected beam are affected by these perturbations and the description becomes more complicated.
The roughness of a surface can be defined as a measure of the deviation of a surface from a reference; many parameter definitions exist in the ISO standard to quantify the roughness but the one we use here is the RMS

roughness:

$$\sigma = \frac{1}{A}\sqrt{\int_A (h(x,y) - \langle h \rangle_A)^2 \, dxdy} \tag{6.15}$$

where A is the area of the surface we characterize, and $h(x, y)$ is the height of the surface at a specific point, and $\langle h \rangle_A$ the mean surface height. The technique used to assess the roughness of a material imply that each roughness measurement should come with an indication of the spatial frequency ranges sampled, because each technique has its own spatial resolution defining the bandwidth it can access. While the roughness is an important parameter to characterize a surface, it loses many information regarding the actual topology. Another useful quantity we can use to describe a surface that is also linked to the BSDF (see for example equation 6.20) is the *Power Spectral Density (PSD)*:

$$PSD(f_x, f_y) = \frac{1}{A}\left|\int_A h(x,y) e^{-2\pi i(xf_x + yf_y)}\right|^2 \tag{6.16}$$

where f are the spatial frequencies in the x and y directions defined through the hemispherical grating equations as:

$$f_x = \frac{\sin(\theta_s)\cos(\phi_s) - \sin(\theta_i)}{\lambda} \qquad fy = \frac{\sin(\theta_s)\sin(\phi_s)}{\lambda} \tag{6.17}$$

The link between the RMS roughness and the PSD can be expressed as:

$$\sigma = \int_{f_{min}}^{f_{max}} PSD(f_x, f_y) df_x df_y \tag{6.18}$$

6.2.6 Lambertian scattering model

For an ideal surface with a perfect Gaussian roughness (i.e. an height distribution that follows a Gaussian random distribution) a simple model that can be used is the Lambertian scattering model:

$$cBSDF(\theta_s) = K\cos(\theta_s) \tag{6.19}$$

Among the various materials and radiative process only blackbody emission seems to follow the behaviour depicted. Most materials tend to exhibit an higher reflectance around the specular reflection with respect to what is predicted by the Lambertian model. This model, while being not much realistic is however useful for its semplicity and many rough surfaces can be reasonably approximated by it.

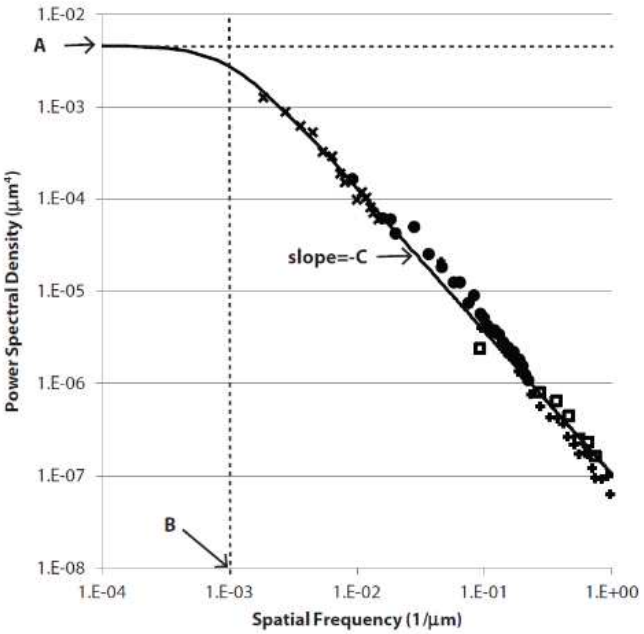

Figure 6.5: Example of the typical PSD of a Material. Note how the different parameters of the ABC model can be easily linked with the features of the PSD. Image from [28]

6.2.7 Harvey-Shack scattering Model

For smooth surfaces, usually a better approximation of the scattered light is offered by the Harvey-Shack model. Harvey-Shack model can be obtained as a limit of Rayleigh-Rice perturbation theory for $\sigma \ll \lambda$. In this conditions Rayleigh-Rice theory predicts the BSDF produced by the component at frequency (f_x, f_y) of a rough surface to be:

$$BSDF(\theta_i, \theta_s, \phi_s) = \frac{4\pi^2 \Delta n^2}{\lambda^4} \cos(\theta_i) \cos\theta_s Q \cdot PSD(f_x, f_y) \tag{6.20}$$

with Δn the difference in refractive index between the material of the surface under investigation and the ambient, λ the wavelength of the incident radiation, and Q called *polarization factor* a polarization dependant expression of the material reflectance. In most surfaces the PSD depend on the spatial frequency as a power law and is usually flat below a certain frequency as it can be seen in figure 6.5. A model that usually describe well the real surfaces when we can assume them to be isotropic is the ABC model [28]:

$$PSD(f) = \frac{A}{[1 + (Bf)^2]^{C/2}} \tag{6.21}$$

where f is the radial spatial frequency $f = \sqrt{f_x^2 + f_y^2}$, A represent the constant value at low frequency of the PSD, B the corner frequency at which the PSD starts to decay, and C the slope of the function at high frequencies. Substituting this expression for the PSD and performing a re-parametrization of the coefficients we obtain the Harvey-Shack model:

$$BSDF(\theta_i, \theta_s, \phi_s) = b\cos(\theta_i)\cos(\theta_s)\left(1 + \frac{|f_x^2 + f_y^2|}{l^2}\right)^{s/2} \tag{6.22}$$

where b, l and s are the model's parameter. The term $\cos(\theta_i)\cos(\theta_s)$ is called *obliquity factor*; this term in many literature works is simply neglected being most of the times close to 1. However recent studies [30] point out how this term becomes fundamental in describing surfaces where the condition $\sigma \ll \lambda$ is only weakly satisfied. In [30] it is shown how a generalization to rough surfaces of the Harvey-Shack model leads to a different form of this factor obtaining:

$$BSDF(\theta_i, \theta_s, \phi_s) = b\left[\cos(\theta_i) + \cos(\theta_s)\right]^2\left(1 + \frac{|f_x^2 + f_y^2|}{l^2}\right)^{s/2} \tag{6.23}$$

that reduces in the scattering plane to:

$$BSDF(\theta_i, \theta_s, \phi_s) = b\left[\cos(\theta_i) + \cos(\theta_s)\right]^2\left[1 + \left(\frac{\sin(\theta_s) - \sin(\theta_i)}{l}\right)^2\right]^{s/2} \tag{6.24}$$

As previously explaind the TIS of a surface can be obtained in a simple fashion by integrating the surface cBSDF; under Harvey-Shack model an exact solution for the TIS at normal incidence can be found:

$$TIS_R = \frac{2\pi b}{l^s(s+2)}\left[(1+l^2)^{(s+2)/2} - l^{s+2}\right] \tag{6.25}$$

6.3 Scattering facility set-up

In order to accurately measure the BSDF and the TIS of the coating samples we built a dedicated facility in a clean room environment in Padova's phyisics department. The design process of the facility went through multiple iterations but only the final version and the key characterization process will be presented here; an optical scheme of the final design can be seen in figure 6.6.

6.3.1 Facility Design

The scattering measurement facility is built in a class ISO 7 clean room in order to keep under control the dust contamination of the samples during the

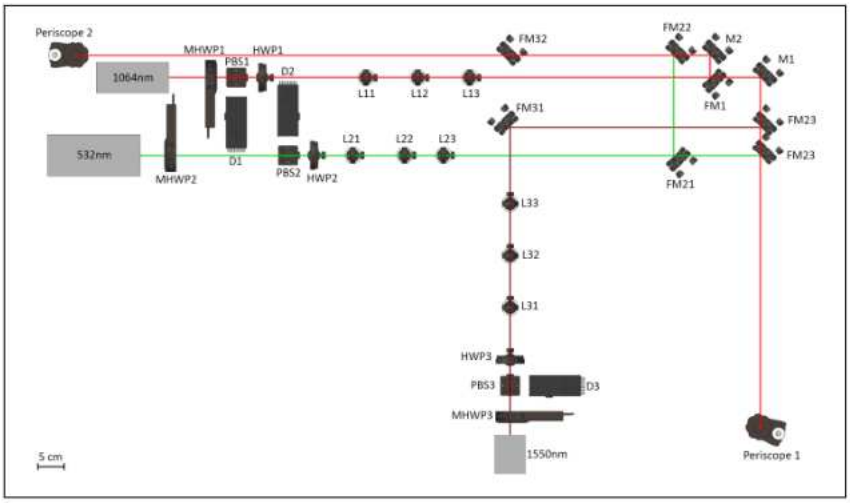

(a) First level.

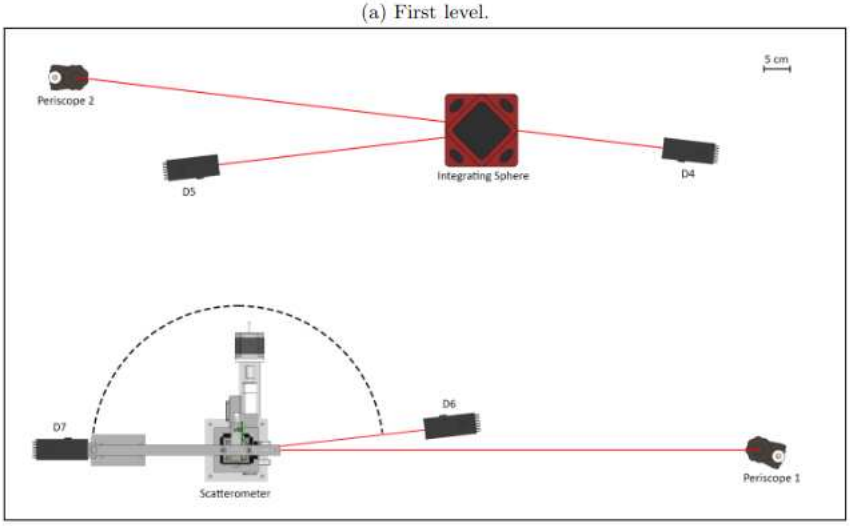

(b) Second level.

Figure 6.6: Optical Design of the Scattering facility built in Padova. a) Lower floor of the facility dedicated to the laser line conditioning. Three Laser lines are present with the possibility to control the output laser power and polarization. On each line a three lens telescope is built in order to control the spot size on a wide range. Through a system of flip mirrors, each line can redirected to one of two periscopes sending the Laser either to an integrating sphere or to the scatterometer instrument. b) Upper floor of the facility dedicated to the instruments. On the top the Integrating sphere, on bottom the scatterometer instrument.

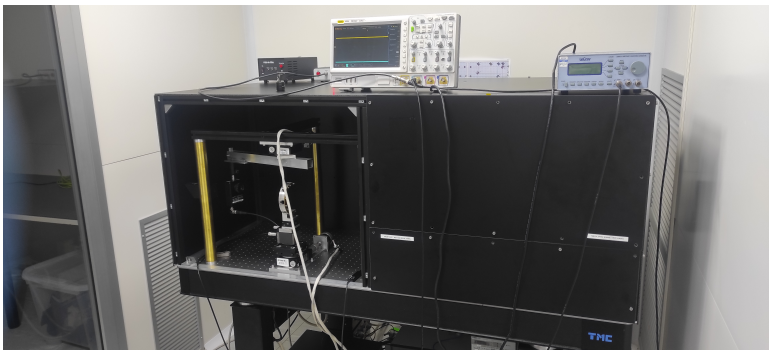

Figure 6.7: Picture of the current state of the scattering facility in Padova

scattering measurements. On a standard optical bench, the facility develops on two levels: on the lower level three different laser sources are present along with all the optics needed to control the beam dimension, power and polarization, on the upper level an Integrating sphere and a goniometric system (in the following "scatterometer") are placed to measure the TIS and the BSDF, respectively, at different wavelengths and different polarizations. The facility operates with three different laser wavelengths: 532 nm, 1064 nm, and 1550 nm (currently under construction at the time of writing). The choice of these three laser's wavelengths has been made to characterize optics for the current and future generation of GW interferometers (1064 nm and 1550 nm); the 532nm laser line is useful both to further explore the scattering phenomena as function of wavelength and also to characterize materials and coatings on a wavelength which is used in GW intererometers even if not for the main beam (eg for auxiliary optical lines or for the generation of squeezed vacuum states). The three adopted laser sources are solid state continuous wave (CW) lasers; 532 nm and 1064 nm sources have a maximum power of 1 W while the 1550 nm one has a maximum power output of 5 W. All three lines powers can be regulated through the use in combination of an half-wave plate ($\lambda/2$) and a polarizing beam splitter (PBS). Each of the laser lines hosts a telescope consisting of a system of 3 lenses, that allows to change the beam spot size on the sample from $\sim 250\mu m$ to $\sim 1500\mu m$.With a combination of flip mirrors and periscopes each laser line can be directed either to the integrating sphere or to the scatterometer hosted in the top level. The laser and measurements areas are separated by a number of black plastic panels to reduce as much as possible the presence of stray light in the measurement volume. In the scatterometer instrument the samples are mounted on a sample holder with with a C-shape that can accomodate samples up to 3" in diameter. The sample holder is placed on top of a rotation stage to change the incidence angle θ_i. The scatterometer detector is a high-sensitivity photodiode (active area of radius 0.5mm) mounted on a movable arm so that it can rotate around the sample at a darius of 34.5cm.

Wavelength	X		Y		Average	
	z_0 cm	w_0 μm	z_0 cm	w_0 μm	z_0 cm	w_0 μm
532	-18 ± 4	49 ± 2	-13 ± 4	44 ± 2	-16 ± 3	46 ± 1
1064	23.3 ± 0.8	365 ± 5	$20.4\pm$	359 ± 5	22 ± 0.7	362 ± 3
1550					220 ± 5	785 ± 10

Table 6.1: Designed position and focals for the lenses to be used in the telescopes of the three laser lines of the scattering measurement facility. The lens distances are calculated from the laser source position.

In front of the detector an iris and a narrow-band pass filter are muonted: the filter is changed according to the laser wavelength in use in order to reduce the background contributions. All the laser sources can be modulated, so that the signal from the scatterometer detector can be acquired trough the use of a lock-in system with a reference frequency of 23 Hz, in order to improve the SNR on a wide dynamic range. The motion of the sampole holder and of the arm are actuated by stepper motors controlled remotely via a labview based program: this software controls also the laser modulation and the acquisition of the photodiode signal.

6.3.2 Laser characterization

In order to correctly design the telescopes of the laser lines we firstly characterize the lasers used by testing their propagation in free space: we used a beam profiler to acquire a measure of the beam radius at various position and then interpolated the results in order to obtain the beams waists w_0 and the beams Rayleigh's ranges z_0. This procedures allows to characterize the laser beam along the vertical and horizontal axes of the transverse plane. In Table 6.1 the results of the procedure are reported. Note that since the 1550 laser line at the time of writing has not been built yet the values reported the laser has not been fully characterized yet. the values reported for the 1550 nm laser are then a rough estimate obtained via a knife-edge method.

6.3.3 Telescopes design

The design the telescopes of each laser lines are based on simulations performed through the use of JamMT software [81] and python scripts. The requirement of the telescopes are the possibility to change the beam spot on the sample in a range from approximately $250\mu m$ to $1500\mu m$ maintaining a fairly low divergence of the beam and avoiding beam clipping on optical elements to avoid potential stray light. The process used to simulate the telescopes configuration was to first use JamMT to find three lenses configurations able to produce the desired beam spot and changing it in the

desired range through the movement of either the first or the third lens; chosen a certain configuration we calculated via python the radius of the beam in correspondence of the main optical elements along the laser line in function of the position of the moving lens. We set the maximum movement of the lens allowed to be 10 cm, the maximum power lost via clipping to be 10^{-6} (same requirement on optics used in AdVirgo). The result of one of said simulation is presented for the line at 1064nm in figure 6.8 while the final configurations of the telescopes are reported in table 6.2

Wavelength	L1		L2		L3	
	focal	position	focal	position	focal	position
532 nm	50 mm	0.22 m	125 mm	0.35 m	300 mm	0.57 m
1064 nm	50 mm	0.64 m	150 mm	0.73 m	300 mm	1.03 m
1550 nm	50 mm	0.23 m	50 mm	0.26 m	200 mm	0.29 m

Table 6.2: focal values and positions of the lenses planned to be used in the construction of the telescopes of the three laser lines. The distances reported are calculated from the laser source.

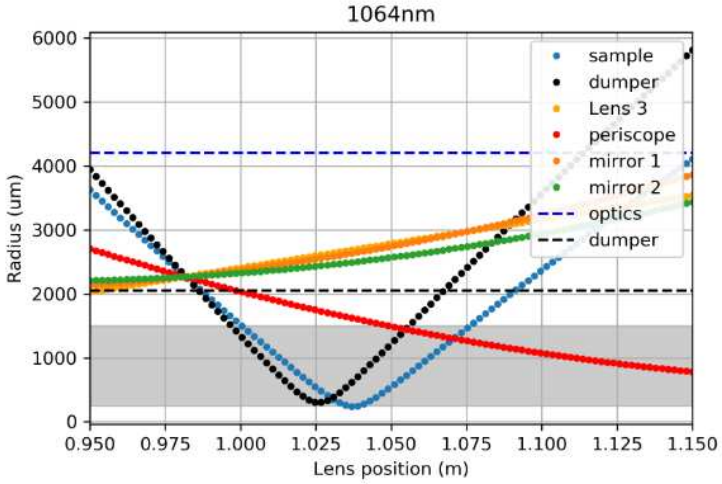

Figure 6.8: Simulation of the dimension of the beam size of the 1064 nm laser line for various optical elements in correspondence of the position of the third lens of the telescope.

6.3.4 Dark Noise Investigation

As a preparatory step, prior to the power modulation of the laser and to connect the photodiode to the lockin amplifier, we characterized the dark noise

of our electronic acquisition system. To perform such task we covered with a cap the detector photodiode and the laser in the system was kept initially turned off. We then manually moved the detector in several positions at 30° intervals acquiring with an oscilloscope in each position the signal from the detector for a time of 5 seconds. The data acquired are visible in figure 6.9. As expected no significant differences were found in the noises spectra

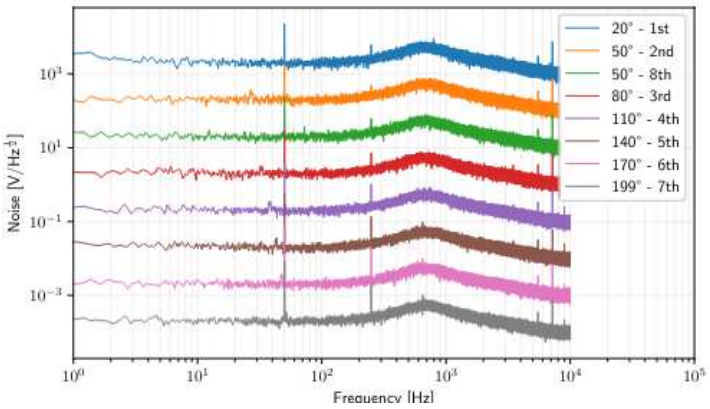

Figure 6.9: Noise spectra acquired at different detector positions. For sake of clarity the spectra are separated by multiplying them artificially by increasing powers of ten. No significant difference is found between them.

for the different acquisition angles.Except for the noise component at 50Hz and a very broad peak centered around 750 Hz, the noise spectrum appear mostly flat with a value of $\sim 2 \cdot 10^{-4} V/\sqrt{Hz}$. Due to the high gain of the photodiode transimpedance circuit (see below), our detection system has a limited bandwidth. For this reason, we decided to operate our modulated laser power at low frequency; on the other hand, a low frequency modulation requires long acquisition times when the lock-in amplifier is used. As a trade off, we decided to operate our system at 23 Hz.

6.3.5 Detector calibration

Determining the power the detector receive is of the utmost important in order to obtain a correct estimate of the BSDF. the detector [29] consists of a photodiode and a transimpedance amplifier: its output can be written as:

$$V_{out} = P_{in} \cdot R \cdot G \tag{6.26}$$

with R being the photodetector's responsivity in A/W (at 1064 nm $R \sim 0.82$ A/W) and G being the gain in V/A (in the mode used for acquisition $G = 2 \cdot 10^{10}$ V/A). In order to check whether the two numbers R and G provided by the photodetector's manual were correct and to investigate any possible non-linearity of the instrument, we performed a calibration of the

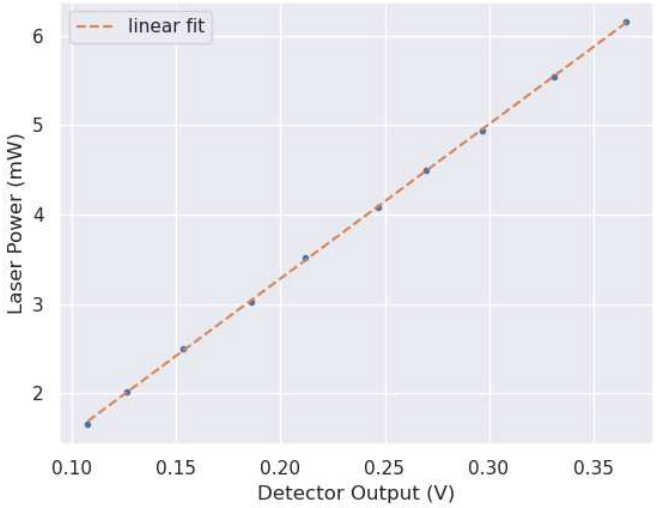

Figure 6.10: Experimental data and linear model for the correspondence between the optical power impinging on the detector and the signal outputted by it

signal obtained as a function of the incident power. We mounted a lens in front of the detector to be sure that the whole beam was collected by the detector,and then on the detector, to avoid its saturation, we mounted a narrowband filter centered at 1064 nm plus a stack of neutral density filters with a total attenuating power of $8.95 \cdot 10^6$. On the data visible in the graph of figure 6.10 we performed a linear fit obtaining a slope of 17.24 ± 0.08 V/mW and an intercept of -0.16 ± 0.02 V. Assuming the nominal responsivity the obtained gain estimate is $G = (1.93 \pm 0.05) \cdot 10^{10}$ A/V in agreement with the declared value of 2e10 A/V. Moreover no evident non-linearity were found in the operational range.

6.3.6 Sample Holder design and characterization

In figure 6.11 a scheme of the sample holder realized for the facility is shown. The key features that guided our design are the possibility of measuring at least one side of the sample without any obstruction and the minimization of the light scattered by the sample holder itself. To ensure that the surface of the sample under investigation contains the vertical rotational axis of the scatterometer the sample holder is mounted on a set of movable supports able to change its spatial positions x, y, z as well as the tilting angle of the sample. However, once the new holder was realized, we found that its contribution of the background of stray light is not negligible as wished that adds up to the one produced by the sample. In particular we find that the largest

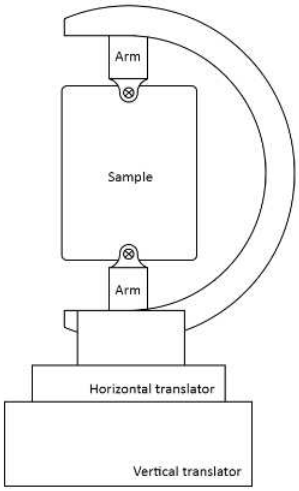

Figure 6.11: Scheme of the sample holder realized with the arms mounted.

contribution comes from the holder's arms that hold the sample in place. The arms are machined in aluminum with no particular surface polishing or treatment. To investigate this phenomenon we tried to model the scattering of the system. We modeled the arms as two Lambertian reflectors shaped as annular sections as can be seen in figure 6.12. Defining as θ_b the angle of the annulus, $2R$ the distance between the arms, $P0$ the incident beam power, and assuming that our laser propagates as a Gaussian beam with beam radius at the sample w we can write the power that impinges on the arms as:

$$P_{inc} = \int_{A_{arms}} I_{beam} dA = 2 \int_0^{\theta_b} d\theta \int_R^{\infty} I(r) r dr = 2 \frac{P_0 \theta_b}{\pi} e^{-2R^2/w^2} \quad (6.27)$$

Modelling the arms as Lambertian scatterers and assuming that the sample has a reflectance $R = 1$ we can compute the expected background as a function of the angular volume of the detector arms and their distance. The results of such computation are visible in figure 6.12 while in figure 6.14 a comparison of the simulated backgrounds with respect to some real measurements is shown. As it can be seen, the measured background levels are much higher than expected, even if the assumption used for the calculations are quite pessimistic. This lead us to the conclusion that the beam arriving into the sample position is not really an ideal Gaussian beam but is strongly contaminated by a light halo this is scattered by the arms and dominates the background. To reduce this contribution as part of this thesis work a dedicated campaign was started. While this is partially still in progress, already some positive results are obtained. In particular, a set of dark walls

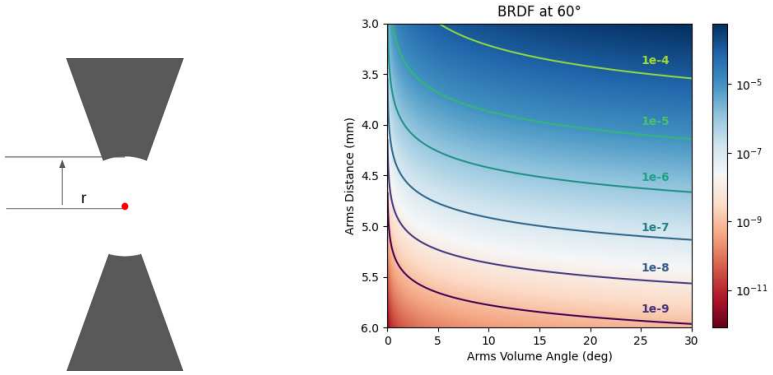

(a) (b)

Figure 6.12: a) Scheme of the geometry adopted to simulate the expected background scattered from the sample holder. b) Expected background at $\theta_s = 60°$ as a function of the solid angle occupied by the arms (x) and the holder arms distance (y)

has been added inside the scattering facility to absorb stray light and an iris was placed in the light path about 40cm before the sample to stop partially and reduce the halo reaching the scatterometer . As it is shown in figure 6.13 by closing the iris to a quarter of its aperture, about 6 mm diameter, it is possible to reduce the background by two orders of magnitude, down to a level suitable to measure the sample of interest for this thesis around $10^{-6} sr^{-1}$.

6.3.7 Detector Iris Optimization

Ambient and thermal light impinges on the detector and may saturate it regardless of the power modulated light originated from the laser. To reduce this problem, the setup is enclosed in a box formed by black, plastic walls. More importantly we stack on the photodiode a narrow band-pass filter at the target wavelength to limit the signal received to only the wavelength under study, and an adjustable iris to let the photodiode see the center of the scatterometer only witin a narrow solid angle. We took multiple measurement of the background signal at different scattering angles and at different iris apertures to check whether the background was influenced by said aperture. The results obtained are shown in figure 6.15. As we expected the smaller the iris aperture the smaller the background however if the iris aperture is too small we run the risk of cutting part of the scattered signal we are interested in. In order to set an appropriate limit to the aperture for the iris a stack of neutral density filters with a combined attenuation of $8.95 \cdot 10^6$ was set in front of the detector and the system was placed

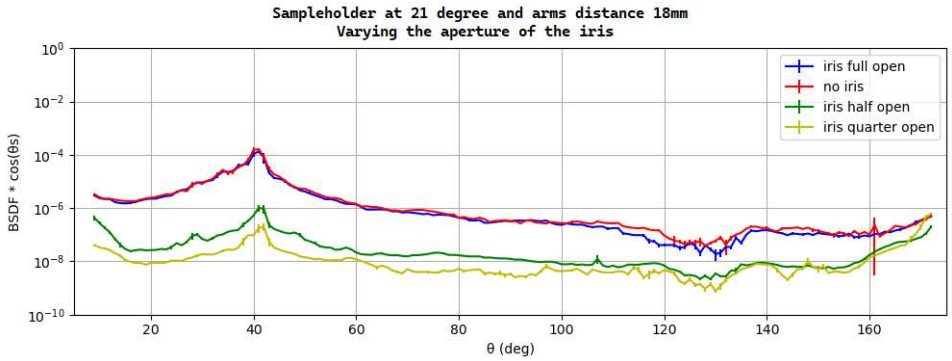

Figure 6.13: Backgrounds measured at $\theta_s = 21°$ by changing the aperture of the iris positioned on the laser entrance of the wall of the measurement volume.

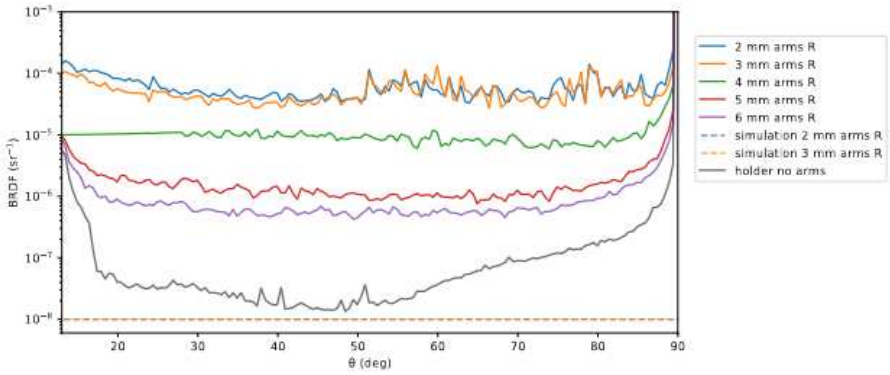

Figure 6.14: Comparison between experimental data (solid lines) and simulations (dashed lines) for the scattered backgrounds produced by different distances of the sample holder arms.

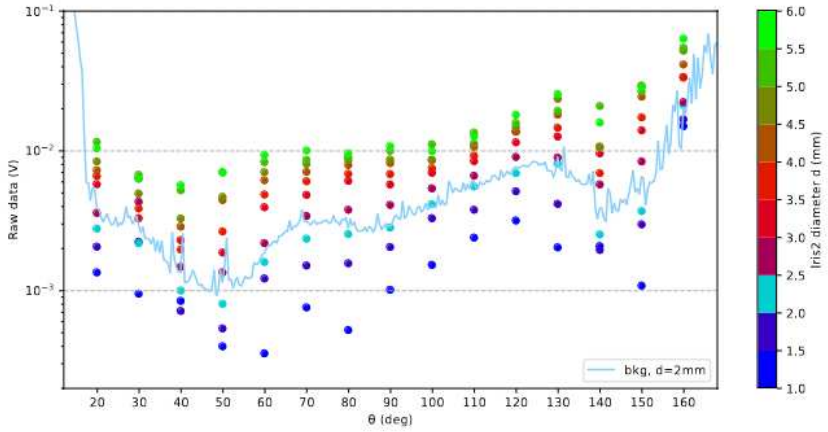

Figure 6.15: Background measured at different angles in the scatterometer varying the detector'iris aperture. The solid light blue line correspond to a 2 mm iris aperture background, the final value chosen for the iris aperture.

such that the full beam was impinging on the sensor. We progressively closed the detector'iris aperture until we started to observe a reduction of the signal signifying that the iris was starting to clip the beam at its edges. This value was found at 2 mm. We also investigated how at each angle the background signal was dependant on the iris aperture; in general we found that the background signal could be described by a quadratic model $Bkg = ad^2 + bd + c$ function of the iris aperture d. The three terms of the model are indicative of different process contributing to the scattering: the constant term c indicates the presence of direct reflections of the beam on some surfaces, the linear term bd can be linked to the presence of air and particulate scattering, and the quadratic term ad^2 is an indication of multiple reflections of stray light in the system. We found that at all angles the constant term was compatible with zero and in almost all cases the linear term was dominant on the quadratic one.

6.4 Investigation of optical scattering due to crystallization

As discussed in section 5.1 crystalline tantala has a density $\sim 10\%$ higher than amorphous one. From this observation, it is reasonable to expect that crystalline tantala has a also a higher refractive index compared to amorphous one, with a Δ_n increase which is probably of the order of 10%. As observed in section 4.3 the crystallization process proceeds by the formation of grains with a typical size in the um range. Thus, the formation of a collection of grains inside the coating acts as a source of scattering which,

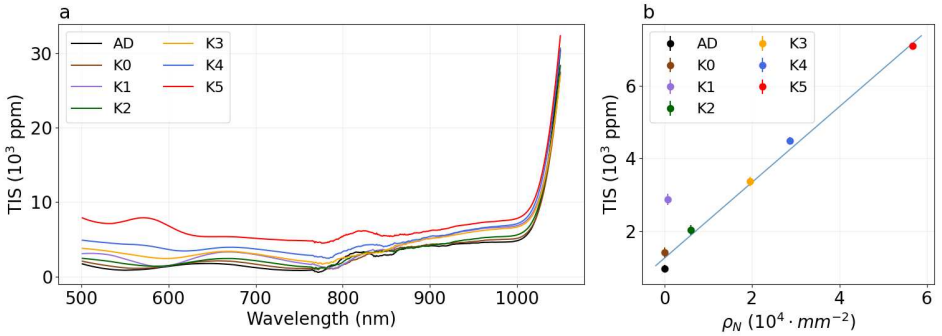

Figure 6.16: (a) TIS spectrum of as-deposited (AD) coating on silicon and K samples. (b) TIS at 532 nm vs. areal grain density ρ_N of K samples.

according to figure 6.3 operates in the Mie regime. In the following we report the effect of an incipient crystallization process on the TIS and on the BSDF of thermally treated tantala samples.

6.4.1 TIS measurements

The presence of a crystalline fraction may increase optical scattering losses in the treated coatings. To quantify this aspect we measured the Total Integrated Scattering of the series K samples from section 4.3.1 with an Internal Diffuse Reflectance Accessory (IDRA-2500) mounted on a Cary 5000 UV-Vis-NIR Spectrophotometer since our setup was not operative yet at the time of these measurements. Measurements were carried out in a reflection geometry with an incident angle of 8° in order to eliminate specular reflections, thus measuring only the diffusely scattered light. Results obtained for the wavelength range 500 to 1100 nm are shown in Fig. 6.16(a): the crystallized grains produce an increase of the TIS over all the measured spectral range. We are especially interested at the wavelength at which GW interferometers work, i.e. 1064 nm. However, since the Si substrate of the K samples is transparent in the infrared range, measurements at 1064 nm provide not only the scattering from the coating, but also from the back surface of the substrate, as can be seen from the steep increase of the TIS between 1000 and 1100 nm in Fig. 6.16(a). For this reason, in order to quantify the amount of scattering caused by the crystalline grains in the coating, we instead performed a quantitative TIS analysis at the half-wavelength 532 nm, taking advantage of the fact that in the Mie regime the scattering is weakly dependent on the wavelength. We assigned to these values the standard deviation of the TIS values measured between 515 and 545 nm as measurement error. Experimental TIS values vary between ∼900 ppm, for samples with no crystallization, to ∼7000 ppm, for the most crystallized sample K5. TIS is found to correlate well with the areal grain density ρ_N as measured

by optical microscopy, as shown in Fig. 6.16(b). This behaviour is likely to be attributed to the fact that the crystalline grains are platelet-like-shaped with a typical size equal to or greater than the wavelength, so that TIS is essentially proportional to the surface area of the coating consisting of crystal grains. By fitting the data of Fig. 6.16(b) to a linear dependency we obtain:

$$\text{TIS[ppm]} = m \cdot \rho_N + q \tag{6.28}$$

with $m = (1260 \pm 140)\ mm^2$ and $q = (1040 \pm 40) \times 10^{-4}$.

6.4.2 BSDF measurements

Before the last cycle of upgrades on the scatterometer facility we were able to acquire the BSDF data for three different samples of $\sim 200nm$ of Ta_2O_5 on a SiO_2 substrate thermally treated via RTA along with an as-deposited sample all taken from the same deposition run. The three samples were each treated for 8 minutes at 723°C, 744°C, and 765°C; the first sample upon GIXRD investigation proved to be still in an amorphous state while the latter two displayed an almost fully crystallized (a rough estimate of $\sim$ 80%) and a fully crystallized spectrum respectively. The samples were measured on 3 different positions each, with an incidence angle $\theta_i = 6.5°$, from a scattering angle $\theta_s = 13.5°$ to a scattering angle of $\theta_s = 163.5°$, in steps of 0.5°.
The measurements acquired, visible in figure 6.17, show as expected an increasing level of scattering with the treatment temperature reconducible to the amount of crystallization present in the material. From the acquired BSDF data we computed an estimate of the TIS of the samples in two different ways in order to compare this measurements with the ones performed on the samples from the K series.
The first method used was to calculate the TIS from the BSDF by obtaining an estimate of the b, l, and s parameters of HS model in the respective cases and then integrating the function over an entire hemisphere. We used a bootstrap method to associate an 95% CI to the TIS estimates.
The second method used was to perform a numerical integration of the data acquired assuming the BSDF to be radially symmetric around the specular reflection. Performing this task we have to take into account that our data are incomplete since they miss a region of 7 degrees around the specular reflection peak however this missing region is estimated to contribute to the TIS at most 10 % of the total value.
In Table 6.3 the values obtained for the two procedures are reported showing that the two methods give consistent results and confirming the obtained values.

As a preliminary test, we also measured three samples from the Z series (4.3.1) although we had no reliable way to convert the data obtained from the detector (in Volts) to the scattered Power (in Watts) and for this

	As deposited	723°C	744°C	765°C
TIS from fit (ppm)	4^{+10}_{-3}	34^{+20}_{-13}	1994^{+86}_{-87}	5400^{+390}_{-300}
TIS from data (ppm)	5.3 ± 0.3	47.9 ± 0.3	1784 ± 4	4782 ± 15

Table 6.3: Values of TIS estimated for samples of Ta_2O_5 treated under various conditions via RTA.

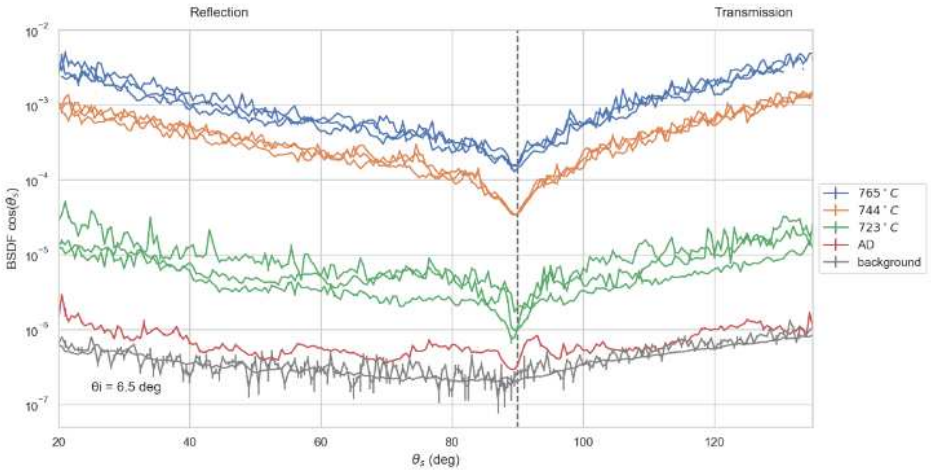

Figure 6.17: BSDF of Ta2O5 thin films measured with the scatterometer. The different samples are indicated by the temperature at which they received the treatment and compared to a sample that received no treatment (AD).

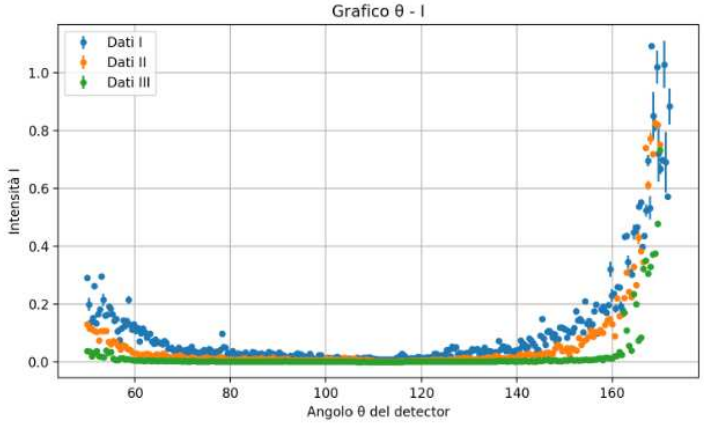

Figure 6.18: Measured BSDF on samples Z1, Z2, and Z3. Note how the different level of crystallization in the samples changes the shape of the BSDF.

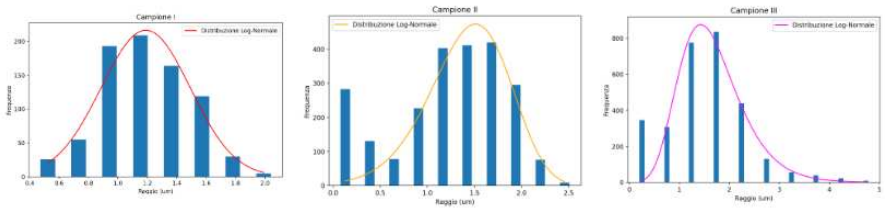

Figure 6.19: Measured grain size distribution of samples from Z1, Z2, and Z3. Data have been found to follow a lognormal distribution

reasons measurements of the BSDF of said sample could be acquired only in arbitrary units. We measured samples Z1, Z2, and Z3; the samples were measured with an incidence angle $\theta_i = 21°$, from a scattering angle $\theta_s = 50°$ to a scattering angle of $\theta_s = 170°$, in steps of 0.5°. The measurements acquired, visible in figure 6.18, show how different distributions of the crystallites sizes in our samples (reported in figure 6.19) affect the shape of the scattered BSDF. In the forthcoming developments, we will try to interpret those data by means of Mie theory in order to link them to the observed particle size distributions.

Chapter 7

Mechanical Losses

As introduced in chapter 2 the current technology of Gravitational waves interferometers is limited in the central detection band by the thermal noise arising from the various suspensions elements and from the optical coatings. The main objective of coating research within GW technology consist hence in finding material candidates or techniques able to lower the mirror's noise. In this chapter a more in depth explanation of what thermal noise is and how it's measured in coatings is given in section 7.1. After that in section 7.2 the results obtained by inducing a partial crystallized state are presented and discussed from the standpoint of coating thermal noise.

7.1 Thermal Noise

7.1.1 Resonant method and Dilution factor

To characterize thermal noise in coatings we make use of the Fluctuation Dissipation theorem [66] that establishes a connection between the thermal fluctuation of a physical variable and the associated response function. In the classical formulation of this theorem we can write the relation between the power spectral density of an observable x and its associated response function χ_{xx} as:

$$S_{xx}(\omega) = \frac{4k_bT}{\omega} Im[\chi_{xx}(\omega)] \tag{7.1}$$

In the case of coatings we are interested in observing the displacements of the surface of the mirror and we can characterize them by studying how the system composed by a substrate and a coating dissipates mechanical energy. A possible method of investigation for these processes is the resonant method in which the response of the sample through an external periodic excitation is studied. If we apply a periodic stress of frequency ω and amplitude σ_0 to our sample in the form:

$$\sigma(t) = \sigma_0 e^{i\omega t} \tag{7.2}$$

the corresponding deformation will take the form of:

$$\epsilon(t) = \epsilon_0 e^{i(\omega t - \phi)} \tag{7.3}$$

The compliance of the process, the ratio between the deformation and the stress, is then composed by a real an an imaginary part. From elasticity theory it can be shown that the real part of the compliance is related to the elastic energy stored by the system while the imaginary part is related to the energy dissipated through a cycle. The ratio between the imaginary and the real part of our compliance quantify the dissipation efficiency of the studied material and it's called mechanical quality factor Q^{-1} or internal friction of the material:

$$Q^{-1} = \frac{J_2}{J_1} = \tan(\phi) \tag{7.4}$$

The retardation phase ϕ that appears between the stress and the deformation from equation 7.3 here is shown to be tightly related to the mechanical quality of the sample; ϕ hence it's called *loss-angle* of the material. When the dissipation process is small we can approximate $\tan(\phi) \sim \phi$ and the energy dissipated through an entire oscillation cycle can be written as:

$$\frac{\Delta E}{E} = 2\pi\phi \tag{7.5}$$

If we excite our system with a periodic external excitation of frequency ω and we then stop the excitation the system will start to lose energy in time following the equation:

$$\frac{dE}{dt} = \Delta E/T = 2\pi\phi E/T \tag{7.6}$$

As the system loses energy the amplitude of its oscillations gradually reduce following the equation:

$$\epsilon(t) = \epsilon_0 e^{-t/\tau} \tag{7.7}$$

where the decay time τ is equal to $T/(\pi\phi)$. A measure of the oscillations decay time can hence provide an estimate of the loss angle of a material.
In a non homogeneous sample, like the case of our interest of a coatings deposited on a substrate, multiple dissipation process take place at the same time. In this case the loss angle of the system can be expressed as a weighted sum of the individual loss angles of the different dissipation processes:

$$\phi_{tot} = \sum_i D_i \phi_i \tag{7.8}$$

The weights of this equation D_i take the name of diluition factors and represent the relative distribution of the energy between the various components

of the sample and so sum to unity. We can hence write the loss angle of a coating on a substrate as:

$$\phi_{tot} = (1 - D)\phi_s + D\phi_c \tag{7.9}$$

where the subscription s indicates the substrate and the subscription c the coating. To estimate the coating loss angle we need to calculate the equation:

$$\phi_c = \frac{\phi_{tot} - (1 - D)\phi_s}{D} \tag{7.10}$$

while the total loss angle of the sample and the loss angle of the substrate are directly measurable from the decay of the oscillation as per equation 7.7, the diluition factor are more complicated to be estimated. Through the work of [19] it has been showed that, in the case of a substrate that has been coated on both surfaces with the same coating the diluition factor can be estimated as:

$$D = 1 - \frac{m_s}{m_tot} \left(\frac{\omega_s}{\omega_tot} \right)^2 \tag{7.11}$$

7.1.2 GENS system

Measurements of the mechanical properties of a coatings are extremely delicate since they require particular care to ensure that the only mechanism of energy dissipation present is the internal friction of the coatings themselves. This is usually achieved by suspending the sample however the point of contact between the suspension an the sample can become a source of energy dissipation that contaminates the measurements.
In this work the apparatus used to perform mechanical measurements was a Gentle Nodal Suspension system (GENS) [63] that tackles the problem of isolating the coating from the environment by suspending the sample from its center. As it can be seen in figure 7.1, disk resonators possess three families of vibrations (n, m) characterized by the number of radial nodes n and the number of azimuthal nodes m. Vibrations from the *Butterfly* modes family ($(0, m)$ $m \neq 0$) and from the *Mixed* modes family ((n, m) $n \neq 0, m \neq 0$) possess a nodal point in their center of mass hence vibrations from these families do not cause displacements in the center of the disk. The measurement of these families in the GENS system ensure that no energy is dissipated trough friction of the sample and the instrument. A photo of a GENS system can be seen in figure 7.2 In the GENS system the sample is firstly placed on top of a silicon halfsphere and held in place by its own static friction coefficient. The coatings resonance vibrations are subsequently excited through the use of an external AC voltage; the AC voltage then is turned down and the system is left to dampen the stored energy. To avoid any dampening from the air to occur all GENS measurements are performed in vacuum with a pressure below 10^{-6} mbar. Through an optical cantilever

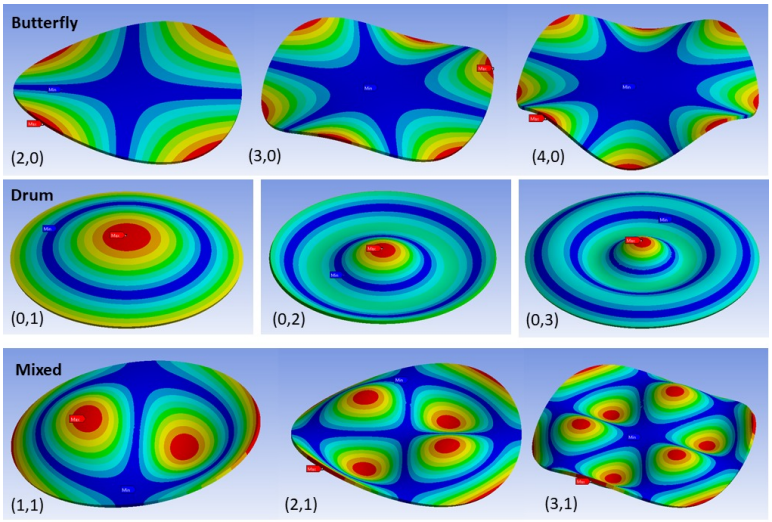

Figure 7.1: Resonant modes of a disk resonator. The butterfly and the mixed modes do not vibrate in the center of the disk. Image from [82]

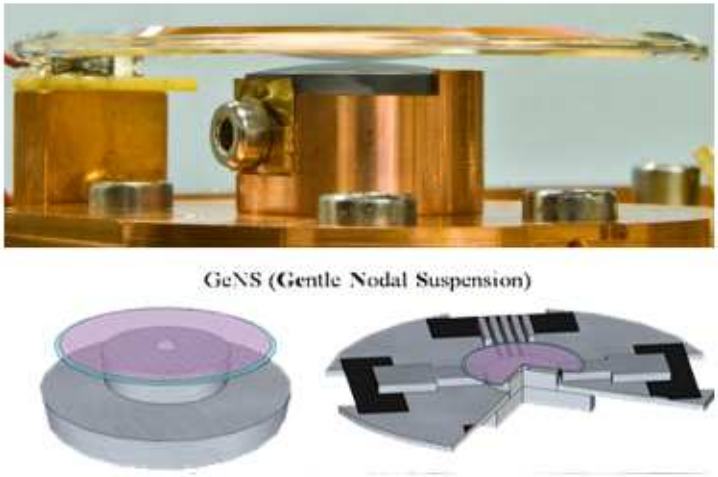

Figure 7.2: Top: Picture of a GENS system. Bottom: Schematic view of the instrument. Image from [64]

the amplitude of the vibration can be monitored during the entire process and the data acquired can be fitted trough the use of equation 7.7 to obtain an estimate of the loss angle of the material.

7.2 Mechanical measurements

To study the changes induced by the presence of crystallites in the amorphous matrix on the mechanical properties of a coating sample we produced a sample of $\sim$ 500 nm of tantala on a 75-mm diameter, 1-mm thick disk of Corning 7980 A fused silica for coating loss angle measurements. Prior to coating deposition, this thicker fused-silica disk was annealed in air at 900°C for 10 hours in order to release its internal stress due to manufacturing and to minimize its intrinsic loss angle φ_0 [17]. The coating was then deposited on both surfaces, in two consecutive coating runs, performed under identical conditions, in order to cancel out any potential curvature effect that might affect its mechanical resonance frequencies. This sample underwent the same annealing steps and in the same oven of samples from series K reported in Table 4.1, thus we can safely assume that after each step it featured the same crystalline fraction of samples from series K. Its coating loss angle was measured before and after the coating deposition as well as after each annealing step, as described in the following.

We used an experimental apparatus based on the ring-down technique [18] to measure the frequency f and ring-down time τ of several disk resonant modes, and calculated the coating loss angle φ_c as

$$\varphi_c = \frac{\varphi - (1-D)\varphi_0}{D} \ , \tag{7.12}$$

where φ_0 and φ are the loss angles associated to the internal friction of the bare disk and of the coated disk, respectively, and D is the so-called *dilution factor* defined as [19]

$$D = 1 - \frac{m_0}{m}\left(\frac{f_0}{f}\right)^2 \ , \tag{7.13}$$

where f_0, f, m_0 and m are the disk resonant frequency and mass as measured before and after coating deposition, respectively. We measured the sample mass with an analytical balance, before and after each treatment (coating deposition, annealing steps), and observed that it remained constant after the coating deposition, that is, the annealing steps never changed it. The measured mass values are reported in Table 7.1.

In order to avoid systematic damping from suspension and ambient pressure, we used a clamp-free in-vacuum Gentle Nodal Suspension (GeNS) system [20] in our ring-down apparatus. Resonant modes were measured from $\sim$2.5 to $\sim$20 kHz, in a frequency band partially overlapping with that of ground-based gravitational-wave interferometers ($10 - 10^4$ kHz). Fig. 7.3

m_0 (g)	m (g)	$m - m_0$ (g)
10.2872 ± 0.0005	10.3167 ± 0.0004	0.0295 ± 0.0006

.

Table 7.1: Mass of the fused-silica disk used in coating loss angle measurements, as measured before (m_0) and after (m) coating deposition.

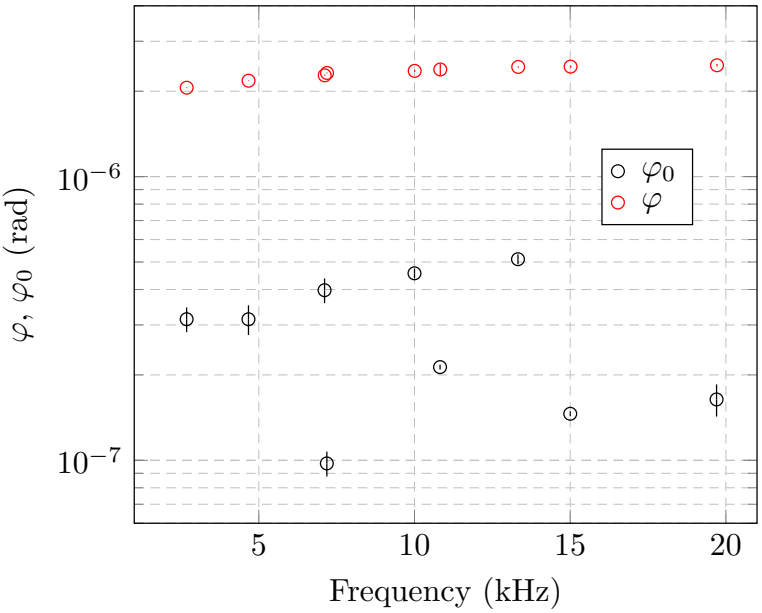

Figure 7.3: Sample loss angle of bare substrate (φ_0, black) and after coating deposition and annealing at 500 °C in air during 10 hours (φ, red).

shows the measured loss angles φ_0 and φ of the bare substrate and coated sample, respectively, where the typical uncertainties of the order of 10% for φ_0 and of the order of 1% for φ were obtained from three independent suspensions of the sample. Indeed, according to Eq. (7.13), the estimation of the dilution factor and hence of the coating loss angle via Eq. (7.12) depends critically on the resonant frequency of the sample modes, which in turn depend on the sample temperature; if the temperature is not constant throughout all measurement steps, a systematic error is introduced [23]. Thus, whenever we observed a temperature difference $\Delta T = T - T_0$ between measurement steps, we estimated the induced systematic frequency error as

$$\Delta f = \frac{\eta}{2} f_0 \, \Delta T \,, \tag{7.14}$$

where $f_0 \equiv f(T_0)$ is taken as the reference value, and $\eta = (1.50 \pm 0.01) \times 10^{-4}$ °C^{-1} [23], subtract it from measured resonant frequencies and used

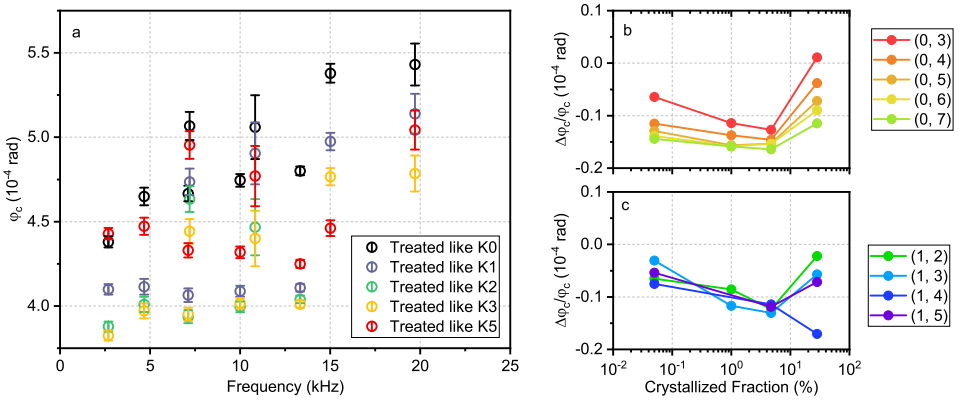

Figure 7.4: (a) Coating loss angle of disk from sample series (iii) as a function of frequency, as measured after annealing. Relative loss angle of (b) butterfly modes and (c) mixed modes vs. crystalline fraction.

the corrected values in Eq. (7.13). The obtained coating loss angle φ_c are reported in Fig. 7.4(a), as a function of frequency, where the uncertainty is a standard deviation obtained by propagating the uncertainties on measured values of resonant frequencies, mass and loss angles φ_0 and φ.

In order to highlight the changes brought upon by the amount of crystalline fraction, we define the relative coating loss angle variation after the annealing step i as

$$\frac{\Delta\varphi_c}{\varphi_c} = \frac{(\varphi_c)_i - (\varphi_c)_0}{(\varphi_c)_0} \ , \tag{7.15}$$

where $(\varphi_c)_i$ is the coating loss angle as measured after annealing step i and $(\varphi_c)_0$ is the coating loss angle value as measured after the first annealing at 500 °C, taken as reference. Figures 7.4(b) and (c) show the relative coating loss angle variation as a function of the coating crystalline fraction, for the so-called *butterfly* and *mixed* vibrational modes of different shapes [72]. Indeed, as shown by Fig. 7.4(a), in all our $(\varphi_c)_i$ data series we observe a branching of butterfly and mixed modes, likely due to a systematic effect of the raw, coated edge of the sample [72, 71, 70]. However, as Figures 7.4(b) and (c) show, such branching does not affect the observed general trend of the coating loss angle against annealing, which is the same for all modes, and can then be neglected. Thus, the coating loss angle of all modes decreases with the increase of the coating crystalline fraction with an optimum point at annealing step 3, that is, at around 12 hours of treatment at 630 °C and with a crystalline fraction of about 5%. At this point the coating loss angle is 10 to 20% lower with respect to the standard annealing procedure at 500 °C. A further increase of the crystalline fraction results in a steep increase of the coating loss angle. Our results thus prove that a modest amount of crystallization can be beneficial from the point of view of mechanical losses.

However, as shown in chapter 6, even a modest crystallization degree is sufficient to increase largely the scattering losses. This may be a significant limit on the applicability of this approach for GW interferometers.

Chapter 8

Conclusions

The detection of gravitational waves has become the fundamental tool to explore a wide range of cosmological and astrophysical theories. The central protagonists of this new way of exploring the cosmos have been the gravitational wave interferometers whose instrumental sensitivity dictates the portion of the universe we are able to access. A worldwide effort is spent to understand the noise sources that affect these instruments and to increase their capabilities. The current main limiting factor in Gravitational wave interferometers mid frequency sensitivity is the Brownian thermal noise that arise from the HR-coatings of the test mirrors. In this thesis we explored the possibility of employing a controlled partial crystallization state to reduce the noise characteristic of a material. Since coating Brownian thermal noise has been shown to arise mostly from high index materials [15] in this thesis work we chose Ta_2O_5, tantala, as our case of study.
We explored the crystallization kinetics of ion beam deposited tantala coatings from LMA. We found that the classical homogeneous crystallization model, the Avrami theory, is well suited to describe our coatings crystallization. After testing several isothermal annealing temperatures in the range between 680°C and 750°C we determined the the temperature dependence of the crystallization time, with evidence of a three dimensional growth of the crystalline regions. Doping tantala with titanium at 27%, as this is the current procedure used in Gravitational waves interferometers, has been shown in this work to modify the activation energies for the crystallization process hence increasing the temperatures and/or the times required to crystallize the material. The crystallization kinetic of a non-isothermal annealing process of tantala was then explored founding that the same activation energies determined in isothermal treatments could be used to describe it. Moreover we collected evidence that annealings performed on a sample, even if they don't induce the formation of crystalline regions in the material, alter the subsequent crystallization kinetics of the material.
Several techniques were employed to investigate the microscopic structure

of our crystallized material. We found that the crystalline grains forms inside of the amorphous matrix with an already large dimension around 5 nm. We identified the crystalline phase the material as δ-tantala choosing a P6/mmm symmetry unit cell recently proposed [21] to describe it as respect many other structures available in literature it was able to explain the experimental data with the same level of precision but using fewer parameters. Pair Distribution Function experiments performed in a synchrothron showed how although the identified P6/mmm structure is well suited to describe the material for correlation ranges greater than 15 Å, below this value it is ineffective. We interpreted this fact as an evidence that many polimorphs of crystalline tantala form in our coatings and that among them the dominant one is the hexagonal symmetry phase. The crystalline grains forming in the material upon investigation were found to be single-crystalline grains with random orientation whose size is comparable or larger than the film thickness.

Samples with different level of crystallization were then produced to investigate the optical and mechanical properties. We decided to study in this regard only samples that had undergone the standard 500°C 10 hours annealing treatment as this treatment is already adopted to improve the properties of the coatings and since in [25] it has been shown that longer annealing times up to 50 hours and higher annealing temperatures up to 600°C do not modify further the mechanical loss and do not show evidence of crystallization.

Our results show that, contrary to conventional wisdom, a small crystallized volume can be beneficial in terms of mechanical losses. In our study, an optimal crystalline volume fraction of about 5% (corresponding to a 12-hour treatment at 630°C) caused a 10–20% reduction in coating loss angle across all measured resonance modes. These results are also in line with recent findings in other materials such as GeO_2:TiO_2 [76] and SiO_2:TiO_2 [73] for which low values of the mechanical losses and/or coating thermal noise were observed after a prolonged annealing and in presence of crystallization. The systematic study hereby reported suggests that the stabilization mechanism due to the crystalline fraction may be responsible for the low mechanical losses also in those cases. At higher values of the crystalline fraction, the coating mechanical losses increase significantly. This indicates that two mechanisms are likely at play: the first, dominant at low grain densities, which stabilizes the coating structures, and the second one introducing additional losses at high grain concentrations. The optimal grain distribution is one in which the coating mechanical losses are minimized. However, the origin of these two contributions remains to be understood.

As the grain distribution influences also the optical losses we devoted part of our effort on the topic. A multi-wavelength facility able to perform both angle-resolved optical scattering and total integrated scattering measurements was designed and built in this work for this purpose. The facility

allows to choose for the measurement one between three different wavelengths (532 nm, 1064 nm, and 1550 nm), is designed to control both the total optical power as well as the intensity of the beam impinging on the sample and is able to measure scattering levels with a sensitivity higher than a part per million.
The amount of light scattered by our samples was found to linearly depend on the areal grain concentration. We believe that the amount of scattered light can be reduced by properly tailoring the grain distribution in our samples. As the crystallization kinetic of tantala are now known we can now achieve the same degree of crystallization through different annealing process and hence we can study how to control the density and the dimension of the grains forming in the material.
This work, although still preliminary in its results, open the way to a new procedure to optimize the properties of coatings for gravitational waves interferometers.

Appendix A

TIS measurements

In section 6.3 we went trough the construction of the scattering facility in Padova and the effort spent to make it functional. This appendix will deep down into the procedures adopted for the TIS measurements and the systematic errors one must consider.
As for equation 6.6 given an incident beam of power P_i the TIS of a sample can be calculated as the ratio of the incident and the power reflected by the sample. In a an integrating sphere we collect the reflected power and measure, after many more reflections inside the instrument, a fraction of this power that is assumed to be constant independently of the specific sample measured and so it will be called from now on η_{sphere} or *efficiency of the sphere*. The measurement photodiode collects then a power that can be expressed as:

$$P_{PD}(P_i, \lambda) = P_i \cdot TIS_s(\lambda) \cdot \eta_{sphere} + b(\lambda) = P_i \cdot m_s(\lambda) + bkg(\lambda) \quad \text{(A.1)}$$

where a background term $bkg(\lambda)$ has been introduced to account for the background light present inside the laboratory. In order to estimate the TIS of our sample we need to subtract then this background contribution and estimate η_{sphere}. Since this expression is a linear function the best way to eliminate this background is to acquire multiple measurements at different incident power and estimate the slope coefficient. In order to estimate the sphere efficiency instead the technique typically used is to measure the power scattered by a reference *"white"* sample whose TIS is assumed to be exactly 1 at the target wavelength and take then the ratio between the sample's slope and the reference slope.
This procedure however becomes more delicate once one consider also the possibility of having a background contribution proportional to the laser incident power. This situation can arise due to multiple reasons like stray light inside of the laboratory or the inherent air scattering at the target wavelength and can't so easily dismissed; dropping from now on the λ de-

pendency in our equations in this fashion we write then:

$$P_{PD}(P_i) = P_i \cdot m_s + bkg = P_i \left[m_{signal} + m_{bkg}\right] + bkg \tag{A.2}$$

To estimate this contribution the typical procedure adopted has been to take a measurement of the scattered power while there is nothing mounted on the integrating sphere sample port. This measurement however can easily be influenced by the backscattering of objects placed behind the integrating; to correctly estimate this contribution we placed a beam dumper catching the beam exiting the sphere at a distance d from it and measured the scattered power. Increasing the distance between the beam dumper and the sphere the solid angle of scattered light that is allowed to come back into the system progressively decrease. Assuming that the beam dumper scattering is almost uniform we can then model the measured slope in function of the distance d as:

$$m(d) = \frac{a}{(b-d)^2} + c \tag{A.3}$$

with a, b, and c free parameters of the model where the constant term represent then the power dependent background. The estimate of the sample TIS becomes then:

$$TIS_{sample} = \frac{m_{sample} - m_{bkg}}{m_{ref} - m_{bkg}} \tag{A.4}$$

Due to geometrical limitation is impossible to actually acquire the total amount of the scattered power. A first systematic loss is due to part of the power escaping through the apertures present on the scattering sphere, in our case the entrance port of the incident beam and the exit port of the specular reflection beam. A second loss is due to regions of the sphere not being able to perfectly redistribute the power towards the photodiode and in particular the main source of this effect is the small gap present between the sample and the inner side of the integrating sphere. A scheme of these two contributions can be seen in figure A.1. Calling α the fraction of power lost due to the first contribution and β the fraction lost due to the second contribution we can rewrite the slope of a sample's measurement as:

$$m_s = TIS^*(1-\alpha)(1-\beta)\eta_{sphere} + m_{bkg} \tag{A.5}$$

where TIS^* represent the "true" TIS of the sample. These two losses are dependant on both the geometry of the integrating sphere used and the shape of the scattering function of the sample so equation A.4 can be rewritten as:

$$TIS_s = \frac{TIS_s^*(1-\alpha_s)(1-\beta_s)\eta_{sphere} - m_{bkg}}{TIS_{ref}^*(1-\alpha_{ref})(1-\beta_{ref})\eta_{sphere} - m_{bkg}} \tag{A.6}$$

Since the reference TIS can be assumed to be 1 and since in our setup the reference sample mounts perfectly inside the sphere and hence $\beta_{ref} \sim 0$ we

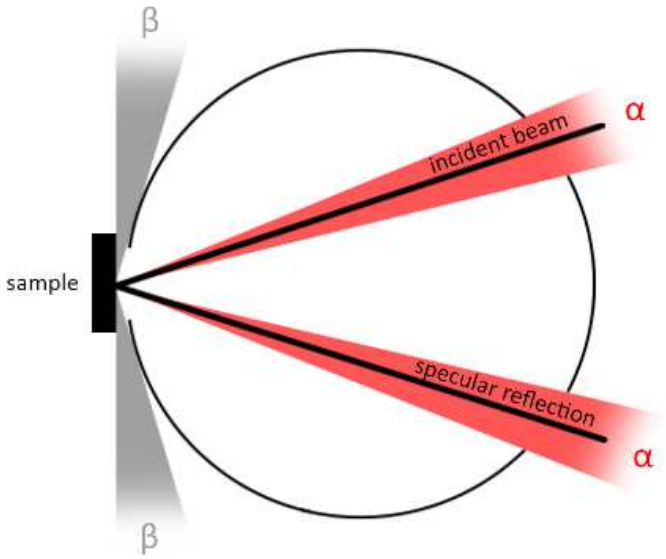

Figure A.1: Scheme of the two main systematic losses in an integrating sphere: α the power lost due to aperture in the sphere and β the power lost due to sample placement[75]

can simplify:

$$TIS_s = \frac{TIS_s^*(1-\alpha_s)(1-\beta_s)\eta_{sphere} - m_{bkg}}{(1-\alpha_{ref})\eta_{sphere} - m_{bkg}} \tag{A.7}$$

To estimate the α's terms we integrate over the solid angle Ω_a of the apertures the BSDF dividing it By the TIS:

$$\alpha = \int_{\Omega_a} \frac{cBSDF(\theta_s,\theta_i)}{TIS(\theta_s,\theta_i)} \mathrm{d}\Omega_a = \frac{\int_{\Omega_a} cBSDF(\theta_s,\theta_i)\mathrm{d}\Omega_a}{\int_0^{2\pi}\mathrm{d}\phi_s \int_0^{\pi/2} cBSDF(\theta_s,\theta_i)\mathrm{d}\theta_s} \tag{A.8}$$

In the case of a Lambertian diffusion like the one of our reference sample in our system we estimated $\alpha \sim 0.1\%$ while for an Harvey-Shack model with the b, l, s values close to the typical experimental ones $\alpha \sim 3.5\%$. In an analogous way for β integrating over the lost angles of our sphere we can write:

$$\beta = \int_{\Omega_l} \frac{cBSDF(\theta_s,\theta_i)}{TIS(\theta_s,\theta_i)} \mathrm{d}\Omega_l = \frac{\int_{\Omega_l} cBSDF(\theta_s,\theta_i)\mathrm{d}\Omega_l}{\int_0^{2\pi}\mathrm{d}\phi_s \int_0^{\pi/2} cBSDF(\theta_s,\theta_i)\mathrm{d}\theta_s} \tag{A.9}$$

and we found $\beta \sim 5\%$ for Lambertian diffusers and $\beta \sim 4.5\%$ for Harvey-Shack ones.

Bibliography

[1] Einstein, Albert (1916), "Die Grundlage der allgemeinen Relativitätstheorie", Annalen der Physik, 49 (7): 769–822

[2] Królak, A.; Patil, M. The First Detection of Gravitational Waves. Universe 2017, 3, 59. https://doi.org/10.3390/universe3030059

[3] B. Sathyaprakash et al., "Scientific objectives of einstein telescope," Classical and Quantum Gravity, vol. 29, p. 124013, jun 2012

[4] B. P. Abbott et al., "Exploring the sensitivity of next generation gravitational wave detectors," Classical and Quantum Gravity, vol. 34, p. 044001, jan 2017

[5] K. Danzmann et al., "Lisa—laser interferometer space antenna: A proposal in response to the esa call for l3 mission concepts," Albert Einstein Inst. Hanover, Leibniz Univ. Hanover, Max Planck Inst. Gravitational Phys., Hannover, Ger- many, Tech. Rep, 2017

[6] C. S. Unnikrishnan, "Indigo and ligo-india: scope and plans for gravitational wave research and precision metrology in india," International Journal of Modern Physics D, vol. 22, no. 01, p. 1341010, 2013.

[7] lma.in2p3.fr

[8] M. Maggiore, Gravitational waves: Volume 1: Theory and experiments. OUP Oxford, 2007.

[9] P. R. Saulson, Fundamentals of interferometric gravitational wave detectors. World scientific, 1994.

[10] LIGO Scientific Collaboration and Virgo Collaboration, "Observation of gravitational waves from a binary black hole merger," Phys. Rev. Lett., vol. 116, p. 061102, Feb 2016.

[11] "Sinc Function (normalized)." https://commons.wikimedia.org/wiki/File:Sinc_function_(normalized).svg

[12] "Virgo Optical Scheme."
https://commons.wikimedia.org/wiki/File:VirgoOpticalScheme. jpg

[13] K. D. Kokkotas, "Gravitational wave physics," Encyclopedia of Physical Science and Technology, vol. 7, pp. 67–85, 2002

[14] Abbott, Benjamin P. et al. (LIGO Scientific Collaboration and Virgo Collaboration) (2016). "Observation of Gravitational Waves from a Binary Black Hole Merger". *Phys. Rev. Lett.* 116 (6): 061102.

[15] M. Granata, A. Amato, L. Balzarini, M. Canepa, J. Degallaix, D. Forest, V. Dolique, L. Mereni, C. Michel, L. Pinard, B. Sassolas, J. Teillon, and G. Cagnoli, Amorphous optical coatings of present gravitational-wave interferometers, *Class. Quantum Grav.* **37**, 095004 (2020).

[16] M. Granata, A. Amato, G. Cagnoli, M. Coulon, J. Degallaix, D. Forest, L. Mereni, C. Michel, L. Pinard, B. Sassolas, and J. Teillon, Progress in the measurement and reduction of thermal noise in optical coatings for gravitational-wave detectors, *Appl. Opt.* **59**, A229 (2020).

[17] F. Travasso, P. Amico, L. Bosi, F. Cottone, A. Dari, L. Gammaitoni, H. Vocca, and F. Marchesoni, Low-frequency internal friction in silica glass, *EPL* **80**, 50008 (2007).

[18] A. Nowick and B. Berry, *Anelastic Relaxation in Crystalline Solids* (Academic Press, New York, 1972), p. 582-602.

[19] T. Li, F. A. Aguilar Sandoval, M. Geitner, L. Bellon, G. Cagnoli, J. Degallaix, V. Dolique, R. Flaminio, D. Forest, M. Granata, C. Michel, N. Morgado, and L. Pinard, Measurements of mechanical thermal noise and energy dissipation in optical dielectric coatings, *Phys. Rev. D* **89**, 092004 (2014).

[20] E. Cesarini, M. Lorenzini, E. Campagna, F. Martelli, F. Piergiovanni, F. Vetrano, G. Losurdo, and G. Cagnoli, A "gentle" nodal suspension for measurements of the acoustic attenuation in materials, *Rev. Sci. Instrum.* **80**, 053904 (2009).

[21] A. Martinelli et al, Phys. Rev. Materials 5, 115603 (2021)

[22] G. Cagnoli, M. Lorenzini, E. Cesarini, F. Piergiovanni, M. Granata, D. Heinert, F. Martelli, R. Nawrodt, A. Amato, Q. Cassar, J. Dickmann, S. Kroker, D. Lumaca, C. Malhaire, C. B. Rojas Hurtado, Mode-dependent mechanical losses in disc resonators, *Phys. Lett. A* **382**, 2165 (2018).

[23] M. Granata, A. Amato, M. Bischi, M. Bazzan, G. Cagnoli, M. Canepa, M. Chicoine, A. Di Michele, G. Favaro, D. Forest, G. M. Guidi, G. Maggioni, F. Martelli, M. Menotta, M. Montani, F. Piergiovanni, F. Schiettekatte, Optical and Mechanical Properties of Ion-Beam-Sputtered MgF2 Thin Films for Gravitational-Wave Interferometers, Phys. Rev. Applied 17, 034058 (2022).

[24] A. Amato, D. Lumaca, E. Cesarini, M. Granata, A. Lemaître, M. Lorenzini, C. Malhaire, C. Michel, F. Piergiovanni, L. Pinard, N. Shcheblanov, G. Cagnoli, Systematic error in the internal friction measurement of coatings for gravitational wave detectors, Phys. Rev. D 106, 082007 (2022).

[25] A. Amato, G. Cagnoli, M. Canepa, E. Coillet, J. Degallaix, V. Dolique, D. Forest, M. Granata, V. Martinez, C. Michel, High-Reflection Coatings for Gravitational-Wave Detectors: State of The Art and Future Developments, J. Phys.: Conf. Ser. 957, 012006 (2018).

[26] C. Spinella, S. Lombardo, F. Priolo, Crystal grain nucleation in amorphous silicon, *J. Appl. Phys* **84**, 5383 (1998).

[27] P. R. Spyak and W. L. Wolfe, "Scatter from articulate-contaminated mirrors. part 1: theory and experiment for polystyrene spheres and wavelength = 0.6328 microns," optical Engineering, vol. 31, no. 8, pp. 1746 – 1756, 1992

[28] Eric C. Fest. Stray Light Analysis and Control. SPIE—The International Society for Optical Engineering, 2013.

[29] Visible & IR Femtowatt Photoreceivers (Models 2151 & 2153) (New Focus Inc., 2002).

[30] James Harvey and Richard Pfisterer. "Comparison of the GHS Smooth and the Rayleigh-Rice surface scatter theories". In: Sept. 2016, p. 996103. doi: 10.1117/12.2237081.

[31] Egami, Takeshi and Billinge, Simon JL. Underneath the Bragg peaks: structural analysis of complex materials, 2003, Elsevier

[32] Billinge, Simon JL. The rise of the X-ray atomic pair distribution function method: a series of fortunate events, Philosophical Transactions of the Royal Society A 377 2147 20180413 (2019) The Royal Society Publishing

[33] ID 11 webpage,
www.https://www.esrf.fr/UsersAndScience/Experiments/StructMaterials/ID11
(2024)

[34] Rietveld Analysis of X-ray Diffraction Pattern from b-Ta2O5 Oxide L. A. Aleshina and S. V. Loginova

[35] Solvent free synthesis of Ta2 O5 nanoparticles and their photocatalytic properties A. Krishnaprasantha and M. Seethaa

[36] J. Lee; W. Lu; E. Kioupakis; Appl. Phys. Lett. 105, 202108 (2014) DOI: 10.1063/1.4901939

[37] Paolo Umari and Alfredo Pasquarello, First-principles analysis of the Raman spectrum of vitreous silica: comparison with the vibrational density of states, J. Condens. Matter Phys. 15 S1547–S1552 (2003)

[38] Teran, Anthony V. and Bill, Andreas and Bergmann, Ralf B., Time-evolution of grain size distributions in random nucleation and growth crystallization processes, Physical Review B 7 81 075319 (2010)

[39] C. Joseph and P. Bourson and M. D. Fontana, Amorphous to crystalline transformation in Ta_2O_5 studied by Raman spectroscopy, J. Raman Spectrosc. 8 43 1146–1150 (2012)

[40] Kim, Namjun and Stebbins, Jonathan F, Structure of amorphous tantalum oxide and titania-doped tantala: ^{17}O NMR results for sol–gel and ion-beam-sputtered materials, Chemistry of Materials, 23 15 3460–3465 (2011)

[41] Xu, Meng and Chen, Junchao and Wen, Yujie and Du, Jia-Huan and Lin, Zhiye and Peng, Luming, ^{17}O Solid-State NMR Studies of Ta_2O_5 Nanorods, ACS omega, 5 14 8355–8361 (2020)

[42] Long DA (2002) The Raman effect. John Wiley & Sons, Ltd, Chichester

[43] Jones, R.R., Hooper, D.C., Zhang, L. et al. Raman Techniques: Fundamentals and Frontiers. Nanoscale Res Lett 14, 231 (2019). https://doi.org/10.1186/s11671-019-3039-2

[44] U. Celano, Electrical Atomic Force Microscopy for Nanoelectronics, Springer (2019)

[45] J. F. Ziegler (2004). "SRIM-2003". Nucl. Instrum. Methods Phys. Res. B. 219–220: 1027. bibcode:2004NIMPB.219.1027Z. doi:10.1016/j.nimb.2004.01.208

[46] L. R. Doolittle, Algorithms for the rapid simulation of Rutherford backscattering spectra, Nucl. Instrum. Methods Phys. Res., Sect. B 9, 344 (1985)

[47] James E. Harvey, Narak Choi, Sven Schroeder, Angela Duparré Total integrated scatter from surfaces with arbitrary roughness, correlation widths, and incident angles, Optical Engineering, Vol. 51, Issue 1, 013402 (2012)

[48] Strutt, J.W (1871). "XV. On the light from the sky, its polarization and colour". The London, Edinburgh, and Dublin Philosophical Magazine and Journal of Science. 41 (271): 107–120. doi:10.1080/14786447108640452

[49] (Springer Atmospheric Sciences) Nicole Mölders, Gerhard Kramm (auth.) - Lectures in Meteorology

[50] Mie, Gustav (1908). "Beiträge zur Optik trüber Medien, speziell kolloidaler Metallösungen". Annalen der Physik. 330 (3): 377–445. Bibcode:1908AnP...330..377M. doi:10.1002/andp.1908330030

[51] F. Sgarbossa. "Innovative Methods for Germanium Doping." (2019).

[52] G.F. Harrington, J. Santiso, Back-to-Basics tutorial: X-ray diffraction of thin films, Journal of Electroceramics (2021)

[53] Lutterotti, Luca. "Maud: a Rietveld analysis program designed for the internet and experiment integration." Acta Crystallogr. A 56.s1 (2000): 54.

[54] Pecharsky, Vitalij K.. (24 November 2008). Fundamentals of Powder Diffraction and Structural Characterization of Materials. ISBN 9780387095790. OCLC 690510145.

[55] Caglioti, G.; Paoletti, A.; Ricci, F. P. (1 July 1958). "Choice of collimators for a crystal spectrometer for neutron diffraction". Nuclear Instruments. 3: 223–228. doi:10.1016/0369-643X(58)90029-X. ISSN 0369-643X.

[56] P. Scherrer, Göttinger Nachrichten Gesell., Vol. 2, 1918, p 98.

[57] Rietveld, H. M. (2 June 1969). "A profile refinement method for nuclear and magnetic structures". Journal of Applied Crystallography. 2 (2): 65–71. doi:10.1107/S0021889869006558. ISSN 0021-8898.

[58] Chateigner, Daniel. Combined analysis. John Wiley & Sons, 2013.

[59] Altomare, Angela, et al. "QUALX: a computer program for qualitative analysis using powder diffraction data." Journal of Applied Crystallography 41.4 (2008): 815-817.

[60] Gates-Rector, Stacy, and Thomas Blanton. “The powder diffraction file: a quality materials characterization database.” Powder Diffraction 34, no. 4 (2019): 352-360.

[61] Marangoni, A.G. (2017). Steady-State Nucleation Kinetics: The Fisher Turnbull Model. In: Kinetic Analysis of Food Systems. Springer, Cham.

[62] Gil-Gonzalez, Eva, et al. ”Crystallization kinetics of nanocrystalline materials by combined X-ray diffraction and differential scanning calorimetry experiments.” Crystal Growth & Design 18.5 (2018): 3107-3116.

[63] E. Cesarini et al., “A “gentle” nodal suspension for measurements of the acoustic attenuation in materials,” Review of Scientific Instruments, vol. 80, no. 5, p. 053904, 2009

[64] E. Cesarini et al., The Virgo Coating Collaboration: a detailed study on thermoelasticity in crystalline materials and other research lines, Proceedings of Gravitational-waves Science&Technology Symposium — PoS(GRASS2018)

[65] A. S. Nowick, Anelastic relaxation in crystalline solids, vol. 1. Elsevier, 2012.

[66] R. Kubo, “The fluctuation-dissipation theorem,” Reports on progress in physics, vol. 29, no. 1, p. 255, 1966.

[67] G. Vignaud and A. Gibaud, Reflex: A program for the analysis of specular x-ray and neutron reflectivity data, J. Appl.Crystallogr. 52, 201 (2019)

[68] https://pypi.org/project/miepython/

[69] Rice, Stephen O. ”Reflection of electromagnetic waves from slightly rough surfaces.” Communications on pure and applied mathematics 4.2-3 (1951): 351-378.

[70] Amato, Alex and Lumaca, Diana and Cesarini, Elisabetta and Granata, Massimo and Lemaître, Anaël and Lorenzini, Matteo and Malhaire, Christophe and Michel, Christophe and Piergiovanni, Francesco and Pinard, Laurent and Shcheblanov, Nikita and Cagnoli, Gianpietro, Systematic error in the internal friction measurement of coatings for gravitational wave detectors, Phys. Rev. D 106 082007 (2022)

[71] Diana Lumaca and Alex Amato and Matteo Bischi and Gianpietro Cagnoli and Elisabetta Cesarini and Viviana Fafone and Massimo Granata and Gianluca Maria Guidi and Matteo Lorenzini and Filippo Martelli and Lorenzo Mereni and Yury Minenkov and Matteo Montani

and Ilaria Nardecchia and Francesco Piergiovanni and Ernesto Placidi and Alessio Rocchi, Stability of samples in coating research: From edge effect to ageing, Journal of Alloys and Compounds 930 167320 (2023)

[72] G. Cagnoli and M. Lorenzini and E. Cesarini and F. Piergiovanni and M. Granata and D. Heinert and F. Martelli and R. Nawrodt and A. Amato and Q. Cassar and J. Dickmann and S. Kroker and D. Lumaca and C. Malhaire and C.B. Rojas Hurtado, Mode-dependent mechanical losses in disc resonators, Physics Letters A, 382 2165 (2018)

[73] McGhee, Graeme I. and Spagnuolo, Viola and Demos, Nicholas and Tait, Simon C. and Murray, Peter G. and Chicoine, Martin and Dabadie, Paul and Gras, Slawek and Hough, Jim and Iandolo, Guido Alex and others, Titania Mixed with Silica: A Low Thermal-Noise Coating Material for Gravitational-Wave Detectors, Physical Review Letters 131 17 171401 (2023)

[74] Jens Als-Nielsen, Des McMorrow, Elements of Modern X-ray Physics, John Wiley & Sons, Ltd (2011)

[75] Takimoto Schmiegelow, Izumi "Characterizing Light Scattering Sources in Gravitational-Wave Interferometers." (2023)

[76] Vajente, Gabriele and Yang, Le and Davenport, Aaron and Fazio, Mariana and Ananyeva, Alena and Zhang, Liyuan and Billingsley, Garilynn and Prasai, Kiran and Markosyan, Ashot and Bassiri, Riccardo and others, Low mechanical loss TiO_2:GeO_2 coatings for reduced thermal noise in gravitational wave interferometers, Physical Review Letters 127 7 071101 (2021)

[77] Waring JL, Roth RS. Effect of Oxide Additions on the Polymorphism of Tantalum Pentoxide (System Ta2O5-TiO2). J Res Natl Bur Stand A Phys Chem. 1968 Mar-Apr;72A(2):175-186. doi: 10.6028/jres.072A.018. PMID: 31824088; PMCID: PMC6640603.

[78] Fred Nicodemus, Directional reflectance and emissivity of an opaque surface (abstract), in Applied Optics, vol. 4, n. 7, 1965, pp. 767–775

[79] Becker, R., and Werner Döring. Kinetic treatment of the nucleation in supersaturated vapors. No. 1374. National Advisory Commitee for Aeronautics, 1954.

[80] A. Beer, Bestimmung der Absorption des rothen Lichts in farbigen Flüssigkeiten, in Annalen der Physik und Chemie, vol. 86, 1852, pp. 78-88

[81] A. Thuring and N. Lastzka, "Jammt - just another mode matching tool," (2011)

[82] Laura Silenzi, Mechanical and structural properties of silica coatings for mirrors of gravitational waves detector, (2020)

[83] G. Losurdo for the Virgo Collaboration, "Advanced Virgo Technical Design Report", available at https://tds.ego-gw.it/ql/?c=8940, 2012

[84] Jérôme Degallaix, Christophe Michel, Benoit Sassolas, Annalisa Allocca, Gianpetro Cagnoli, Laurent Balzarini, Vincent Dolique, Raffaele Flaminio, Danièle Forest, Massimo Granata, Bernard Lagrange, Nicolas Straniero, Julien Teillon, and Laurent Pinard, "Large and extremely low loss: the unique challenges of gravitational wave mirrors," J. Opt. Soc. Am. A 36, C85-C94 (2019)

[85] L. Pinard, C. Michel, B. Sassolas, L. Balzarini, J. Degallaix, V. Dolique, R. Flaminio, D. Forest, M. Granata, B. Lagrange, N. Straniero, J. Teillon, and G. Cagnoli, "Mirrors used in the LIGO interferometers for first detection of gravitational waves," Appl. Opt. 56, C11-C15 (2017)